Observation strategies for current and future geodetic very long baseline interferometry

Niko Kareinen

Observation strategies for current and future geodetic very long baseline interferometry
Niko Kareinen

Cover: The Onsala Twin Telescopes at Onsala Space Observatory.
Photo courtesy of Roger Hammargren.

Observation strategies for current and future geodetic Very Long Baseline Interferometry

NIKO KAREINEN
Department of Space, Earth and Environment
Chalmers University of Technology

Abstract

Geodetic Very Long Baseline Interferometry (VLBI) is an essential technique for space geodesy. It is uniquely capable of simultaneously observing all Earth Orientation Parameters (EOP) and directly giving access to the Earth's rotation angle (related to Universal Time, UT1). The EOP provide the link between the terrestrial and celestial reference frame. The latter is defined by positions of extra-galactic radio sources observed with geodetic VLBI whereas the terrestrial frame is realised through station positions and velocities. Ongoing phenomena such as the sea-level rise caused by global warming have magnitudes in the millimetre per year range. An accurate global reference frame is therefore crucial for reliably measuring these changes. The Global Geodetic Observing System (GGOS) and its VLBI component, the VLBI Global Observing System (VGOS), are designed to meet these challenges. The transition to the VGOS era brings challenges for all aspects of geodetic VLBI: telescope design, receiver development, recording, data transfer, correlation, observation planning, and analysis. The transition to VGOS involves gradually phasing out the legacy dual-frequency S/X telescopes, while delivering all IVS geodetic products and ensuring the continuity of the time series of geodetic parameters. The VGOS targets include continuous observations and delivery of initial geodetic products in less than 24 hours. This will require a fully automated VLBI analysis chain to make results available in near-real time.

This thesis aims at contributing to the improvement of current geodetic VLBI products and supporting the transition from the legacy S/X systems to observations in the VGOS era. Broadband VGOS observations necessitate upgrades for the receiver chain and the data recording devices. The Onsala Space Observatory (OSO) operated its analogue and a new digital back-end in parallel for almost two years. We present the results from a comparison, in which the new system was found to have no biases w.r.t. the old setup. We also investigate ways to improve the current IVS Intensive sessions. This involves using approaches that have relevance for the upcoming VGOS observations. We present fully automated analysis of INT1 sessions between 2001 and 2015 to investigate different analysis strategies and the impact of mapping functions, the use of auxiliary data, and lack of recent *a priori* EOP on the UT1-UTC accuracy. Up-to-date *a priori* polar motion was recognized as a key factor for the accuracy of UT1 estimates. Results from implementation and testing of fully automated robust L1-norm based ambiguity estimation are presented. We find that the L1-norm outperforms least-squares for ambiguity estimation. Lastly, optimal locations for a third station in tag-along mode for INT sessions are determined. We conclude that UT1-UTC WRMS can be reduced to 61 % (INT1) and 67 % (INT2) of the WRMS without the tag-along station. The UT1-UTC was improved significantly even without optimised schedules.

Keywords: VLBI, VGOS, GGOS, Earth rotation, Intensives, automated analysis.

i

List of Publications

This thesis is based on the following appended papers:

Paper I. Niko Kareinen and Rüdiger Haas (2015), *Experience from geodetic very long baseline interferometry observations at Onsala using a digital backend*, Journal of Geodetic Science, 5(1), 26–34, doi:10.1515/jogs-2015-0004.

Paper II. Niko Kareinen, Thomas Hobiger and Rüdiger Haas (2015), *Automated analysis of Kokee–Wettzell Intensive VLBI sessions — algorithms, results, and recommendations*, Earth, Planets and Space, 67(1), 181, doi:10.1186/s40623-015-0340-x.

Paper III. Niko Kareinen, Thomas Hobiger and Rüdiger Haas (2016), *Automated ambiguity estimation for VLBI Intensive sessions using L1-norm*, Journal of Geodynamics, 102, 39–46, doi:10.1016/j.jog.2016.07.003.

Paper IV. Niko Kareinen, Grzegorz Klopotek, Thomas Hobiger and Rüdiger Haas (2017), *Identifying optimal tag-along station locations for improving VLBI Intensive sessions*, Earth, Planets and Space, 69(1), 16, doi:10.1186/s40623-017-0601-y.

List of Acronyms

AAM	–	Atmospheric Angular Momentum
ABE	–	Analogue Back-End
AGN	–	Active Galactic Nucleai
BCRS	–	Barycentric Celestial Reference System
BIH	–	International Time Bureau (from French: Bureau International de l'Heure)
BVID	–	Bordeaux VLBI Image Database
BWS	–	Bandwidth Synthesis
CIO	–	Celestial Intermediate Origin
CIP	–	Celestial Intermediate Pole
CIRS	–	Celestial Intermediate Reference System
CPWL	–	Continuous Piece-Wise Linear
CRF	–	Celestial Reference System
DAO	–	Data Assimilation Office
DBBC	–	Digital Base Band Converter
ECEF	–	Earth-Centred Earth-Fixed
DBE	–	Digital Back-End
DORIS	–	Doppler Orbitography and Radiopositioning Integrated by Satellite
DOY	–	Day-Of-Year
ECI	–	Earth-Centred Inertial
ECMWF	–	European Centre for Medium-Range Weather Forecasts
ENU	–	East North Up
EOP	–	Earth Orientation Parameters
ERA	–	Earth Rotation Angle
ET	–	Ephemeris Time
FCN	–	Free-Core Nutation
FS	–	Field System
GCRS	–	Geocentric Celestial Reference System
GEOSS	–	Global Earth Observing System of Systems
GGOS	–	Global Geodetic Observing System
GIA	–	Glacial Isostatic Adjustment
GMF	–	Global Mapping Functions
GMT	–	Generic Mapping Tools
GNSS	–	Global Navigation Satellite System
GPS	–	Global Positioning System
GPT	–	Global Pressure/Temperature

GSFC	–	Goddard Space Flight Center
HOPS	–	Haystack Post-Processing System
GSI	–	Geospatial Information Authority of Japan
IAG	–	International Association of Geodesy
IAU	–	International Astronomical Union
ICRF	–	International Celestial Reference Frame
ICRS	–	International Celestial Reference System
IERS	–	International Earth Rotation and Reference Systems Service
IF	–	Intermediate Frequency
IMF	–	Isobaric Mapping Functions
ITRF	–	International Terrestrial Reference Frame
ITRS	–	International Terrestrial Reference System
IUGG	–	International Union of Geodesy and Geophysics
IVS	–	International VLBI Service for Geodesy and Astrometry
JAXA	–	Japan Aerospace Exploration Agency
JD	–	Julian Date
LLR	–	Lunar Laser Ranging
LNA	–	Low-Noise Amplifier
LO	–	Local Oscillator
LOD	–	Length-Of-Day
NASA	–	National Aeronautics and Space Administration
NGS	–	National Geodetic Survey
NICT	–	National Institute of Information and Communications Technology
NMF	–	New Mapping Functions
NNR	–	No-Net Rotation
NNT	–	No-Net Translation
NWM	–	Numerical Weather Model
OSO	–	Onsala Space Observatory
OTT	–	Onsala Twin-Telescope
PM	–	Polar Motion
PPN	–	Parametrized Post-Newtonian
PPP	–	Precise Point Positioning
REANNZ	–	Research and Education of Advanced Network New Zealand
RFI	–	Radio Frequency Interference
RMS	–	Root Mean Square
SEFD	–	System Equivalent Flux Density
STEC	–	Slant Total Electron Content
TECU	–	Total Electron Content Unit
TIRS	–	Terrestrial Intermediate Reference System
SINEX	–	Solution INdependent EXchange
SLR	–	Satellite Laser Ranging
SNR	–	Signal-To-Noise Ratio
TAF	–	Tag-Along Factor
TAI	–	International Atomic Time (from French: Temps Atomique International)
TCG	–	Geocentric Coordinate Time (from French: Temps-coordonnée géocentrique)

TEC	–	Total Electron Content
TIO	–	Terrestrial Intermediate Origin
TRF	–	Terrestrial Reference Frame
TT	–	Terrestrial Time
USNO	–	United States Naval Observatory
UTC	–	Coordinated Universal Time
UT1	–	Universal Time
VASCC	–	VLBI Analysis Software Comparison Campaign
VEX	–	VLBI Experiment Definition
VLBA	–	Very Long Baseline Array
VLBI	–	Very Long Baseline Interferometry
VGOS	–	VLBI Global Observing System
VMF	–	Vienna Mapping Functions
WRMS	–	Weighted Root Mean Square
ZHD	–	Zenith Hydrostatic Delay
ZWD	–	Zenith Wet Delay

Acknowledgments

First, I would like to thank my supervisor Rüdiger Haas for all the support and guidance he has given me throughout these years I have been a PhD student. You taught me a lot not just about VLBI but space geodesy in general. I would also like to thank my co-supervisor Thomas Hobiger, who provided invaluable scientific and technical insight, which helped realize many investigations from ideas to results. A thank you also goes to my co-supervisors Hans-Georg Scherneck and Hans Olofsson, as well as Gunnar Elgered, Jan Johansson, Peter Forkman, and Roger Hammargren.

The importance of good friends cannot be understated. I would like to thank the whole Geo-group for providing such an enjoyable working environment at Onsala. A big thank you also goes to all the PhD students and staff at Onsala and Chalmers. The fika room talks gave an insightful break from working.

I would also like to thank my family and friends back in Finland. Visiting you always felt like I had only been gone for a few days. Thank you for many relaxing summer holidays, kiitos, tack så mycket!

Niko Kareinen
Göteborg, April 2018

Contents

Chapter 1

Introduction

The Earth is a complex system with continuous dynamic processes between its interior, atmosphere, oceans, land and ice masses, and biosphere. These processes are driven by both external and internal forces. The largest external forces are due to the Sun and the Moon. The radiation from the Sun heats up the planet and drives many dynamic processes in the atmosphere and oceans. The gravitational attraction of the Moon and the Sun, and to lesser extent other planets, causes tides and changes in the Earth rotation. Due to the external gravitational forces and the diurnal rotation of the Earth we observe the familiar ocean tides. The surface of the Earth is not rigid either, but elastic and deforms periodically through phenomena called Earth tides. These deformations and mass redistribution change the angular momentum of the Earth, which in turn affects the rotation and the orientation of the rotation axis. Furthermore, the meteorological processes, such as movement of the masses of the atmosphere due to diurnal heating, cause changes in the Atmospheric Angular Momentum (AAM), which adds to the total change in the angular momentum. The response of the Earth to the external forces is also dependent on its interior structure. This makes it possible to study the inner structure of the Earth by observing its shape, gravity field, and movement and orientation in space. Thus, the Earth system is dynamic and deeply interconnected, with different phenomena coupled via transfer of angular momenta and mass redistribution. When these phenomena are modelled and observed accurately, we can decouple and estimate the different parameters of the system.

The study of the Earth as a system gives us the possibility to better understand the processes and changes that are ongoing on our planet. During the late 20th century it became evident that there is an ongoing global warming phenomenon. One major effect from the global warming can be observed as a long-term increase of global mean surface temperature since the start of the 20th century (Hartmann et al., 2013). Around 90 % of the increase in the heat content of the system is stored in the oceans (Bindoff et al., 2007). On a global scale this is detected as an increase in the mean sea level. According to Bindoff et al. (2007), between the years 1993 and 2010 the global mean sea level rose by 3.2 ± 0.4 mm. The effects of global warming can be observed both globally and locally. According to current scientific understanding there is a definite anthropogenic component to the warming trend, that is to say the

recent accelerated rise in temperature is man-made (Cook et al., 2013). This trend is linked to an increased amount of the various greenhouse gases in the atmosphere.

The projected effects from global warming are bound to have a huge and deleterious societal impact. To mitigate this, countries have attempted to reach agreements to reduce emissions of greenhouse gases. The Earth's population is projected to increase in the near-to-mid future, this leads to a difficult situation where on the one hand the leaders try to provide growth and at the same time shifting away from traditional energy sources. Thus, even though the observation and interpretation of the processes are a matter of scientific research, the conclusions have to be mediated in a reliable and convincing way to the political sphere, where the decisions are ultimately made. Due to the complex nature of the different interactions that contribute to global change, we need extremely accurate ways to measure these changes in order to be able to interpret the results, give predictions to the future, and convey the conclusions convincingly. An important part of this effort is the contribution of space geodesy and its ability to monitor changes in the Earth system on a truly global scale. Current space geodetic techniques rely on both space-borne and terrestrial methods, such as satellite geodesy and altimetry and Very Long Baseline Interferometry (VLBI). Due to the nature of these techniques, some are more capable of observing certain aspects of the Earth system than others. By combining these techniques it is possible to get a more complete picture of the ongoing physical processes.

The technique that is most relevant to this thesis is geodetic Very Long Baseline Interferometry (VLBI) (Sovers et al., 1998). Compared to other space-geodetic techniques VLBI is unique in its capability to determine all the five Earth Orientation Parameters (EOP) simultaneously. This is particularly important for connecting the celestial and terrestrial reference frames. Furthermore, Global Satellite Navigation System (GNSS) techniques can directly observe only the changes in UT1-UTC (i.e. its time derivative). These techniques rely on timely updates of the phase of the Earth's rotation (i.e. UT1) measured in an absolute sense with VLBI.

1.1   Outline of the thesis

This thesis presents the concepts and issues that are relevant to understanding the field of geodetic VLBI and the research carried out in the four papers appended to this thesis. The rest of this chapter introduces key observing system concepts that underpin the modern geodetic VLBI. Chapter 2 introduces important geophysical and geodetic concepts and how they are connected. Chapter 3 describes basic principles related to geodetic VLBI theory and the procedure for obtaining geodetic parameters from the observations. In Chapter 4 the challenges and solutions related to the transition from legacy VLBI to fully operational next generation VLBI system are discussed. Finally, in Chapter 5 a brief introduction and summary of the main results are given for the four papers appended to this thesis.

1.2 Global Geodetic Observing System

Cornerstones for reliable geodetic measurements are accurate reference frames and the capability to combine different reference frames via frame ties to an intra-technique geodetic reference frame. The Global Geodetic Observing System (GGOS) (Plag and Pearlman, 2009) is an observing system of the International Association of Geodesy (IAG) that brings together different areas and techniques of geodesy as a combined system. The decision to establish GGOS was made in 2003, and in 2007 it became an official IAG component. As an organizational layer GGOS acts as the link between the needs of Global Earth Observing System of Systems (GEOSS) and the contributions of the geodetic services provided by various IAG components. In 2005 a plan was drafted which states that within the framework of a 10-year implementation plan of GEOSS, geodesy will provide GEOSS components with accurate reference frames.

1.3 VLBI Global Observing System

The VLBI Global Observing System (VGOS) of the International VLBI Service for Geodesy and Astrometry (IVS) (Nothnagel et al., 2017) is the VLBI component of the GGOS (Schuh and Behrend, 2012). There is a need for increasingly accurate observations on a global scale in order to monitor both scientifically and societally important phenomena, such as sea-level rise. The concept was designed as a response to these requirements. Phenomena such as mean sea-level rise have magnitudes on the order of a few millimetres per year. For VGOS this means that the accuracy of the VLBI station positions and velocities needs to reach at least the same level as the observed phenomena. During the planning phase it became apparent that these requirements could not be met with existing legacy equipment and observation systems.

1.4 Transition to the VGOS era

Geodetic VLBI is currently in the transition process from legacy operational S/X VLBI observations to observing with VGOS era telescopes. During this period it is important to ensure the continuity of the existing time series of geodetic parameters and the delivery of IVS products. Major efforts are needed in all aspects of VLBI observing in order to realise a smooth transition to VGOS observations. This involves developing new technology for the telescopes, receivers, recording and correlation hardware, data transfer, and all aspects of observation planning and analysis. A key requirement in this transition is to move towards fully automated real time observations. In this thesis we approach this transition by investigating how the current VLBI observations, especially rapid UT1-UTC products, could be improved with methods that have the potential to also benefit the future VGOS operations.

Chapter 2

Geophysical and geodetic background

The variations in the Earth's shape, gravity field, orientation, and rotation are a result of various geophysical phenomena. Due to its elasticity Earth deforms under gravitational forces and mass transport. This in turn affects its inertial tensor that is linked to its rotational characteristics. External torques by the Sun, the Moon, and the planets inflict forced movement of the Earth's axis of rotation. These same external bodies cause a tide-generating potential that leads to a multitude of tidal effects.

The outer layer of the Earth is composed of the Earth's crust, gases and water in the atmosphere, and oceans. These react to the gravitational forces relative to their composition, which leads to phase lags in the tidal responses. The interior of the Earth is in constant motion, which can be seen as changes in Earth rotation. The radiation from the Sun causes diurnal heating of the air masses, which in turn plays a part in the movement of the air masses and hence the pressure that is inflicted on the Earth's crust. Seasonal changes in the biosphere and ground water deposits also contribute to the loading variations.

The rigid outer part of the Earth is called the lithosphere. The lithosphere deforms via plate tectonic motion, which in turn causes volcanism and seismic activity. These phenomena can have huge local impact on short time scale, such as meter level ground movement and post-seismic relaxation. In some cases they can be also global, if for example the composition of the atmosphere is drastically changed by volcanic activity leading to e.g. wide-scale temperature decrease and ice accumulation. Major cooling and warming cycles are also driven by the precession of the Earth's axis. The Earth is currently in an interglacial period. The long-term effects from this are seen particularly well in the Nordic countries as Glacial Isostatic Adjustment (GIA) (Steffen and Wu, 2011).

In the following sections the most important geophysical processes and geodetic concepts are described. The geophysical processes are mainly discussed through their connection to Earth rotation and displacements. For tidal displacements these are the solid Earth tides, ocean tidal loading, atmospheric loading, pole tide, ocean pole tide loading, and some non-tidal effects. For analysis purposes the recommended way

to account for these phenomena are described in conventions published and updated by the International Earth Rotation and Reference Systems Service (IERS).

2.1   Earth rotation and geophysical models

The external forces and geophysical processes are reflected as changes in the direction and magnitude of the Earth's rotation vector. The rotation of a non-rigid body such as Earth can be described by Eulerian equations with time varying angular momentum and external torques. The direction and motion of the Earth's axis of rotation in the space-fixed frame is affected through secular processes seen as precession and nutation. The axial tilt of the Earth can be described as the angle between the ecliptic plane and the celestial equator. It has a value of approximately $23.5°$. The gravitational torque by the Sun causes this pole to rotate with a main period of 26000 years along the precessional cone. The Moon causes the rotational axis to oscillate on this path with a period of approximately 18.6 years. These main motions are superimposed with other minor terms, which together constitute the precession-nutation motion of the Earth's axis of rotation (Lambeck, 1988).

The angular velocities of the Earth-fixed axes about themselves are assumed to be small variations in the direction cosines of the angular velocity vector with respect to the rotation axis of the Earth. The dynamical Liouville equations of motion for non-rigid Earth are given by

$$\frac{\mathrm{d}}{\mathrm{d}t}[\mathbf{I(t)}\boldsymbol{\omega} + \mathbf{h}(t)] + \boldsymbol{\omega} \times [\mathbf{I}(t)\boldsymbol{\omega} + \mathbf{h}(t)] = \mathbf{L}, \tag{2.1}$$

where $\mathbf{I}(t)$ is the time-dependent inertia tensor, $\mathbf{h}(t)$ is the angular momentum vector relative to Earth-fixed axes, $\mathbf{L}$ is the applied torque. The angular rotation vector of the Earth, $\boldsymbol{\omega}$, is given by (Munk and MacDonald, 1960)

$$\boldsymbol{\omega} = \omega_0[m_1\hat{\mathbf{x}}_1 + m_2\hat{\mathbf{x}}_2 + (1 + m_3)\hat{\mathbf{x}_3}], \tag{2.2}$$

where ω_0 is the mean angular velocity of the Earth, $\hat{\mathbf{x}}_{1,2,3}$ are the Earth-fixed axes, and $m_{1,2,3}$ are small disturbances in the non-rigid motion of the rotation vector. The latter are angular displacements that describe the position of the instantaneous rotation axis $\boldsymbol{\omega}$ with respect to the Earth-fixed axes $\hat{\mathbf{x}}$ on the equator plane of x_3. The two values m_1 and m_2 correspond to counter-clockwise rotations around x_1 and x_2, respectively. The movement described by these two is called the polar motion, giving the position of the instantaneous rotation axis. The parameter m_3 describes the difference from the uniform speed of rotation ω_0. It is connected to the change in Length-Of-Day (LOD), the excess of day measured by UT1 with respect to 86400 s. LOD and UT1 are related by

$$m_3 = \frac{\mathrm{LOD}}{86400 \text{ s}} = -\frac{d}{dt}(\mathrm{UT1} - \mathrm{UTC}). \tag{2.3}$$

More detailed descriptions of UT1 and UTC are discussed in Section 2.3.3. Formulating in terms of the three axes, Equation 2.1 can be written as

$$\frac{i\dot{m}_1 - \dot{m}_2}{\sigma_r} + m_1 + im_2 = \psi_1 + i\psi_2,$$

$$m_3 = \psi_3,$$

(2.4)

where i denotes the imaginary unit and σ_r is the rigid-body wobble frequency. The $\psi_{1,2,3}$ are excitation functions, which characterise the torques, relative motions, and changes in the inertia tensor of the system. This formulation describes the Earth rotation response to the geophysical phenomena included in the excitation functions. Furthermore, it separates polar motion and the variations in the rate of rotation. The rigid-body wobble frequency includes information on the constant terms of the inertia tensor components. The excitation functions include the time-dependent changes in the inertia tensor and angular momentum vector (Lambeck, 1988).

2.1.1 Tidal loading

The combined gravitational pull from external bodies provides a set of of tidal forces that cause deformation and mass movement in the solid Earth, atmosphere, and oceans. These forces and deformations also cause changes in the Earth's rotation axis and gravity field. The tidal effects have both permanent and periodic parts. A tide for which all observed periodic variations have been removed is referred to as mean tide.

2.1.1.1 Solid Earth tides

The combined effect of tidal deformation and the rotation of the Earth is seen as two main tidal bulges. This deformation can be detected via displacements of observing sites with, e.g., GNSS and VLBI. The tide generating potential is given by

$$V_{\text{tide}} = \frac{GM_i}{R_i} \sum_{n=2}^{N} \left(\frac{R_E}{R_i}\right)^n P_n(\cos\Psi),$$

(2.5)

where GM, R_E, and R_i are the geocentric gravitational constant, Earth radius, and distance from Earth's center to the centre of the ith disturbing celestial body, respectively. P_n are Legendre polynomials. Their argument $\cos\Psi$ is the cosine of the angle between the line from geocentre to the centre of the attracting body and a selected point on the Earth's surface. The terms $n = 0$ and $n = 1$ describe constant potential and Earth's orbital acceleration; the sum for the disturbing potential starts from $n = 2$. The harmonic expansion of the potential contains three main frequencies for the tidal potential. These are the long period, diurnal, and semi-diurnal tides. The crustal deformation response to the tidal potential depends on the composition of the crust. The maximum amplitude of solid Earth tides reaches 50 cm (Sovers et al., 1998). The Earth response to the solid tides can be characterized by the Love and Shida numbers, which act as scaling factors for the vertical and horizontal displacements. When these factors are complex-valued they also take into account the phase lag due to Earth's inelasticity. Solid Earth tides are the main tidal component in displacements. In order to reach sub-millimetre accuracy the 2nd degree tidal

potential caused by the Sun needs to be taken into account. For the Moon the 2nd and 3rd degree potential is needed (Petit and Luzum, 2010).

2.1.1.2   Ocean tidal loading

Oceans also have an response to the tide generating potential. The movement of the water masses deforms the underlying seabed and coastal regions. This effect is called ocean loading. The horizontal and vertical station displacements caused by ocean loading are on the centimetre level (Petit and Luzum, 2010). The magnitude of observed displacements is connected to the proximity to the body of water as well as local flow patterns. The ocean tides can be described by 11 main tidal components. The associated station displacement is computed as the sum of these tidal constituents, accounting for the amplitude and phase of the loading response of the site. Contributions from other tidal constituents, such as the 18.6 year lunar node (Scherneck, 1999), can be approximated from the 11 main tides and added to the displacements. In addition to the 11 main tidal components the IERS Conventions 2010 recommends inclusion of 342 constituent waves, which are based on the 11 main tides.

2.1.1.3   Atmospheric loading

The diurnal heating of the atmosphere leads to periodic pressure variation which causes displacements (Petrov and Boy, 2004). This effects is called the tidal atmospheric loading, and it consists of two major diurnal and semi-diurnal tides, S1 and S2, respectively. The amplitude of this loading effect is in the millimetre range (Petit and Luzum, 2010). The loading effect is highly dependent on the observer's latitude. The largest variations are seen in regions with high variation in the governing atmospheric pressure systems. Because these tides can lead to amplitudes similar to Ocean Loading at some sites and their periodicity is close to those of GPS satellites, the IERS 2010 Conventions include S1 and S2 in the recommended atmospheric loading computation.

2.1.1.4   Solid Earth pole tide

The polar motion causes a centrifugal force, which is a disturbing potential. The response of the Earth's crust to this potential is observed as pole tides. They cause station displacements in both vertical and horizontal directions. The greatest displacements are detected in the vertical direction. When computed against the mean pole (i.e. the secular part of the polar motion) the station displacements have amplitudes of 2 cm in radial and a few millimetres in lateral directions (Petit and Luzum, 2010).

2.1.1.5   Ocean pole tide

Similar to the case of Earth and Ocean tides, the ocean pole tide is the tidal response caused by the centrifugal polar motion. In the same manner it also contributes to

the site displacement. The amplitudes of the displacements range from 2 mm in radial to sub-millimetre in lateral directions. They were included in the IERS 2010 Conventions modelled according to Desai (2002). This model takes into account the continental boundaries, mass conservation, self-gravitation, and ocean floor loading.

2.1.2 Non-tidal loading

In general any type of redistribution of mass has the potential to cause deformation and thus displacements. These can be due to hydrology loading, in which water masses periodically stored in the ground cause changes in its mass and composition. In regions with regular seasonal weather patterns these can be detected as a seasonal signal in the station positions. However, it is possible that, for example, extended drought can change the grounds ability to hold water on the long term. These type of effects may cause disruptions in seasonal variation. Man-made effects such as deforestation can permanently change the composition of the soil and water flow patterns. This in turn could lead to more long-term changes in the normally observed displacements due the hydrology profile changing. As of now the latest IERS Conventions (Petit and Luzum, 2010) do not recommend including these effects in operational solutions.

2.2 Reference systems

Defining reference systems and establishing their accurate realizations (called reference frames) are an essential task in geodesy. On a global scale this involves two reference systems: a non-rotating quasi-inertial system and a co-rotating terrestrial system. Geodetic VLBI is important for providing both the realized reference frames and the connection between the two. The non-rotating celestial frame is defined by the positions of radio sources. The VLBI station locations contribute to defining the terrestrial reference frame. The transformation between these two is realized by the Earth Orientation Parameters (EOP).

2.2.1 Celestial Reference System and Frame

In 1997 at the 23rd General Assembly of the International Astronomical Union (IAU) it was decided that the new celestial reference system, based on directions realized by observations of extra-galactic radio sources, will be the International Celestial Reference System (ICRS). The ICRS is specified in the 1991 IAU Resolution on Reference Systems and it is defined by the IERS. The realisation of the ICRS is the International Celestial Reference Frame (ICRF). Its centre is defined at the barycentre of the Solar System. IAU also defines a celestial reference system that has the Earth as its origin. In its 2000 resolution IAU named the Sun- and Earth-centred systems the Barycentric Celestial Reference System (BCRS) and the Geocentric Celestial Reference System (GCRS), respectively. The ICRS is defined so that the observed barycentric directions of the extra-galactic sources show no global rotation w.r.t. the system. It was also designed in a way that ensured continuity

with the previous, fifth edition of the Fundamental Katalog FK5, reference system and its defining catalogue (Fricke et al., 1988). The first realization, ICRF1, was adopted in 1998. It is based on 608 extra-galactic radio sources. The equatorial coordinates of the sources were derived from 1.6 million S/X VLBI group delay observations made between 1979 and 1995. The source catalogue was divided into three sections: 212 defining sources, 294 compact sources (candidate sources), and 102 other sources. The defining sources have a median positional uncertainty of 0.4 mas. The compact sources (candidate sources) are sources whose positional accuracy can be improved with further observations. The 102 other sources did not have good enough astrometric quality but nevertheless could be used for, e.g., frame ties (Ma et al., 1998). ICRF2 is the second, and currently used, realization of the ICRS. It was adopted by the IAU in 2009 and contains the positions for 3414 sources, of which 295 are categorized as defining sources. It includes over 6.5 million S/X group delays between 1979–2009 (Fey et al., 2009). Compared to its predecessor ICRF1, ICRF2 improved the axis stability from 20 μas to 10 μas. The noise-floor was improved from 250 μas to 40 μas. Development of the third realization, ICRF3, is currently underway with a goal to complete the work by 2018. In addition to S- and X-band it will include higher-frequency frames on K, X/Ka, and Q-band (Malkin et al., 2015). It aims at providing an improved tie with the Gaia optical frame (Mignard et al., 2016) as well as improved source precision. Furthermore, the spatial coverage is expected to be improved by adding especially more southern-sky sources. In principle the ICRS sources are defined to have no apparent motion. However, it is to be noted that the movement of the solar system around the galactic centre causes the so-called secular aberration drift of approximately 5 μas/year in the apparent motion of the radio sources (Titov et al., 2011).

2.2.2   Terrestrial Reference System and Frame

The International Terrestrial Reference System (ITRS) (McCarthy and Petit, 2004) is defined following a resolution by the International Union of Geodesy and Geophysics (IUGG). Its realization is called the International Terrestrial Reference Frame (ITRF). It is a geocentric system with the center of mass defined for the whole mass of the earth, including oceans and atmosphere. The initial orientation is given by the Bureau International de l'Heure (BIH) at epoch 1984.0. Its unit is the SI metre, which is consistent with the Geocentric Coordinate Time (Temps-coordonnée géocentrique, TCG) time coordinate for a geocentric local frame. A No-Net-Rotation (NNR) is imposed to provide consistent horizontal time evolution with regard to tectonic plate movement (Petit and Luzum, 2010). The ITRF is realized by the IERS using observations from all four major geodetic techniques: VLBI, Global Navigation Satellite Systems (GNSS), Satellite/Lunar Laser Ranging (SLR/LLR), and Doppler Orbitography and Radiopositioning Integrated by Satellite (DORIS). Furthermore, local survey methods have an important part in determining the local ties between different co-located techniques. The latest realization of the ITRS is the ITRF2014 (Altamimi et al., 2016). The main changes to the previous realizations are the inclusion of annual- and semi-annual signals and parameters to account for

sites with post-seismic deformation. VLBI as a technique for the ITRF provides stable observations on long intercontinental baselines, which especially contribute to the scale of ITRF (Sovers et al., 1998). Furthermore, via EOP determination VLBI is the technique that ties together the ICRF and the ITRF.

2.3   Earth Orientation Parameters

Earth Orientation Parameters (EOP) are the rotation angles that describe the relation between an Earth-Centred Earth-Fixed (ECEF) and an Earth-Centred Inertial (ECI) coordinate system. From a geophysical perspective they come from the formulation in Equation 2.4. They manifest the effects of the external torques caused by the Sun, the Moon, and the planetary bodies and the resultant mass redistributions, which change the orientation and magnitude of the Earth's rotation vector in the Earth-fixed and space-fixed frames. Changes in the external torques and Earth's mass distribution, as well as Earth's dynamic response, are reflected in the secular and irregular terms in the EOP. The IERS publishes the EOP through various predicted, rapid, monthly, and long-term data products[1]. The following subsections will discuss EOP in terms of their response to the geophysical excitations discussed in the previous sections. Furthermore, the coordinate transformation for which the EOP are used is described.

2.3.1   Precession and nutation

The precession and nutation of the origins of the ICRF are described according to the IAU2006/2000 precession/nutation model (Capitaine and Soffel, 2015). The orientation of the Earth's rotation axis in space is described by the Celestial Intermediate Pole (CIP) and the direction of the Celestial Intermediate Origin (CIO) on the equator of CIP. The latest IERS Conventions (Petit and Luzum, 2010) define precession-nutation as the motion of the CIP in the GCRS. In this definition precession includes the 26,000 year term and the secular part of the motion and nutation is the residual motion that is not included in precession. IERS publishes the position of the CIP both consistent with the IAU1980 and IAU2006/2000 precession/nutation models. The offset parameters with respect to the IAU1980 model are given by nutations in longitude $\Delta\epsilon$ and obliquity $\Delta\psi$. The IAU2006/2000 nutation/precession parameters are given as celestial pole offsets dX, dY to the CIP location (X, Y) in an ECI reference system (Capitaine and Wallace, 2006). The precession/nutation amplitudes are within tens of arcseconds per year. The origin of longitude varies within milliarcseconds per century and between 1900–2100 it stays within 0.1 as relative to the initial alignment with the GCRS (Petit and Luzum, 2010).

Free Core Nutation (FCN) is the free motion caused by the interaction of the mantle and the Earth's fluid core. Because the FCN is not forced it is hard to model and predict. Its period is approximately 431 sidereal days (Malkin, 2007). It causes an additional CIP motion on the order of a few hundred μas. FCN can be predicted

---

[1]http://www.iers.org/IERS/EN/DataProducts/EarthOrientationData/eop.html

with an accuracy of approximately 100 μs RMS and its period and amplitude has been estimated from VLBI observations, e.g. Krásná et al. (2013). FCN is not included in the latest IAU2006/2000 precession/nutation model.

2.3.2 Polar motion

Polar motion is the movement of the rotation axis of the Earth in the TRF. It has both periodic and secular components. The three main components are the long-term drift (mean pole), an annual period, and the Chandler wobble, which has a period of approximately 435 days. The Chandler wobble is caused by excitations due to combination of atmospheric and oceanic processes with the largest contribution coming from ocean-bottom pressure fluctuations (Gross, 2000). Excitations from tidal motions and gravitational torques also cause daily and sub-daily variations in polar motion.

Polar motion is difficult to model, which consequently makes predictions difficult. The polar motion components are given by x_p and y_p, which describe the direction of the rotation axis in the terrestrial system. They are related to the formulation in Equation 2.4 by appropriate mean components via $m_1 = x_p - \overline{x}_p$ and $m_2 = -(y_p - \overline{y}_p)$. The x_p polar motion axis is aligned with the terrestrial x-axis, whereas the y_p axis has for historical reasons opposite sign with respect to the y-axis. The amplitude of the variations in total motion of the polar motion components during the 20th century are approximately 0.8 and 0.6 as for x_p and y_p, respectively. In addition to these variations the polar motion also has an additional long-term drift. On the surface of the Earth these amplitudes correspond to several meters (0.5 as $\sim$ 15 m). The polar motion values published by the IERS do not include corrections for the diurnal and semi-diurnal tide and the libration terms, which are included afterwards. The effect of the sub-daily tides and libration to polar motion are on the order of 0.5 μs (Petit and Luzum, 2010) and 60 μs (Chao et al., 1991), respectively.

2.3.3 Universal Time (UT1)

Universal Time (UT1) is a measure of the diurnal phase of rotation of the Earth around the CIP. It is connected through a linear relationship to the sidereal Earth Rotation Angle (ERA) (for a detailed description see Section 2.4, Equation 2.13).

Observations of UT1 (or ERA) must be referred to an external time reference This means that technically the observed parameter is typically either LOD or UT1-UTC. UTC is the Coordinated Universal Time which is defined to have 86400 s per day. UT1-UTC is defined to be constrained within 1 second of the UT1. Occasionally, due to gradual slowing down of the Earth's rotation leap seconds are added to UTC to keep the difference within the defined limits.

Because of the difficulty in modelling and predicting UT1 in general it must be determined from observations. VLBI is the only technique that can directly determine UT1 through observations of UT1-UTC. Because of this VLBI plays an essential role in providing a stable UT1-UTC time-series for e.g. satellite-based techniques, which have access only to LOD.

Libration and tidal effects cause periodic variations in UT1. The axial libration causes UT1 variations up to several microseconds. The effect of sub-daily tides on UT1 is on the order of 50 μs, whereas the effect of fortnightly tides is up to 785 μs (Petit and Luzum, 2010).

2.4 Transformation from ITRS to GCRS

After the station positions at the moment of observation are corrected for the various loading effects, they can be transformed from ITRS to GCRS via a series of rotations. In sequence these rotations transform the station coordinates according to

$$\mathbf{x}_{\text{GCRS}} = N(t){\cdot}R(t){\cdot}W(t)\mathbf{x}_{\text{ITRS}}, \tag{2.6}$$

where $W(t)$ (wobble) is a matrix combination of rotations representing polar motion, $R(t)$ is a rotation matrix for the diurnal rotation of the Earth around the Celestial Intermediate Pole (CIP), and $N(t)$ is the nutation-precession matrix which describes the orientation of Earth's axis of rotation in space. The time argument t (the signal time of arrival t_1 at station 1 in UTC referred to Terrestrial Time (TT) with respect to TT(J2000.0) (Petit and Luzum, 2010)) corresponds to

$$t = \frac{(TT - TT(J2000.0))_{days}}{36525}, \tag{2.7}$$

$$TT = t_1 + (\Delta_{TT-TAI} + N_{ls}), \tag{2.8}$$

where Δ_{TT-TAI} can be accurately realized as 32.184 s, and N_{ls} is the number of leap seconds applied to UTC until epoch t_1. J2000.0 is the epoch Jan 1st 2000 12:00 UT. The TT is a coordinate time, which has a mean rate that closely follows the observer time on a rotating geoid. TT is a theoretical time unit, which is realized by TT(TAI) = TAI + 32.184 s. The 32.184 s offset is due to maintaining continuity with its predecessor Ephemeris Time (ET) (Petit and Luzum, 2010).

Following the IAU 2000/2006 resolutions the transformation from ITRS to GCRS should be done with the CIP, defined in the GCRS and ITRS, and the Earth Rotation Angle (ERA). This transformation is done via two intermediate systems, the Terrestrial Intermediate Reference System (TIRS) and the Celestial Intermediate Reference System (CIRS). For both systems a non-rotating reference longitude is defined on the CIP equator, the Celestial Intermediate Origin (CIO) for the CIRS and the Terrestrial Intermediate Origin (TIO) for the TIRS. In the intermediate systems the z-axes are aligned with the CIP in that system and the x-axes to their respective reference longitudes. The expanded version of W is

$$W(t) = R_3(-s'){\cdot}R_2(x_p){\cdot}R_1(y_p) \tag{2.9}$$

where R_1, R_2, and R_3 are the conventional rotation matrices in a Cartesian coordinate system. The arguments for the first two rotations y_p and x_p are the polar motion coordinates for the CIP, respectively, and s' is the Terrestrial Intermediate Origin

(TIO) locator. The position of TIO with respect to the CIP equator is given by s'. Its value varies with time as a function of the polar motion coordinates following

$$s'(t) = \frac{1}{2} \int_{t_0}^{t} (x_p \dot{y}_p - \dot{x}_p y_p) dt. \tag{2.10}$$

The value of s' is determined by the large-scale variations in polar motion. With current mean values for annual and Chandler wobble terms the value of the TIO locator in μas is given by

$$s' = -47 \cdot t. \tag{2.11}$$

The W(t) rotation relates the ITRS coordinates to TIRS coordinates. The next rotation R(t) consists of

$$R(t) = R_3(-\text{ERA}), \tag{2.12}$$

where ERA is defined as the angle between the CIO and TIO measured along the equator of the CIP and R_3 is a rotation matrix about the z-axis. It can be expressed with linear relation to UT1 via $T_u(\text{UT1})$ by

$$ERA(T_u) = 2\pi(0.7790572732640 + 1.00273781191135448 \cdot T_u), \tag{2.13}$$

with $T_u = (JD(\text{UT1}) - 2451545.0)$ i.e. the Julian Date value of UT1 referenced to J2000.0 (Capitaine et al., 2000). This rotation transforms the coordinates from the TIRS to the CIRS.

The final rotation, N(t), transforms the CIRS coordinates to the GCRS. Physically it represents the effects of precession and nutation. This transformation is given by a combination of four rotations

$$N(T) = R_3(-E) \cdot R_2(-d) \cdot R_3(E) \cdot R_3(s), \tag{2.14}$$

where E and d define the coordinates of the CIP in the GCRS as

$$\mathbf{x}_{\text{GCRS}}^{\text{CIP}} = \begin{bmatrix} \sin d \cos E \\ \sin d \sin E \\ \cos d \end{bmatrix}, \tag{2.15}$$

while s is the CIO locator that describes the position of the CIO on the CIP equator between the reference epoch and t caused by nutation and precession. Similar to s' the CIO locator s is a time-integral of a function of the related coordinates. It is given by

$$s(t) = -\int_{t_0}^{t} \frac{X(t)\dot{Y}(t) - Y(t)\dot{X}(t)}{1 + Z(t)} dt - (\sigma_0 N_0 - \Sigma_0 N_0), \tag{2.16}$$

where X, Y, and Z are the coordinates of the CIP in the GCRS. The offset-term is a constant, which includes the position of the CIO at J2000.0 (σ_0), x-origin of the GCRS (Σ_0), and the ascending node of the equator in the equator of the GCRS at

J2000.0 (N_0). The rotations in Equation 2.14 can be expressed in terms of X and Y with $a = 1/(1 + \cos d) \approx 1/2 + 1/(8(X^2 + Y^2))$ (within 1 μas) as

$$N(t) = \begin{bmatrix} 1 - aX^2 & -aXY & X \\ -aXY & 1 - aY^2 & Y \\ -X & -Y & 1 - a(X^2 + Y^2) \end{bmatrix} \cdot R_3(s). \qquad (2.17)$$

The values for X and Y can be expressed by the IAU 2006/2000A model developed from the nutation and precession series. The value for s can be estimated via the quantity $s + XY/2$, which is numerically derived from Equation 2.16 using developments of values for X and Y (Petit and Luzum, 2010).

The use of CIP separates polar motion from nutation. By convention the nutation-precession includes variations that have a period of 2 days or larger and polar motion includes the terms with higher frequency.

Chapter 3

Geodetic Very Long Baseline Interferometry

Very Long Baseline Interferometry (VLBI) is an interferometric technique in radio astronomy that is based on simultaneous observations made with two or more radio telescopes to the same source. Depending on the application, the sources can be either natural or man-made. Typical natural sources are extra-galactic objects which have active emissions in the radio spectrum, such as quasars, Active Galactic Nuclei (AGN), and blazars. The recorded signals are compared against one another in a process called correlation to produce an interference pattern. VLBI is used in both astronomy and geodesy. The correlated data can be used to obtain images (maps) of the observed source with very high angular resolution or to derive the difference and rate in time-of-arrival (delay, delay rate) of the signal between the telescopes. The maps are important for astronomy in order to study sources too distant for any other observing technique, whereas the delay and delay rate form the basis for geodesy with VLBI. A closely related field is VLBI astrometry. It is involved with determining the distance and motion of celestial bodies. Whereas astronomers use VLBI to observe a multitude of objects with interesting physical properties and processes, in geodetic VLBI and astrometry compact sources with well-known structure are preferred. In addition to this, VLBI is also used for spacecraft tracking. An emerging field is to combine geodetic VLBI with observations of man-made radio transmitters on the moon, such as the Chinese Chang'E lander (Zhou et al., 2015). In order to combine the recorded signals they have to be aligned in time. To make correlation possible, the signals are digitized, time-tagged using an extremely stable frequency standards, such as a hydrogen maser, recorded, and transferred to the correlator. Then the correlator can playback and cross-correlate the recorded signals at a later time. Before adequately fast internet connections were available the data were shipped physically to the correlator on disk packs to the correlator. Nowadays it is feasible in some cases to transmit the recorded data afterwards or in near real-time.

The fundamental reason for observing with VLBI is to increase the angular resolution of the observing system. This provides angular resolution which far exceeds that achieved with a single telescope. For a single-dish telescope the approximate angular resolution follows $\theta \approx \lambda/D$, where θ is the angular resolution, λ is the

observed wavelength, and D is the diameter of a parabolic antenna (Karttunen, 2007). Typically VLBI observations for geodesy are made in the microwave region. The legacy geodetic VLBI observations are made on S-band (2.3 GHz) and X-band (8.4 GHz). For VGOS a frequency range of 2–14 GHz is discussed (Petrachenko et al., 2009). There is also an ongoing work to extend to higher frequencies (K-, Ka-, Q-bands) for improved ICRF determination (Malkin et al., 2015). When observing with VLBI, the diameter D of the antenna is replaced by the separation of the observing telescopes. Given that currently the size of a steerable radio telescope is structurally limited to about 100 m (see e.g. Green Bank Telescope[1]) and the theoretical maximum separation between the telescopes is twice the radius of the Earth (approximately 12000 km), this results in five orders of magnitude increase in angular resolution for VLBI over single dish.

3.1 Basic principle of geodetic VLBI

In geodetic VLBI the most commonly observed sources are quasi-stellar objects (quasars) and AGN (Fey et al., 2009). The general characteristics for a *good* geodetic source are high enough flux (to meet Signal-to-Noise Ratio targets), compact structure (i.e. as close to pointlike as possible), and low or predictable variability. Also, in an optimal situation the sources are evenly distributed around the sky. In physical terms the reason for using extra-galactic quasars and AGN billions of light years away is their high absolute energy output, which makes them detectable even at this large distance. It is this distance that makes the sources appear as nearly fixed set of reference points on the sky. The positions of the most suitable radio sources realize a non-rotating quasi-inertial reference system, as in the case of the ICRS and its realisation, the ICRF. Because the telescopes used in geodetic VLBI are located on the Earth's crust, the technique intrinsically links the ICRF to the Terrestrial Reference Frame (TRF). Thus, VLBI is used to realize the ICRS and to describe Earth's motion relative to that frame via providing the transformation parameters (EOP) between the terrestrial and celestial systems.

3.1.1 VLBI delay model

The observed parameter in geodetic VLBI is called the delay, which is the difference in signal time-of-arrival at the two stations forming a baseline. In essence VLBI is a geometric technique. The delay is directly related to the SI unit of meter via the speed of light c. In case of extra-galactic sources, without any loss of accuracy the wavefront arriving at the telescopes can be approximated by a plane wave. In general for sources further away than $\sim$30 light years the curvature effects of the wave front can be ignored (Sovers et al., 1998). The basic operating principle of VLBI is described by the geometrical relationship between a delay and baseline vector given by

---

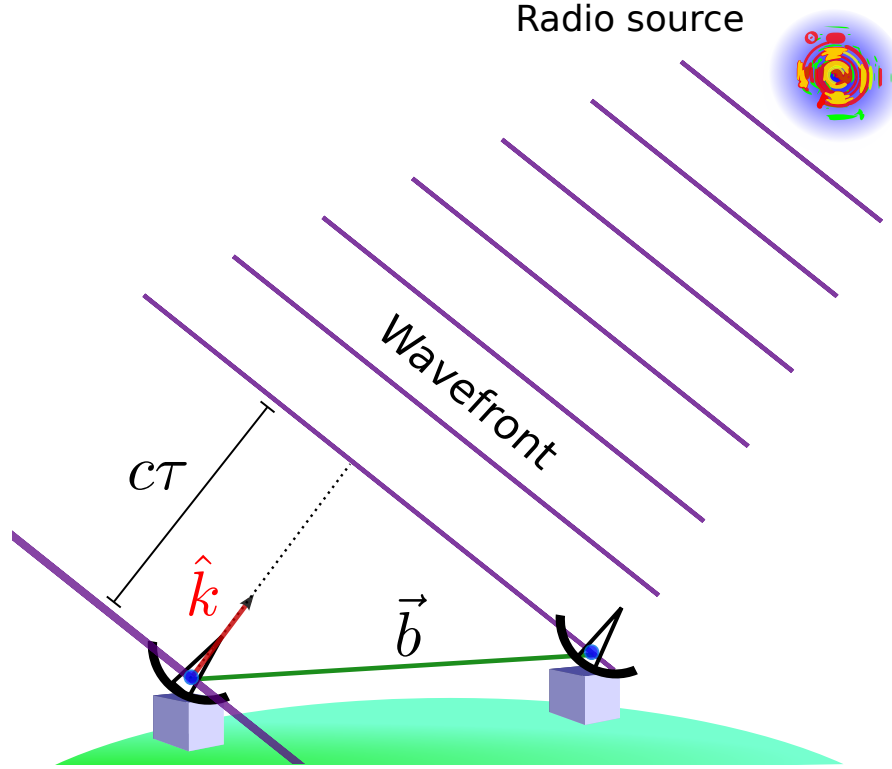[1] https://science.nrao.edu/facilities/gbt

Figure 3.1: VLBI observing geometry for a single baseline. A plane wave arrives from a radio source in direction $\hat{k}$ and is observed at two stations separated by a baseline b. The time-of-arrival delay of the signal between the two telescopes is τ and c is the speed of light in vacuum.

$$\tau_{12} = t_2 - t_1 = -\frac{1}{c}\, \mathbf{b} \cdot \hat{\mathbf{k}}, \tag{3.1}$$

where t_1 and t_2 are the signal arrival times at stations 1 and 2, $\tau_{12} = t_2 - t_1$ is the delay, $\mathbf{b} = r_2 - r_1$ is the baseline vector, and $\hat{\mathbf{k}}$ the source vector, a unit vector pointing towards the source. The geometric situation is illustrated in Figure 3.1.

The geometric model in Equation 3.1 is only valid for a simplified situation, where the endpoints of the baseline vectors are static and the signal is propagating in perfect vacuum. In order to account for time-varying geometry due to the Earth's rotation, gravitational bending, and signal propagation effects, the delay model needs to be extended. A standard approach is to have the signal arrival time (t_1) at the first station as the reference time for the observation. The baseline vector is then defined as $\mathbf{b} = r_2(t_1) - r_1(t_1)$. In its given form Equation 3.1 is only valid for the baseline vector where r_2 is constant. In order to account for Earth rotation the model needs to be extended with a term to account for the movement of station 2 during the signal propagation between t_1 and t_2 (i.e. shift $r_2(t_2)$ to $r_2(t_1)$).

In order to define the geometric delay in the geocentric frame, we first define the vacuum delay. Taking into account the gravitational bending of the signal due to the Sun, planets, the Moon, and Earth itself, the vacuum delay in geocentric

system (Petit and Luzum, 2010) is given by

$$\tau_{12,\text{vacuum}} = \frac{\Delta T_{\text{grav}} - \dfrac{\hat{\mathbf{K}} \cdot \mathbf{b}}{c}\left[1 - \dfrac{(1+\gamma)U}{c^2} - \dfrac{|\mathbf{V}_\oplus|^2}{2c^2} - \dfrac{\mathbf{V}_\oplus \cdot \boldsymbol{\omega}_2}{c^2}\right] - \dfrac{\mathbf{V}_\oplus \cdot \mathbf{b}}{c^2}\left(1 + \dfrac{\hat{\mathbf{K}} \cdot \mathbf{V}_\oplus}{2c}\right)}{1 + \dfrac{\hat{\mathbf{K}} \cdot (\mathbf{V}_\oplus + \boldsymbol{\omega}_2)}{c}},$$

(3.2)

where ΔT_{grav} is the gravitational delay contribution from all of the gravitating bodies, γ is the Parametrized Post-Newtonian (PPN) formalism parameter (in the theory of general relativity it is equal to one), U is the gravitational potential at the geocentre without including the mass of the Earth, $\mathbf{V}_\oplus$ is the barycentric velocity of the geocentre, $\boldsymbol{\omega}_2$ is the geocentric velocity of the second receiver, and c is the speed of light in vacuum. The barycentric source vector $\hat{\mathbf{K}}$ does not include the effects from gravitational bending or aberration.

The geometric delay is given by adding the geometric part of the tropospheric propagation delay due to vacuum delay following

$$\tau_{12,\text{geom}} = \tau_{12,\text{vacuum}} + \delta t_{atm_1}\frac{\hat{\mathbf{K}} \cdot (\boldsymbol{\omega}_2 - \boldsymbol{\omega}_1)}{c}.$$

(3.3)

The tropospheric propagation delays are estimated using the aberrated source vector k_i given by

$$\hat{\mathbf{k}}_i = \hat{\mathbf{K}} + \frac{\mathbf{V}_\oplus + \boldsymbol{\omega}_i}{c} - \hat{\mathbf{K}}\frac{\hat{\mathbf{K}} \cdot (\mathbf{V}_\oplus + \boldsymbol{\omega}_i)}{c}.$$

(3.4)

where $\boldsymbol{\omega}_i$ is the geocentric velocity of the ith receiver. The total delay is then given by

$$\tau_{12} = \tau_{12,\text{geom}} + (\delta t_{atm_2} - \delta t_{atm_1}).$$

(3.5)

In the above equations the δt_{atm_1} and δt_{atm_2} terms account for the total troposphere propagation delay at station 1 and 2. In practice the tropospheric delay is divided into a hydrostatic and a wet part. Most of the tropospheric total delay is explained by the hydrostatic part, which can usually be modelled *a priori* with sufficient accuracy, whereas the wet part needs to be estimated. The atmospheric modelling will be discussed in more detail in Section 3.1.2.2. The most natural coordinate system to describe the gravitational bending and propagation of the signal is the BCRS. On the other hand, the baseline vector is most conveniently expressed in the co-rotating terrestrial frame. To compute the scalar product the baseline and source vectors have to be in the same coordinate system. The station coordinates are transformed from ITRS to GCRS following the procedure in Section 2.4. As a result the EOP are included into the delay model. Then, following the general relativistic model described in this section, we transform the baseline vector and source vector into the same frame. The basis for many parameter estimation approaches is to form the difference between the observed and computed delay $(o - c)$. While the modelled geometric delay is the main delay term, the observed delay contains contributions from several other sources. These need to be either included in the computed theoretical delay or reduced from the observed delay. In fact, as described in sections 2.1.1
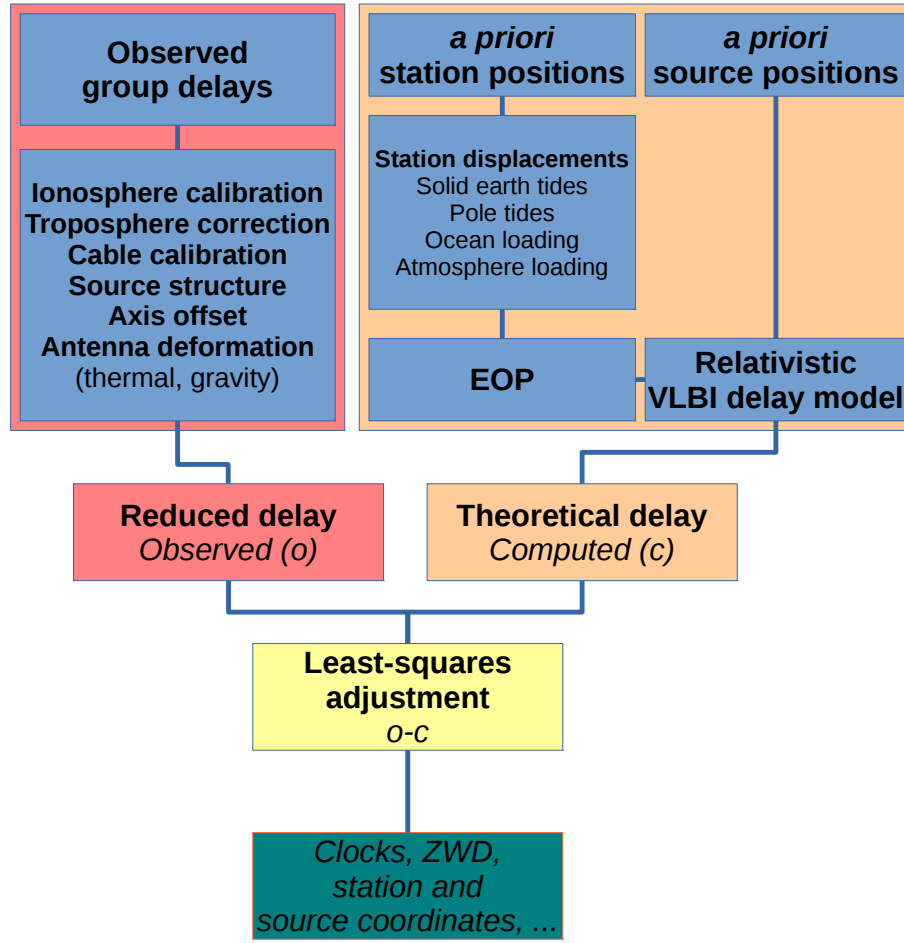
Figure 3.2: Forming the $o - c$ of the VLBI delay. The observed delay is reduced and the corrections are applied to the theoretical delay. The differences are used as an input to the parameter estimation, such as least-squares estimation.

and 2.1.2, due to deformation of the Earth's crust from a combination of various tidal and loading effects, the station coordinates, which are part of the geometric delay, undergo changes. These are handled by adding appropriate corrections to the *a priori* station coordinates. In addition to this, the observed delay includes contributions due to tropospheric and ionospheric path delays, to differences and variable rates in the station clocks, to instrumentation delays, and to antenna geometry and structure deformation (e.g. axis offset or thermal deformation). Most of the corrections can be provided with sufficient accuracy by models or *in situ* measurements such as cable delay and meteorological data. The station clock variations and the wet part of the troposphere can not be modelled or observed well enough and must be estimated from the observations. Naturally, other parameters of interest can be and are estimated as corrections to their *a priori* values. A flowchart depicting the formation of the observed and computed delay is shown in Figure 3.2. The following subsections describe briefly the main modelled delay constituents.

3.1.2   Atmosphere delay

Before the signal from a radio source reaches a telescope it has to travel through the different atmospheric layers. In VLBI the atmosphere can be regarded as being divided into two distinct layers: the charged ionosphere and the neutral troposphere. These media are dispersive and non-dispersive, respectively.

The ionosphere is a dispersive medium, meaning that the propagation velocity of the signal is dependent on its frequency. This also means that the phase and group velocities of the signal are not equal. For dual- or multi-band VLBI, the frequency dependence leads to different delays for different observing bands, which can be used to mitigate the effect of ionosphere to a great extent.

Geometrically, the signal path is bent due to changes in the refractive index. For VLBI frequencies in the neutral atmosphere there is no frequency dependence and thus the phase- and group velocities are equal. The refractivity of the neutral atmosphere can be divided into a hydrostatic part and a non-hydrostatic wet part.

3.1.2.1   Ionosphere delay

The ionosphere is a region of the atmosphere that consists of electrically charged particles. It starts at an altitude of approximately 1000 km and can reach down to 50 km above the surface of the Earth. The Sun is the driving force of the ionosphere. At high altitudes the air mass is sufficiently thin for the electrons to be removed from their host atoms and molecules by the Sun's radiation to exist as free electrons for a prolonged time. These free electrons and ionized molecules have the properties of a plasma. In general the extent is dependent on the plasma density, which in turn is proportional to the Total Electron Content (TEC). Because the process is driven by the Sun, there is a diurnal cycle of TEC. The density peaks during daytime when the Sun's radiation is the strongest. During night the free electrons recombine with the ionized molecules. The changes in the magnitude of TEC during the day-night-cycle are dependent on the particular composition of the different ionospheric layers (Hobiger and Jakowski, 2017).

The phase delay due to the ionosphere is given by

$$\Delta_{pd}^{iono} = \frac{1}{c} \int (n(f) - 1) dl, \tag{3.6}$$

where $n(f)$ is the frequency dependent refractive index and dl is the differential of the propagation path.

For dual-band VLBI it is sufficient to use the first order approximation of the integral to compute the ionosphere phase and group delays. The ionosphere phase delay in metres is given by

$$\tau_{pd}^{iono} = -\frac{40.31}{f^2} STEC, \tag{3.7}$$

where $STEC$ is the slant TEC along the ray path. TEC is given in TEC-units (TECU), where 1 TECU is a column density of 10^{16} electrons per m^2. The factor

40.31 is a constant derived from electron mass, electron charge, and the permittivity of free space, and its unit is $[m^3/s^2]$. The ionosphere group delay is given by

$$\tau_{gd}^{iono} = \frac{40.31}{f^2} STEC. \tag{3.8}$$

In dual frequency (S/X) VLBI the group delays of the different bands have frequency dependent contribution from the ionosphere. The band-dependent delays group delays can be used to express an ionosphere free linear combination where the contribution from $STEC$ has been eliminated. The ionosphere free observable τ_{gd}^{SX} is given by

$$\tau_{gd}^{SX} = \underbrace{\frac{f_X^2}{f_X^2 - f_S^2}}_{c_1} \tau_{gd}^X - \underbrace{\frac{f_S^2}{f_X^2 - f_S^2}}_{c_2} \tau_{gd}^S. \tag{3.9}$$

Assuming uncorrelated observations, the error of the SX combination can be estimated by (Sovers et al., 1998)

$$\sigma_\tau^2 = c_1^2 \sigma_{\tau_X}^2 + c_2^2 \sigma_{\tau_S}^2. \tag{3.10}$$

For S/X frequencies (2.3/8.4 GHz) the multiplying factors c_1 and c_2 for the variances of the respective group delays are approximately 1.081 and 0.081. The c_2 factor for τ_{gd}^X is small compared to c_1, which helps in reducing the contribution from the otherwise larger error for the S-band.

3.1.2.2 Tropospheric delay

The troposphere is the air mass that extends on average up to 20 km from the ground. Up to this level it contains 99 % of the water vapour and 80 % of the mass of the atmosphere. Most of the weather phenomena take place in this layer and thus atmospheric turbulence plays an important role in the troposphere delay. The propagating electromagnetic waves are refracted, delayed, and attenuated by the molecules in the troposphere. The delay is dependent on the variable refractivity along the signal propagation path. The refractivity is dependent on the partial pressures of the hydrostatic and non-hydrostatic (wet) part of the atmosphere, as well as temperature. The atmospheric gases are close to hydrostatic equilibrium. Hence the distribution of atmospheric gases is largely dependent on altitude and thus refractivity scales strongly with atmospheric pressure. The wet part is much more susceptible to strong variation due to weather phenomena and turbulence and hence more difficult to model. Thus, it is natural to separate the troposphere delay into hydrostatic and wet parts. Furthermore, the troposphere delay is highly dependent on elevation (e). Considering a simplified geometry, the delay scales as $1/sin(e)$, giving a rule of thumb that the delay close to the horizon is 10–15 times larger than zenith. Usually the station troposphere delays are determined at the zenith and then, using so-called mapping functions, mapped to the elevation of the source. Due to the strong elevation dependence, accurate mapping functions are crucial in determining the tropospheric delays. The delay along a path that minimizes the propagation time is given by

$$\tau_{trop} = 10^{-6} \int_S (N_h + N_w) \, dS, \tag{3.11}$$

where subindices h and w indicate the hydrostatic and wet parts. These subindices will be used throughout the text. From the integral we have the model for the tropospheric delay expressed as a sum of Zenith Hydrostatic Delay (ZHD) and Zenith Wet Delay (ZWD) scaled with their respective mapping functions. The slant delay is given by (Davis et al., 1985)

$$\tau_{trop} = mf_h(e) \ \text{ZHD} + mf_w(e) \ \text{ZWD}, \tag{3.12}$$

where the respective elevation (e) dependent mapping functions are denoted by $mf(e)$. This delay can be extended to take into account azimuthal variations by including gradients. Then, the tropospheric slant delay is given by

$$\tau_{trop} = mf_h(e) \ \text{ZHD} + mf_w(e) \ \text{ZWD} + mf_{grad}(e)[\text{G}_\text{n} \cos \alpha + \text{G}_\text{e} \sin \alpha], \tag{3.13}$$

where G_n and G_e denote North and East gradients, respectively. The hydrostatic part (ZHD) can be modelled as

$$\text{ZHD} = \frac{[(0.0022768 \ \pm \ 0.0000005)]P_0}{1 - 0.00266 \cos(2\phi) - 0.00000028 \ H}, \tag{3.14}$$

where P_0 is total atmospheric pressure in hPa at the antenna reference point and ϕ and H are the geodetic latitude and height of the station (Saastamoinen, 1972). At sea level the approximate magnitude of the ZHD is 2.3 m and the ZWD 0–30 cm. While the ZHD constitutes $\sim$90% of the total tropospheric delay and is very well modelled *a priori* according to Equation 3.14, the remaining ZWD is considerably more difficult to handle. The water vapor content can vary very rapidly during one day and cannot be eliminated with multi-frequency observations as with the ionosphere. Because of this, troposphere is considered as one of the main error sources in geodetic VLBI. It is expected that troposphere determination can be improved by observing in two directions simultaneously. For this purpose some VGOS sites will have two co-located next-generation telescopes (so called twin telescopes).

3.1.2.3   Mapping functions

Typically the mapping function that relate the delay in the zenith to the slant direction follow a continued fraction form (Herring, 1992)

$$mf(e) = \frac{1 + \dfrac{a}{1 + \dfrac{b}{1 + c}}}{\sin{(e)} + \dfrac{a}{\sin{(e)} + \dfrac{b}{\sin{(e)} + c}}}. \tag{3.15}$$

The mapping function coefficents can be determined based on atmospheric models or observations. The coefficents have been determined from e.g. ray-tracing through radiosonde profiles or numerical weather models. One way the mapping functions

differ is that they require different amount of *in situ* information from the sites. Some can be used in the absence of any meteorological data. For example, the widely used New Mapping Functions (NMF) (Niell, 1996) take as input the day-of-year (DOY), station latitude, and station height. By incorporating numerical weather models, the mapping functions can be extended to include meteorological parameters from a Numerical Weather Model (NWM) in the absence of measured data. This approach was first demonstrated with the Isobaric Mapping Functions (IMF) by Niell (2000). In a newer set of mapping functions called VMF1 (Böhm et al., 2006a), the coefficients are derived using meteorological data from NWM and ray-tracing. VMF1 is currently recommended for global applications in the IERS Conventions 2010 (Petit and Luzum, 2010). An empirical alternative is the Global Mapping Function (GMF), which is derived from VMF1 and can be thought of as an averaged version of VMF1. GMF together with Global Pressure and Temperature model (GPT), can be used in the absence of external pressure/ray-traced values. In the following, two of the mapping functions, NMF and VMF1, as well as GMF/GPT are described briefly.

3.1.2.4   New Mapping Functions and Isobaric Mapping Functions

The New Mapping Functions (NMF) (also called Niell Mapping Functions) (Niell, 1996) are empirical mapping functions that take DOY and station latitude and height as input parameters. They are based on the continued fraction shown in Equation 3.15. For the hydrostatic part the coefficients a_h, b_h, and c_h are parametrised as sinusoidal functions of latitude and time and corrected for changes in station height. The wet part is based solely on interpolated latitudes. These coefficients $a_{h,w}, b_{h,w}, c_{h,w}$ were determined for latitudes between 15° and 75° on 5° intervals by ray-tracing for nine elevation angles from 3° to 90°. The phases for coefficients are referenced to January 28th. The mapping functions were validated against radiosonde measurements.

The improved version of NMF, Isobaric Mapping Functions (IMF) (Niell, 2000), uses NWM data from Goddard Space Flight Center Data Assimilation Office (DAO) (Schubert et al., 1993) to determine the a coefficient. The b and c coefficients were again determined empirically. Unlike NMF, IMF are provided on a 2.5°×2.0° grid.

3.1.2.5   Vienna Mapping Functions 1

Similar to the NMF and IMF, the Vienna Mapping Functions 1 (VMF1) (Böhm et al., 2006a) are based on the continued fraction in Equation 3.15. VMF1 refers to the latest version of the Vienna Mapping Functions. Its earlier version is called simply VMF (Böhm and Schuh, 2004). In VMF the b and c coefficients were fixed to values from at the time latest NMF and IMF for the hydrostatic and wet parts, respectively.

For VMF1 the b and c parameters were re-determined using data from European Centre for Medium-Range Weather Forecasts (ECMWF) 40-year re-analysis (ERA40) data for the year 2001. The improved hydrostatic b and c coefficients were no longer symmetrical with regard to the equator, as this was found to influence station heights in some cases. This also led to the need to recompute the ray-traced a parameters.

VMF1 provides the *a* parameter with 6 h resolution for individual sites and on a global 2.5°×2.0° latitude-longitude grid. The values are made available by the Vienna University of Technology (IGG Vienna, 2018). The provided values also include predictions based on ECMWF forecasts that can be used in the analysis of real-time data.

3.1.2.6   Global Pressure and Temperature model and Global Mapping Functions

The Global Pressure and Temperature (GPT) model and the Global Mapping Functions (GMF) combined together form an empirical slant delay model (Böhm et al., 2006b). The model is based on 3 years of monthly mean profiles from ECMWF ERA40 data from 1999 to 2002. The mapping function coefficients are provided as a spherical harmonics expansion of degree 9. They contain mean and annual terms and the phase is fixed to January 28th. GMF/GPT assumes a constant lapse rate of −6.5°C/km and the pressure is reduced from an exponential model based on standard atmosphere. Pressure, temperature, and hydrostatic and wet *a* coefficients are used as output parameters. An improved version to GPT/GMF called GPT2 was introduced by Lagler et al. (2013). It uses a longer time period from 2001–2010 and more pressure levels of the ECMWF ERA40 data. The temporal variation is increased to include semi-annual terms. The model now also includes mean, annual, and semi-annual terms for the lapse rate, which in GMF/GPT were held constant. Instead of fixing the phases in GPT2 they are estimated. In addition to the parameters provided by GMF/GPT, GPT2 outputs lapse rate and water vapour pressure. As such, the GPT2 output can be used directly with standard VMF1 routines (Lagler et al., 2013), hence the omission of GMF2 in its name.

3.1.3   Station displacements

As discussed in Section 2.1, the Earth's crust deforms due to tidal- and non-tidal effects. These cause displacements in the station positions which need to be corrected before transforming the baseline vector from the ITRS to GCRS. The displacements for each phenomena can be derived from their geophysical descriptions. These are presented in great detail in the IERS Conventions 2010 (Petit and Luzum, 2010). In general these phenomena can be modelled accurately enough so they can be computed *a priori*. On the other hand, because they affect the observed parameters, VLBI can be used to estimate the associated geophysical effects and coefficients.

3.1.4   Radio source structure

An ideal radio source for geodetic VLBI observations is a stable pointlike source. However, some radio sources exhibit structural variations on a milliarcsecond level, which poses a problem in determining the position of the radio source as a single point. In parts of the VLBI product chain, such as scheduling, variations in source structure affect the expected observed flux. Typically the source structure is taken into account by representing the source by a set of Gaussian components (Gipson,

2012b). As the accuracy of the VLBI observations increases, the effect from currently dominant error sources decrease, in which case the effect of the radio source structure can become significant (Souchay and Feissel-Vernier, 2006). In addition to extended structure, some sources have temporal variations in flux. The variability requires continuous monitoring of the current (and prospective) geodetic sources. For this purpose the Bordeaux VLBI Image Database (BVID) provides images of the observed geodetic VLBI sources at S- and X-bands (Fey and Charlot, 2000).

3.1.5 Antenna-related mechanical effects

In addition to geophysical effects, observed delays are also affected by mechanical effects related to the antenna. The main contributors for geodetic VLBI are the antenna axis offset and physical deformation due to thermal and gravity effects. The gravitational deformation is proportional to the antenna size and structure, and thus most prominent in extremely large antennas such as the Effelsberg radio telescope (Bach and Kraus, 2015). A widely used model for antenna deformations was derived by Nothnagel (2009).

The VLBI observations are referenced to the point connecting the elevation and azimuth axes of the antenna. However, due to the mechanical structure of the antennas, these axes do not always intersect physically. In this case, the offset between them needs to be accounted for in the analysis.

The materials in the structure undergo deformation due to changes in the ambient temperature. This causes antenna-specific deformations, which change the shape and size of the reflector as well as the supporting structures. Most antennas are directly exposed to the weather. Some VLBI antennas are located within a protecting radome with a more controlled temperature environment. However, even then the thermal deformations can cause larger than millimetre-level variations in the antenna reference point. The temperature deformation can be monitored by e.g. an invar rod embedded in the telescope base, such as at the Onsala 20 m telescope (Haas et al., 2015).

3.2 VLBI – from observations to geodetic parameters

The VLBI data production pipeline from the observations to the estimation of geodetic parameters of interest consists of many steps but the process can be divided into a few main steps. In general, the description given in this section refers to the legacy S/X observations. Here we have used the distinction of observations, producing the interferometric data, and data analysis. This division can seem somewhat arbitrary. The different steps of an VLBI experiment are intrinsically connected. The results from the analysis can be used to improve the VLBI pipeline as a whole. An example is the improvement of scheduling approaches based on the obtained accuracy of the target parameters. In this section the procedures involved in the different steps are explained from a combination of theoretical and practical

point of view when it comes to the data analysis process and the work done in Papers II and III. In the next chapter, the VLBI operations are discussed in the framework of the International VLBI Service for Geodesy and Astrometry (IVS) (Nothnagel et al., 2017) and the transition to future VGOS observations.

3.2.1   Scheduling

The first task in the VLBI observation process is to schedule the observations. A schedule is provided to each participating station. It includes instructions for the telescopes as to which sources they should observe at a given time. The schedule also contains procedures on e.g. observing modes so that the SNR targets needed are reached. The schedule lists scans in the session, source positions and models, antenna parameters, antenna specific equipment, and frequency configurations. The frequency setup includes channel number, frequencies, bandwidths, sampling (typically 1 or 2 bit), and recording mode. In the scheduling terminology an *observation* is an observation to a source on a single baseline. A *scan* is a collection of all the simultaneous observations made to the same source. Thus, in a multi-baseline network a scan (usually) consists of many observations. If the network consists of only the minimum two telescopes, a scan and an observation are equal. Furthermore, depending on the network geometry, multiple sub-networks may also participate in different scans simultaneously. Multiple station- and network-dependent conditions have to be met when the observation schedule is created. The main inclusion criterion for a source is that it is visible (and not below elevation cut-off angle) at all the stations that are to be included in the scan. If a source is visible, the next step is to estimate the flux densities that can be attained on each baseline. From the flux density the expected Signal-to-Noise Ratio (SNR) can be computed to check whether the SNR target is met. The SNR of a VLBI observation can be calculated as (Thompson et al., 2017; Shaffer, 2000)

$$\text{SNR} = \frac{\nu F \sqrt{2 \cdot B \cdot T}}{\sqrt{\text{SEFD}_1 \cdot \text{SEFD}_2}}, \tag{3.16}$$

where $\text{SEFD}_{1,2}$ are the System Equivalent Flux Densities (SEFD) for antennas 1 and 2, F is the source flux density, T is the integration time, B is the observed bandwidth, and ν is a factor which includes corrections for e.g. instrumentation and correlator type. The factor of two in the square root is due to the Nyquist sampling criterion. From Equation 3.16 we see that higher SNR can be achieved by increasing the recorded bandwidth, increasing observing time, using better antennas (larger size, lower SEFD), or by observing sources with greater flux density.

The schedule structure depends on the pool of radio sources, the participating stations, and the target parameters of that particular VLBI session. As a result, the schedule is a combination of several different selection criteria. For example, the 1-hour Intensive sessions are scheduled on a predominantly East-West baseline because these orientations are most sensitive to variations in Earth's phase of rotation (UT1-UTC) (Nothnagel and Schnell, 2008). A typical way to optimise a VLBI schedule is to aim at a maximum number of scans per station, while still maintaining a good

observation geometry. A good observation geometry is linked to both sky coverage and elevations at individual stations. The number of scans that a telescope can participate in is connected to the slewing time it takes to switch between sources as well as source flux densities and antenna properties, which dictate the on-source time. All of these considerations are linked to the antenna specifications as well as to its location within the network. Maximising the number of scans via minimal slewing time can lead to clustering of sources and subsequently to a sub-optimal sky coverage. The sky coverage also has a time-dependency that needs to be considered. In general, sources should be selected so that the typical variation period of phenomena such as atmospheric effects is covered. For troposphere delays this time span is normally on the order of 1 hour or less. Furthermore, observations at both high and low elevations are needed in order to de-correlate parameters such as the troposphere and station clocks (Gipson, 2010). A widely used scheduling package for geodetic VLBI is SKED (Gipson, 2012b), which originates from the NASA Goddard Space Flight Center (GSFC). More recent alternatives include the scheduling module VIE_Sched (Sun et al., 2011) in the Vienna VLBI Software (VieVS) (Böhm et al., 2012). These scheduling software share many common features, which are essential in selecting sources that meet the minimal criteria. However, there are differences in e.g. how the sky coverage and number of simultaneous sources are determined. As for now SKED is used to create the operational VLBI schedules for regular IVS sessions. VieVS has been used in many regional studies, such as observing southern radio sources with the AuScope VLBI Array (McCallum et al., 2017).

3.2.2   Observations and data acquisition

In the next stage the observations are carried out by following the pre-computed schedule. As VLBI does not require identical antennas, the individual station architectures and procedures differ somewhat. However, the main stages of the process are very similar for every telescope. The most commonly used telescope type in geodetic VLBI, see e.g. Baver et al. (2013), Baver et al. (2014), and Baver et al. (2015), has Cassegrain optics. The electromagnetic signal from the radio source is reflected via main and sub-reflectors and directed into the waveguide/antenna feed, where the signal is converted into a voltage. Phase calibration tones are injected at this stage as well. Because the received signal is extremely weak, it needs to go through an initial amplification stage which involves a Low-Noise-Amplifier (LNA). The amplified signal is mixed with a Local Oscillator (LO) signal and heterodyned to multiple Intermediate Frequencies (IFs), and down-converted to base-band frequency/video frequency channels. Nowadays most stations have switched from analogue back-ends to fully digital back-ends (DBE), which can handle tasks where previously separate instruments (such as channelizer) were needed. The signal is digitized, time-tagged using a precise local frequency standard (hydrogen masers) (Sovers et al., 1998), and recorded on hard drives or transferred in real-time. Improvements in circuit technology has made it possible to digitize signals that were previously analogue. This has lead the analogue back-ends (ABEs) to be replaced by digital back-ends (DBEs). DBEs have several advantages over their analogue predecessors, including

the possibility to handle higher data rates, scalability, reproducibility, stability, and better radio-frequency interference (RFI) tolerance. Several DBEs were developed during the last years.[2] A widely implemented DBE product is the Digital Base-Band Converter (DBBC), which was conceived by Gino Tuccari and produced by HAT-Lab[3]. The development of the DBBC started in 2004 (Tuccari, 2004) and so far includes three generations, DBBC1 (2004–2008), DBBC2 (2007-) and DBBC3 (2015-) (Tuccari et al., 2006; Tuccari et al., 2010; Tuccari et al., 2014). In 2011 the Onsala Space Observatory (OSO) acquired a DBBC2, which was subsequently operated during tests in parallel with an old setup using a MarkIV (Whitney, 1993) analogue back-end. Widely used recorders, such as the Mark5 and Mark6 (Whitney, 2002; Whitney, 2004; Whitney et al., 2010; Whitney and Lapsley, 2012), record to disk modules that can be physically sent to the correlator for processing. With modern high-speed internet connections (in VLBI context referred to as e-transfer) the data can be sent to the correlator electronically from some sites. Alternative recording systems include FlexBuff (Mujunen and Salminen, 2013). The advantage of a FlexBuff as opposed to the Mark-series are that it does not need any dedicated hardware, but consists of implementation guidelines and standards. Furthermore, it is capable of simultaneously recording and streaming the data to the correlator, but has the disadvantage of not recording to modules that can be conveniently shipped. This may be necessary for sites with low bandwidth network connection.

The observations are controlled with the Field System (FS) (Himwich et al., 2003). It is used to interpret the sked files and convey the information for the antenna and the recording equipment. Its tasks include reading in the schedule and procedure file information and passing it to the antenna as well as executing correct observational procedures for each scan. The FS also records auxiliary data, such as the difference between GPS time and the formatter, cable delay values, and meteorological data during the experiment. These data are valuable in the subsequent correlation and data analysis steps. The software is largely automated, but depending on the observation procedure at the station, the pre-experiment setup may need human input. Pre-experiment tasks include e.g. pointing tests and measurement of system sensitivity.

3.2.3   Producing and processing the interferometric data

After a session is observed the data from all telescopes are shipped to a centralized correlator. In the future increased data amounts could also lead to the need for de-centralized correlation, as will be discussed in the next chapter. The process from raw observations to geodetic delay products can be divided into two steps: correlation and fringe-fitting.

---

[2] http://ivs.nict.go.jp/mirror/technology/vlbi2010-docs/dbe_comparison_130121.pdf

[3] http://www.hat-lab.com/hatlab/

3.2.3.1   Correlation

The objective of the correlator is to multiply the observed signals in order to produce an interference pattern which has its maximum at the true delay. The combination is done in a pairwise manner on the baselines so that the cross-correlation function of the observed voltages is maximised. This is done by shifting the recorded signals by different amounts of lags; lag corresponds to the time delay between the observations. The cross-correlation function is given by

$$R(\tau) = \frac{1}{T} \int_0^T V_1(t)V_2^*(t - \tau)dt, \tag{3.17}$$

where T is the averaging interval, $V_{1,2}$ are the bit-streams of the recorded voltages at stations 1 and 2. The peak is found by trying different lag-values (τ). Prior to averaging the cross-correlated bit-streams high fringe rates due to variable baseline geometry, clock offset between the stations, and the Doppler shift caused by the rotation of the Earth during the observation need to be accounted for. For this purpose the correlator applies a sufficiently accurate correlator model to compute the *a priori* geometric delays. The Doppler shift effect can be corrected by performing a so-called fringe stopping, which involves multiplying the cross-correlated bits by sine and cosine functions (Sovers et al., 1998). In the end, the output from the correlator includes the complex visibilities, extracted phase calibration tones, and the SNR information.

3.2.3.2   Fringe-fitting

After the observations are correlated the raw correlator output is still likely to contain high residual delays and delay rates. Sources for these errors are linked to insufficient modelling and instrumental errors. The error sources include the limited accuracy of the applied *a priori* correlator model. Furthermore, atmospheric delays and the ionosphere exhibit time-variations, which are difficult or impossible to model *a priori*. The Haystack Post-Processing System (HOPS) is a widely used software for this stage. The principal task during the post-processing is fit the phase samples $\phi(\omega_i, t_j)$ for all observed frequency channels with phase, group delay, and phase rate. The phase samples are Fourier transformed to the delay and delay rate domain. In this domain a correlation amplitude peak is searched for. This peak is used as the *a priori* value for a bilinear least-squares fit for the measured phases, given by

$$\phi(\omega, t) = \phi_0(\omega_0, t_0) + \frac{\partial \phi}{\partial \omega}(\omega - \omega_0) + \frac{\partial \phi}{\partial t}(t - t_0), \tag{3.18}$$

where the phase delay is defined as $\tau_{pd} = \phi_0/\omega_0$, the group delay as $\tau_{gd} = \partial\phi/\partial\omega$ and the phase delay rate as $\dot{\tau}_{ph} = (1/\omega_0)(\partial\phi/\partial t)$. The post-correlation processing produces four observables: phase delay, group delay, delay rate, and amplitude of the coherence function. The precision of the phase delays are superior compared to group delays, but to determine the phase delays an unknown integer number of 2π ambiguities have to be resolved. In contrast, when the group delay is determined from the best-fit slope of the phase delays across all the frequency channels, the group delay

precision is inversely proportional to the largest channel separation, i.e. the spanned bandwidth. This technique is called the Bandwidth Synthesis (BWS) (Rogers, 1970). This makes group delay the currently best observable available for geodetic purposes. However, the group delays obtained with BWS also contain ambiguities. These are proportional to the greatest common divisor of the channel spacing within the individual bands. The obtained parameters are stored into a database, which are subsequently used as input for the geodetic VLBI analysis software.

3.2.4 Data analysis

The last stage in the VLBI experiment flow observed on S/X-band is the data analysis where the observed group delays are fitted to the VLBI delay model (see Section 3.1.1). The obtained geodetic parameters can then be further interpreted in order to study the underlying geophysical phenomena. The general analysis usually follows the process of computation of $o - c$ and subsequent adjustment, as shown in Figure 3.2. However, the intricacies of the analysis process are dependent on the choice of the VLBI analysis software package as well as the format of the input data. An important aspect when selecting the analysis software is to consider the level of automation that can be achieved. Some software packages can perform a full geodetic adjustment completely automated, whereas others require manual input in different stages of the analysis. Before estimating geodetic parameters from the VLBI data, further pre-processing steps are needed to deal with ionosphere calibration and ambiguity adjustment. The available software packages differ in the their capability to complete these tasks. The VLBI analysis software are used not only in this parameter estimation stage, but also by the correlators to compute the required *a priori* delays (Souchay and Feissel-Vernier, 2006). In the following subsections a brief description of the database formats, most common VLBI software packages, the estimation process, and aspects of automated analysis are discussed. Emphasis is given to the software packages most utilized for the papers appended to this thesis: calc (Ma et al., 1990), νSolve (Bolotin et al., 2014) and c5++ (Hobiger et al., 2010).

3.2.4.1 VLBI database formats

The most common formats used in geodetic VLBI are the Mark3-database (Mark3-DB) format (Gipson, 2012a), National Geodetic Survey (NGS) cards[4], and most recently vgosDB (Gipson, 2014). These formats differ significantly in their structure and usual application in the standard VLBI data processing chain. The database formats used for the work presented in the papers attached to this thesis were Mark-3DB (Paper I) and NGS cards (Paper I, Paper II, Paper III, and Paper IV). Mark3-DB is a binary format, which together with the calc/Solve VLBI analysis software (Ma et al., 1990) has been the main combination used for creating the IVS VLBI data products. The databases contain the observational data, and optionally, complete sets of auxiliary info, such as geophysical models and meteorological data.

---

[4]`ftp://cddis.gsfc.nasa.gov/pub/reports/formats/ngs_card.format`

NGS databases are formatted in ASCII and they contain only a subset of the data included in the more comprehensive binary database formats. The databases are labelled with a version number (usually from 1 to 4), which refer to different stages of the data processing. Version-1 databases contain the raw correlator output. Version-4 databases have been processed for the removal of group delay ambiguities, ionosphere, outliers, clock-breaks, and station performance, and they contain auxiliary data from the station log-files (Gipson, 2012a). The new vgosDB has been developed to replace the Mark3-DB format (Gipson, 2012a). The new format is designed to be flexible and deal with VGOS aspects such as high data rates and a new type of observable (broadband delays).

3.2.4.2   Analysis software

Currently there is a wide variety of VLBI analysis software packages available for estimating geodetic parameters. The packages are developed and maintained by multiple institutions and agencies. The abundance of choice and adoption of different analysis software gives redundancy and a chance to compare the results. This helps to avoid the situation where the geodetic parameters provided by the VLBI community could have software related hidden biases. On the other hand, it poses a challenge in bringing the different software into agreement. This issue has been investigated in comparison campaigns, such as the VLBI Analysis Software Comparison Campaign 2015 (VASCC) (Klopotek et al., 2016). Some of the most used software packages include calc/Solve (Ma et al., 1990) and the Solve upgrade νSolve (Bolotin et al., 2014), c5++ (Hobiger et al., 2010), OCCAM (Titov et al., 2004), and VieVS (Böhm et al., 2012). Most of these software packages are open-source and available either on-line or by request.

c5++

The c5++ space-geodetic analysis software has been developed jointly by National Institute of Information and Communications Technology (NICT), Japan Aerospace Exploration Agency (JAXA), Hitotsubashi University, and most recently Chalmers University of Technology. The software package is designed with straightforward and robust multi-technique combination in mind. The analyst can combine observations from VLBI, SLR, and GNSS on an observational level. It follows the latest IERS Conventions (Petit and Luzum, 2010).

c5++ is run from a binary executable using configuration files, or alternatively, invoking the commands directly from command line. The configuration files include the geophysical models, *a priori* data, and parameter estimation options. This also includes cable delays and meteorological data available in the station log-files from the FS. It supports input data in NGS, K5 raw correlator output (KOMB), and the new vgosDB formats. It also includes additional tools to process the calc-related Mark3-DB databases without the calc libraries (Hobiger et al., 2010). Additionally, data can be read and output in Solution INdependent EXchange (SINEX) format. This is particularly useful when combining multiple techniques in the analysis.

The software is fully automated and does not require any user input apart from the initial configuration files/command line calls. This also includes ambiguity estimation and ionosphere calibration, meaning it can be used to process databases which do not yet include corrections for these. Thus, it is able to process e.g. NGS Version-1 files that are generated directly from the correlator output. Along with calc/Solve/νSolve, c5++ is the only other software package capable of performing the aforementioned tasks. Parameters are estimated using iterative Gauss-Markov least-squares adjustment. The VLBI module can estimate all relevant geodetic parameters: EOP and LOD, station positions, source positions, ZWD, and station clocks. The ambiguity resolution and ionosphere calibration is a recursive process. When resolving the ambiguities the correlator output databases for X- and S-band are analysed using a simple parameter estimation configuration. The ambiguities are assigned for each band according to their ambiguity spacing. At this stage the $o - c$ is modelled by a clock function, where the clock offset term is allowed to differ between S- and X-bands. This solution is done in an iterative manner and when the ambiguities are resolved (i.e. the solution converges), the results including the estimated ionosphere correction are output in NGS format. Figure 3.3 depicts the schematics of an automated c5++ VLBI analysis process.
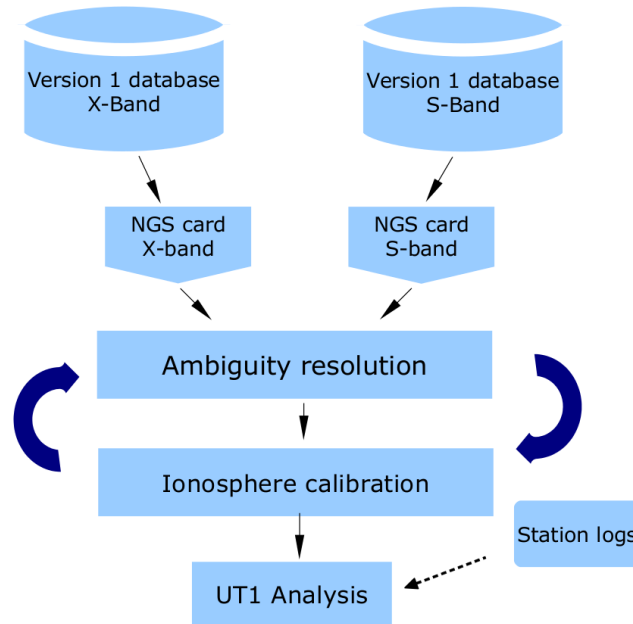

Figure 3.3: Flowchart of the automated VLBI data analysis process with c5++ (Paper II).

calc/Solve/νSolve

calc/Solve (Ma et al., 1990) is a VLBI analysis software package that has been developed for over 40 years at the Goddard Space Flight Center (GSFC). It consists of two main parts: calc and Solve. Calc produces databases that contain the

computed c part. This includes theoretical VLBI delay and delay rates, most of the partial delays used in the adjustment process, such as EOP, station positions, and source coordinates as well most geophysical models (e.g. ocean loading, atmosphere loading, and tides) (Fey et al., 2009). Solve uses the databases produced by calc and performs least-squares parameter adjustment. Recently, a completely new software νSolve (Bolotin et al., 2014), a GUI version of interactive Solve; a preprocessor to Solve, has been created. When using Mark3-DB database format the processing with calc is done in a similar manner regardless whether Solve or νSolve is used. Both Solve and νSolve can be used to estimate group delay ambiguities and ionosphere calibration. The automatic ambiguity resolution algorithm is derived from the standard Solve version, with the added capability of handling variable ambiguity spacing within baselines or one baseline in a session. The clock breaks can be detected in semi-automatic and manual mode. νSolve can estimate clock polynomial coefficients, ZWD, tropospheric gradients, station positions, sources coordinates, EOP and their rates (excluding nutation angle rates), baseline vectors and clock offsets, and antenna axis offsets.

3.2.4.3 Pre-processing data and automated analysis

The observed group delays provided by the correlator contain effects that need to be removed before the data are ready for final analysis. The group delay ambiguities obtained via BWS contain ambiguities, which need to be removed first, after which the ionosphere-free delays can be determined. Instabilities in the station clocks, called clock breaks, are sometimes present and seen as abrupt jumps in the delays. These should be identified and handled before the final analysis as well.

Currently c5++ does not have a dedicated automated way to detect clock breaks. However, the software is very capable of analysing VLBI data from Intensives and simulated data. Due to the short duration of the Intensives, clock breaks during one hour are extremely rare. Furthermore, simulated data do not include instrumental or other random issues apart from Gaussian noise. In νSolve, processing a regular 24-hour VLBI session the clock breaks are normally detected after semi-automated ambiguity estimation. This is usually done in manual or semi-automated fashion by starting a new clock polynomial at the time of the break. Furthermore, at this stage (at least for the moment) it is possible to suppress crude outliers.

Ambiguity estimation

As discussed in Section 3.2.3.2 the group delays determined with BWS (Rogers, 1970) from dual-band observations on X- and S-band contain an unknown integer number of ambiguities. The multi-band group delay observable is given by $\tau_{gd} = \partial\phi/\partial\omega$ (see Section 3.2.3.2). It is given by the gradient of the best-fit line of the phase samples in the frequency-phase domain. The group delay ambiguity spacing τ_{amb} is given by

$$\tau_{amb} = \frac{1}{\Delta f}, \tag{3.19}$$

where Δf is the greatest common divisor (gcd) between the frequency spacings. A typical frequency setup for IVS rapid turnaround sessions are 50 ns ($\Delta f = 20$ MHz) and 100 ns ($\Delta f = 10$ MHz) for X- and S-band, respectively.

For multi-baseline sessions the ambiguities are distributed between the baselines included in a particular scan. In this case the ambiguities need to be distributed such that triangle misclosures for the group delays in subsets of three stations are avoided.

In VLBI software the ambiguity estimation process differs between c5++ and νSolve/Solve. c5++ performs the adjustment iteratively and fully automatically in conjunction with ionosphere calibration. νSolve has support for both manual and automatic ambiguity estimation. The automatic ambiguity estimation algorithm in Solve is called GAMB. The implementation in νSolve follows GAMB closely. In νSolve, the analyst attempts to solve the ambiguities in a semi-automated iterative manner. It is also possible to shift ambiguities for a single observations. The ionosphere calibration is applied separately after the ambiguities are resolved.

The difference in residual delays on X- and S-band should be within a few centimetres. A typical X-band ambiguity spacing of 50 ns corresponds to approximately 14 m. For cases where the residual is close to half of the ambiguity spacing (e.g. ± 25 ns) the right choice of an ambiguity shift is not clear. In these cases it is important to be consistent w.r.t. different baselines. It also helps in case there is a clear trend in the residuals which is not due to the ambiguities (e.g. an under-parametrized station clock could show up as a polynomial in the residuals). In this case the likely right choice fits this trend and the remaining residuals can be accounted for in later stages of the analysis.

Inspecting the analysed data from c5++ a failed ambiguity estimation can be detected as a large post-fit WRMS of the delays. Sometimes this also shows up as large single outliers in the delay residuals, where the failed detection is usually close to 50 % of the ambiguity spacing. These observations will then likely be suppressed in the later stages of the analysis. However, if the residuals are overall large but show no clear outliers the overall quality of the solution is likely to be degraded.

Robust ambiguity estimation for Intensive sessions

In c5++ the VLBI data are analysed using iterative least-squares (L2-norm) adjustment. The software also applies this method for the ambiguity estimation. In Paper III we investigate an alternative ambiguity estimation approach for IVS Intensives based on the L1-norm. In L2-norm minimisation a best-fit solution is found by minimising the squared sum of the (weighted residuals), as given by Equation 3.20

$$\min(v^\mathsf{T} P v), \tag{3.20}$$

where v is the residual vector and P the weight matrix. The residual vector v is the difference between the model and observations, given by

$$\mathbf{v} = A\mathbf{x} - y, \tag{3.21}$$

where A is the design matrix, x is the vector of unknown parameters, and y is the observation vector. However, its performance as an estimator is depends on how the errors in the observations are distributed. The L2-norm is a maximum likelihood estimator (MLE) if the observation errors come from a Gaussian distribution. In VLBI analysis this is usually a valid approximation in the presence of observation noise. However, compared to the group delay error estimates from the correlator, which are around 15 ps (Takahashi et al., 2000), the ambiguities manifest as large jumps in nanosecond scale. The group delays containing ambiguities are also in practice distributed randomly within the observations in a session. This leads to a situation where the error profile no longer follows Gaussian distribution, which in some situation causes the L2-norm to underperform when doing the adjustment to detect the ambiguities. Since any unresolved ambiguities will significantly degrade the overall fit and propagate as errors to the target geodetic parameters, it is vital that they are detected before further analysis.

L1-norm on the other hand is more robust against large outliers, which is how the ambiguities look in the data. Since the L2-norm minimises the squared sum of the residuals, the observations with ambiguities (i.e. large residual to the model) have an disproportionate influence on the sum, which will also degrade the fit for the observations with no ambiguities. In L1-norm minimisation the optimising condition is

$$\min(\mathbf{p}^\mathsf{T}|\mathbf{v}|), \tag{3.22}$$

where $\mathbf{v}$ is the residual vector and p the weight vector. As opposed to the L2-norm, only absolute values of the residuals contribute to the sum, and thus large outliers do not influence the solution similarly. The disadvantage of the L1-norm is that it can not be implemented as simply as the L2-norm. The argument in Equation 3.22 is not differentiable around $\mathbf{v} = 0$ due to the absolute value. With the L2-norm this limitation does not exists, and the condition in Equation 3.20 can be solved by differentiating and solved for the unknown parameters, giving the adjusted values $\hat{\mathbf{x}}$. For the L1-norm the sign change at zero must be dealt with by introducing slack variables for v and x, which are given as a differences $\mathbf{v} = \mathbf{u} - \mathbf{w}$ and $\mathbf{x} = \alpha - \beta$. With this formulation the adjustment reduces to a linear programming problem. We implemented the L1-norm estimation as an external Python application for the c5++. Figure 3.4 illustrates how the L1-norm application is related to the estimation process in c5++. To validate the usefulness of the L1-norm it was compared to the L2-Norm. In stage one, using both estimation methods the ambiguity and ionosphere calibration were estimated for 1835 Intensive sessions observed on Kokee–Wettzell baseline between 2001–2015. In stage two the ionosphere and ambiguity free databases produced by both methods were analysed using only the L2-norm to estimate UT1-UTC w.r.t IERS EOP 08 C04. This is because at this stage the errors are largely Gaussian, thus making the L2-norm the more suitable choice. The success rate of the two approaches was assessed by comparing the post-fit residuals from stage one and the UT1-UTC estimates and their formal errors from stage 2. The L1-norm was found to increase the number of successes by 5 % (out of all sessions). Figure 3.5 illustrates an example where the L1-norm
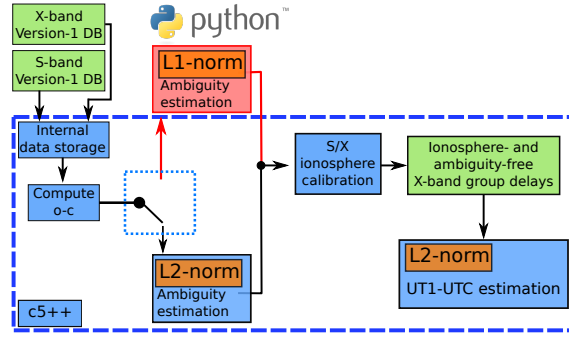
Figure 3.4: L1-norm application implemented into c5++. The schematics show the program flow for the estimation process in c5++.
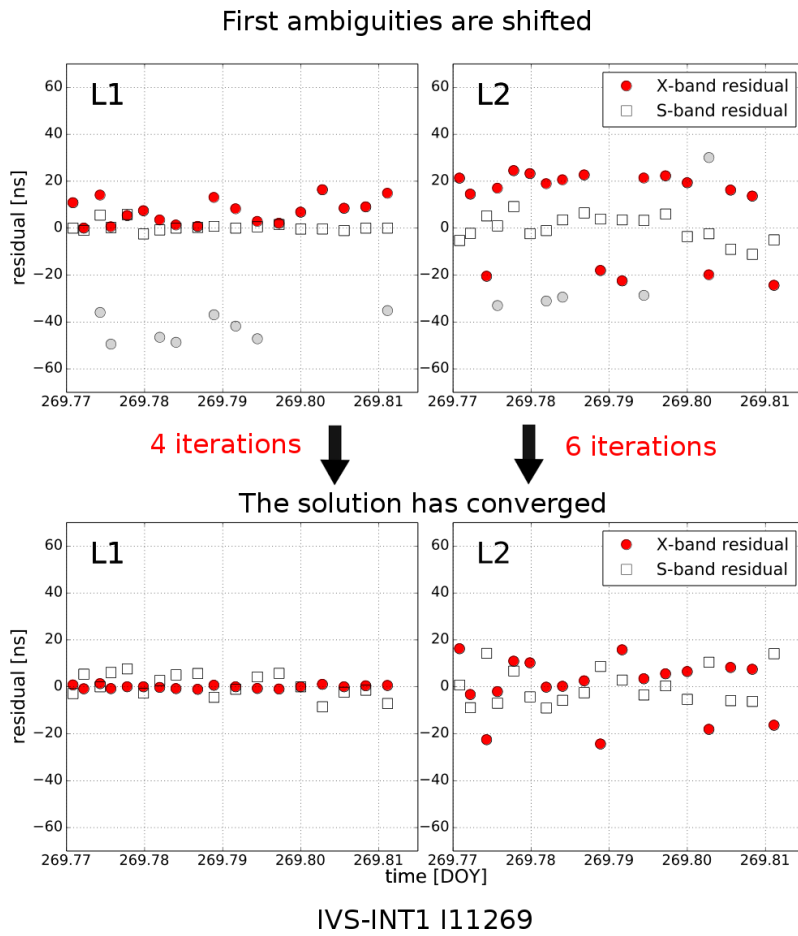
Figure 3.5: En example of ambiguity estimation using L1- and L2-norms in which using the L1-norm leads to a better result. The session is IVS-INT1 I11269 and it has ambiguities in the X-band. The upper row shows the residuals for the L1-norm (left) and L2-norm (right) after the first ambiguities are shifted. The grey markers show the value of the residual before it was shifted in the current iteration. In the bottom row are the residuals after the solution has converged. The L1-norm solution converges in 4 iterations, while the L2-norm takes 6 iterations. The L1-norm is able to detect the ambiguities correctly and converges more quickly. The L2-norm (right) does not detect the ambiguities correctly and they end up in the residuals.

is able to correctly detect the ambiguities leading to a greatly improved model fit. This improved estimation method has been used successfully by the Geospatial Information Authority Japan (GSI), who analyse the IVS-INT2 sessions operationally.

Handling auxiliary data

The auxiliary data, normally the cable delay and *in situ* meteorological data (usually only local barometric pressure is used), i.e. data extracted from the station log-files may contain outliers or biases due to e.g. cable wrap and thermal issues, and instrumental errors. Sometimes the log-files might also be corrupted due to problems that occurred during the experiment. When processing Mark3-DB these auxiliary data are included in the database at the early stages of the processing. At this stage the values can be manually screened for suspicious values using the *pwxcb* utility that is included in calc/Solve. In practice the analyst often enables/disables the auxiliary data also in later steps and by investigating the overall fit can assess whether the solution is improved. When doing an automated analysis from start to finish, screening this data is more challenging. Because there are no definite *a priori* models on how the local barometric pressure and cable delay should behave, it is challenging to detect erroneous values. For meteorological data one does have a certain normality assumption based on the station location on how the weather conditions should look at a given time of year. Additionally, if for example the barometric pressure drops to e.g. zero at certain point, this could be flagged as an error in the reading. Overall, 'realistic looking' biases, however, can be almost impossible to detect. For cable delay the situation is even more challenging, since the variation is dependent on temperature, cable wraps and twists, and other possible instrumentation problems.

3.2.4.4 Estimation process

The manner in which the parameter estimation process is carried out in VLBI analysis depends on the number of observations (group delays) as well as the target parameters. The number of observations is largely dictated by the length of the session and the number of participating antennas. Typically, VLBI sessions are carried as either 24-hour (e.g. IVS-R1, IVS-R4, TRF) or 1-hour (IVS-INT1, IVS-INT2, IVS-INT3) sessions. The 24-hour sessions are normally designed for EOP determination or strengthening the TRF and CRF. The 1-hour sessions are aimed for low-latency UT1 determination, and they are observed mostly with a single-baseline network. For example, an IVS-R1 session has up to approximately 6000 observations. On the contrary, an Intensive session has approximately 15–30 observations. This leads to very different initial conditions for the analysis.

In the adjustment the difference between the number of observations (n) and number of estimated parameters (u) gives a measure of the redundancy of the system (degree-of-freedom). The system needs to be sufficiently overdetermined for parameter adjustment to converge. Parameters such as station clocks and troposphere, for which no *a priori* information is available, always need to be estimated. The station clocks

are typically estimated as a quadratic polynomial (three polynomial coefficients) and optionally as continuous piece-wise linear (CPWL) offset on top of the polynomial. Essentially the clocks can only be determined w.r.t. a reference, and therefore one station is always fixed as the reference clock. Thus, for 1-hour single-baseline Intensives the standard parametrisation for the clock requires 3 unknowns. Whereas ZHD are typically modelled the ZWD have to be estimated at each site individually. The standard parametrisation for ZWD is to use 60 min CPWL functions. In the case of Intensives only one offset is estimated. For Intensives the target parameter UT1-UTC is estimated once, leading to six unknowns. Due to the small number of observations in Intensives it is difficult to improve the parametrisation by decreasing the estimation intervals, since this would bring the redundancy to a very low number. For Intensives this means that all the other parameters such as polar motion and station coordinates must be fixed to *a priori* values. Furthermore, in the case of Intensives the observation geometry is designed to maximise the sensitivity to the target parameter UT1-UTC. The small number of stations makes it more manageable to correlate and process the observations in a timely manner, which is crucial for Intensives as they aim to provide daily UT1-UTC series with sufficient accuracy for the users.

For a 24-hour session this type of parametrisation totals to $25 \times N_{stations}$ CPWL estimates for ZWD and $28 \times (N_{stations} - 1)$ clock coefficients. This leads to a redundancy which makes it possible to estimate a full set of EOP and stations position from the 24-hour session. In order to avoid singularity the station positions are usually constrained by No-Net-Rotation and No-Net-Translation (NNR/NNT) conditions. Typically station positions can be assumed to stay constant over a 24-hour period and as such one offset to the *a priori* per session is adequate. In a case where the station is known to have experienced a substantial non-linear shift w.r.t. its *a priori* (e.g. due to an earthquake), it is necessary to exclude it from the NNR/NNT conditions to avoid errors propagating into the observation network. Analogously, if radio source positions are estimated (by combining multiple sessions in a global solution) a source with known instability in its position due to e.g. changes in structure, should be excluded from the NNR conditions.

Especially with sessions that have a large number of observations there is a better possibility to try to optimise the estimation intervals to capture the true variation of the parameters. Some stations can at times have so turbulent a troposphere that in order not to degrade the results a shorter estimation interval is needed. More educated guesses in the analysis process can thus depend on how experienced the analyst is.

3.2.4.5   Automated analysis of Intensive sessions

The IVS Intensive sessions (see more details in the following Section 4.1.2.2) are aimed at providing daily UT1-UTC estimates. In order to minimise the turnaround time and to provide the results in near-real time, automated analysis of the sessions is required. The analysis of the Intensive sessions is mainly done following the processes described in Sections 3.2.4.3 and 3.2.4.4. In order to eventually realise a

fully automated real-time analysis it is necessary to know which factors are most important for the UT1-UTC accuracy. Paper II investigates to what degree the accuracy of the UT1-UTC w.r.t. IERS EOP 08 C04 (later on referred to as UT1-UTC accuracy) in automated analysis is dependent on the choice of analysis strategies, external information, and availability of accurate *a priori* data.

The data set consists of the IVS-INT1 sessions on Kokee–Wettzell baseline Version-1 databases (see Section 3.2.4.1) initially selected from 2001 to 2015. In total 1669 sessions were used in the analysis. Sessions for which Version-1 database or auxiliary data were not available were excluded from the analysis. Furthermore, if the ambiguity estimation was not successful for a given session, as detected by large UT1-UTC residuals ($|v_{\mathrm{UT1-UTC}}| > 1000\mu s$) or formal errors ($\sigma_{\mathrm{UT1-UTC}} > 50\mu s$), the session was also excluded. Starting from database Version-1 the sessions were analysed in a fully automated mode using c5++ VLBI analysis software (See 3.2.4.2 and Figure 3.3).

The analysis was divided into three parts. The first part investigate whether the choice of mapping function and applying external information has significant impact on the UT1-UTC accuracy. This has relevance for near-real time analysis, since mapping functions such as VMF1 (see Section 3.1.2.5) require that external information (*a* coefficient) is available, whereas empirical mapping functions such as GMF(GPT2) (see Section 3.1.2.6) can be used without external input. The other external data are provided in station log-files, which includes meteorological and cable delay data. In case the local barometric pressure is not available, the mapping functions need to use global models, such as GPT2. In the second part the impact of *a priori* EOP data to the UT1-UTC accuracy is studied with extensive Monte Carlo simulations. Lastly, the standard parametrisation of the Intensive analysis is extended by estimating one constrained station position as opposed to fixing both stations.

The impact of mapping functions was investigated by analysing the data using four strategies. They are formed by the choice of mapping function and applying/not applying station log-files. When station log-file information is not used in the analysis, the pressure data are provided by GPT2, and no cable delay is applied. Thus, the strategies are: VMF1 with and without logs, GMF(GPT2) with and without logs. By analysing the sessions consistently and fully automated in one software, we can by differencing the resulting time series and computing a UT1-UTC WRMS to determine the impact of each strategy. The impact of mapping function choice was found to be not significant (with or without external meteorological data), the differences being on the order of 0.01 μs. This result is not that surprising considering that the duration of an Intensive session is only one hour, and the ZWD is estimated only as one offset. When using the same mapping function with and without applying the external information, the UT1-UTC WRMS w.r.t. IERS EOP 08 C04 decreased approximately 0.4 μs when cable delays and local pressure were applied. Nonetheless, the improvement is modest, compared to the general UT1-UTC accuracy, which was on the order of 17.6 μs with station log-files and 18.0 μs without them.

The general assumption is that using the auxiliary data should improve the results. However, there can be periods where those data are biased for a long period

of time. In those cases one might see deviations in the target parameters which can only be detected as erroneous given a long-term trend to which to compare. For example, the effect of cable delay errors propagating into the UT1-UTC estimates can be seen in the sessions observed between late 2013 and early 2014. Figure 3.6 depicts the difference between the UT1-UTC estimates from analysing with and without station cable delay. The points for which the residuals differ by more than 5 μs are highlighted with red markers. In the bottom two figures the UT1-UTC residuals are shown as a function of the corresponding cable delay RMS values computed from the station log-files for Kokee and Wettzell. The shift in the residuals can attributed to anomalous cable delay measurements at Wettzell during the time period. As such, undetected problems in the cable delay measurements have the potential to have a large impact on the UT1-UTC estimates. This shows, that even if external information is available, it is necessary to make sure it is not corrupted by e.g. faulty instrumentation.
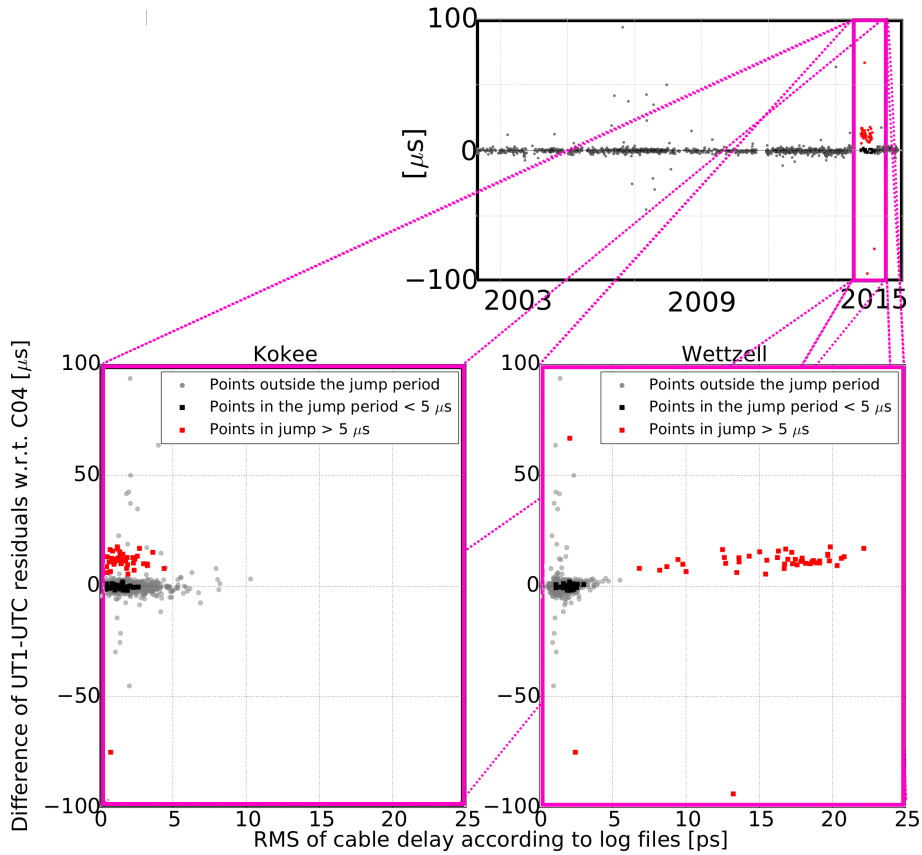
Figure 3.6: Jump in UT1-UTC residuals due to anomalous cable readings in Wettzell station log-files. The upper figure shows the difference of UT1-UTC residuals w.r.t. IERS EOP 08 C04 time series obtained with and without applying the cable delays. The differences in residuals larger than 5μs are highlighted with red markers. The lower figures depict the same differences of the UT1-UTC residuals plotted against the cable delay RMS at the respective stations. The inspected time window is illustrated by the magenta boxes. For Kokee (bottom left) the anomalous data points are not correlated with suspicious cable readings. For Wettzell the highlighted data points correlate well with sessions having higher than normal cable readings.

One possible solution could be to automatically accumulate the cable readings as a function of antenna orientation and temperature from the station and in this way build an *a priori* model for normal cable behaviour or request information from the station when an anomaly occurs. However, even in this way it would be necessary to receive detailed information from the stations about possible instrumentation changes, which could cause discontinuities. For now, collecting this information would involve a great deal of manual work.

Because Intensives have a low number of observations and limited geometry it is not possible to increase the parametrisation or estimate other EOP apart from UT1-UTC. Thus station positions, polar motion, and Celestial Pole Offsets (CPO) are fixed to their *a priori* values. This makes accurate *a priori* data important for the analysis of Intensives, since errors in these will be partly absorbed by the target parameter UT1-UTC. The *a priori* EOP values used in the analysis were from IERS 08 C04 and they represent the most accurate EOP values available. These are available with a latency of 30 days, this limits their usefulness for real-time analysis. For real-time analysis lower latency but lower accuracy EOP sources, such as the daily solution by the United States Naval Observatory (USNO) (called USNO finals) or IERS Bulletin A[5] are needed. The weekly IERS Bulletin A provides EOP predictions forward up to 90 days, but only the first week or less is used. It also includes error estimate models for the standard deviations of UT1-UTC and the polar motion components (x_p, y_p). For polar motion and UT1-UTC the standard deviations are given by

$$\sigma_{x_p,y_p} = 680{\cdot}D^{0.80}, \tag{3.23}$$

and

$$\sigma_{UT1-UTC} = 250{\cdot}D^{0.75}, \tag{3.24}$$

where D is days elapsed since the Bulletin A was issued. The impact of *a priori* polar motion and UT1-UTC to the UT1-UTC estimates can be investigated by adding an offset to the EOP 08 C04 *a priori* values. The offsets represent an error in the *a priori* EOP values and they are drawn from a normal distribution $N(0, \sigma^2)$. The σ for polar motion and UT1-UTC are provided by Equations 3.23 and 3.24, respectively. Because new bulletins are released once a week, $D = 6$ gives the most outdated *a priori* EOP. The 6 day period was divided into into 24 time steps. For polar motion the first day was further divided into 17 steps to cover the update period of USNO finals with better resolution. All 1669 sessions were analysed with 20 Monte Carlo iterations for each time step. Each time step is thus represented by 20 UTC-UTC WRMS values determined from the 1669 sessions. These values were averaged to yield a mean WRMS and error estimates for each time step. The offsets for polar motion and UT1-UTC were applied in separate runs to isolate the impact of the two. The baseline UT1-UTC accuracy with IERS EOP C08 04 available was determined from the previous part of the analysis using the GMF(GPT2) without station log-files as 18.04 μs. The impact of outdated polar motion values was an increase in the UTC-UTC WRMS by 4 μs to 22 μs during the first day. At day 6

---

[5]`https://datacenter.iers.org/eop/-/somos/5Rgv/latest/6`

the UT1-UTC WRMS was over 53 μs. The increase in the mean UT1-UTC WRMS during the 6-day period is shown in Figure 3.7.
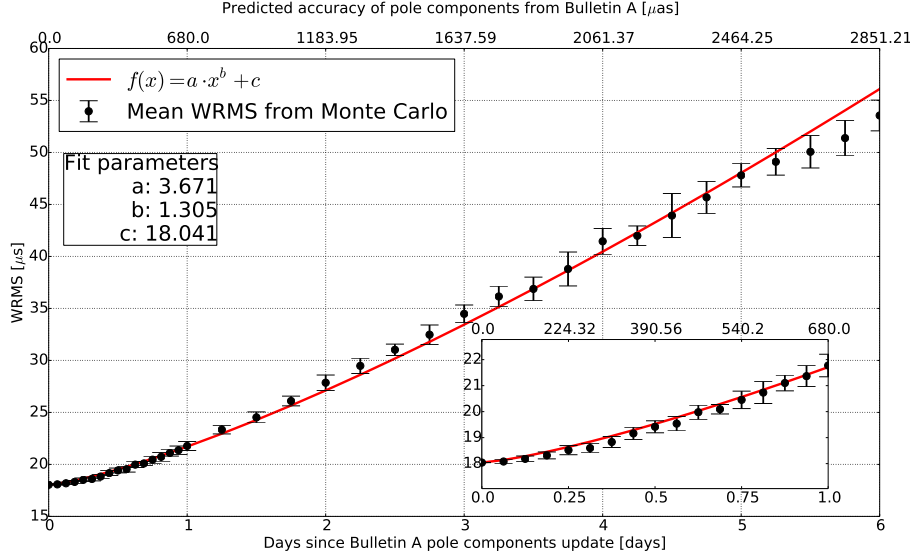

Figure 3.7: The increase in mean UT1-UTC WRMS as the *a priori* polar motion become outdated. The data points represent a mean WRMS from the 20 Monte Carlo iterations of analysing the 1669 Intensive sessions. The top-axis shows the corresponding standard deviations of the polar motion components that were used in generating the offset-values.

The *a priori* UT1-UTC values do not have a similar impact to the UT1-UTC accuracy as polar motion. Because the UT1-UTC is estimated in the analysis, it is sufficient if the *a priori* UT1-UTC is within a range where the linearised parameter is still close enough to the 'true' value. Estimating a constrained station position at the non-reference station had negligible impact on tight constraints, while with more loose constraints the solutions degraded. In their current form the number of observations in the Intensives is so low that the parametrisation and choices for alternative analysis approaches are restricted. Improving the overall performance of the Intensives might be possible by introducing additional external data, improving the observation geometry, or increasing the number of observations. When considering near-real time analysis of the Intensive sessions the most crucial factors for UT1-UTC are related to the reliability of the available *a priori* data. This is in some sense also more relevant, because the Intensives are a product that is targeted for users who need the UT1-UTC estimates with low latency. The degradation in UT1-UTC accuracy after one day due to the latency of the *a priori* polar motion can be 10 times larger than the difference between using or ignoring the external information from station log-files (i.e. local barometric pressure and cable delay).

Chapter 4

Transition from legacy systems to geodetic VLBI with VGOS

The IVS (Nothnagel et al., 2017) is a best-effort international collaboration of organizations involved in geodetic and astrometric VLBI. It is one of the four services that contribute to the operations of the IERS. IVS supports its different parts in providing accurate geodetic data products to the end-users. It includes seven components that together form the basis for delivering and developing the VLBI data products. These include centres for coordination, operations, data analysis, technology and development, as well as the correlators and network stations. These together help integrate VLBI as a geodetic technique to GGOS. VLBI as a technique has evolved greatly from its beginnings. Over time the technical and procedural improvements have also been incorporated into the day-to-day data production services of the IVS. The number of network stations has also increased greatly from only a handful of active stations. When the decision was made to establish GGOS in 2003 the IVS set up a working group, IVS working Group 3 (WG3), to define the requirements and actions needed by the VLBI community to answer the GGOS challenges. This was the start to the ongoing project which is in principle set to modernize all aspects of geodetic VLBI. In 2016 the IVS Directing Board developed a roadmap called *Strategic Plan of the IVS for the Period 2016–2025*, summarised by Nothnagel et al. (2016), to address the issues that need to be solved in transitioning to operational VGOS observations. In this chapter the current (also referred to as 'legacy') operational VLBI services, the upcoming VGOS, and the challenges involved in realizing and transitioning into the VGOS era are discussed.

4.1   VLBI with legacy network and equipment

During the transition period the legacy network is still needed to provide the data products that are used by the geodetic community. Even when the VGOS network will be fully operational the legacy network will likely participate alongside in order to provide continuity in the geodetic time series. Compared to VGOS the legacy network is characterized by larger and slower antennas, lower data rates (and thus

less need for storage and transfer capabilities), and narrower spanned frequency range.

4.1.1 IVS VLBI Observation network

Currently there are 31 IVS network stations that take part in different VLBI experiments in the IVS observing program. Many sites have already begun the steps towards VGOS operations. Some stations have recently been upgraded to (or replaced by) a next-generation station (e.g. Tsukuba station has been replaced by Ishioka station).

Figure 4.1 depicts the distribution of a current network stations and sites with upcoming VGOS antennas. Uneven station distribution has long been a problem with the geodetic VLBI observing network. As evident from the map the majority of the stations are located on the Northern Hemisphere. Furthermore, compared to the Northern Hemisphere, the Southern Hemisphere is largely covered by water, which leads to both fewer stations and reduced common visibility. This has been a problem especially for CRF determinations (Jacobs et al., 2013) leading to reduced position accuracy for sources in the southern sky. Naturally any new station increases the strength of the network, but from a scientific point of view a better impact could be achieved with a more even station distribution. This again is also an issue of available resources for building new stations. The issue of inclusion of new telescopes both to the network as well as observing plans has been investigated in e.g. Hase and Pedreros (2014) and Paper IV, respectively.

Current geodetic VLBI is observed using S-band and X-band, centred around 2.3 GHz and 8.4 GHz, respectively. The observing bandwidth is usually divided into 8 channels for X-band and 6 channels for S-band. The base-band signals are limited to channels with a width of a few MHz. A typical bandwidth choice is 8 MHz. The data rates are usually between 128–512 Mbps. The total bandwidth and the length and number of scans determine the data rates and storage space needed at the telescopes. For regular IVS-R1 sessions At the Onsala 20 m telescope the data are usually recorded with a rate of 256 or 512 MB and the number of scans is typically 400 to 450 resulting in approximately 1.5–3.5 TB of data. Furthermore, the data volume directly affects the workload of the correlators, which have to receive and correlate the data from all the telescopes in an experiment, and scale their resources accordingly.

The Mark5-series (see e.g. Whitney (2002), Whitney (2004), and Whitney et al. (2010)) has been a common choice amongst VLBI stations for a recording system. The Mark6 system (Whitney and Lapsley, 2012) is the next-generation recorder and is designed to handle VGOS data rates. The data rates achievable by these recorders are listed in Table 4.1.

An alternative to the fixed-hardware solutions is FlexBuff (Mujunen and Salminen, 2013). It has the advantage of simultaneously recording and streaming the data to the correlator. Furthermore, it is not tied to a specific hardware solution but rather guidelines, which makes adoption and modification more flexible. The FlexBuff data rates used in operational observations have reached 2–4 Gbps. However, tests
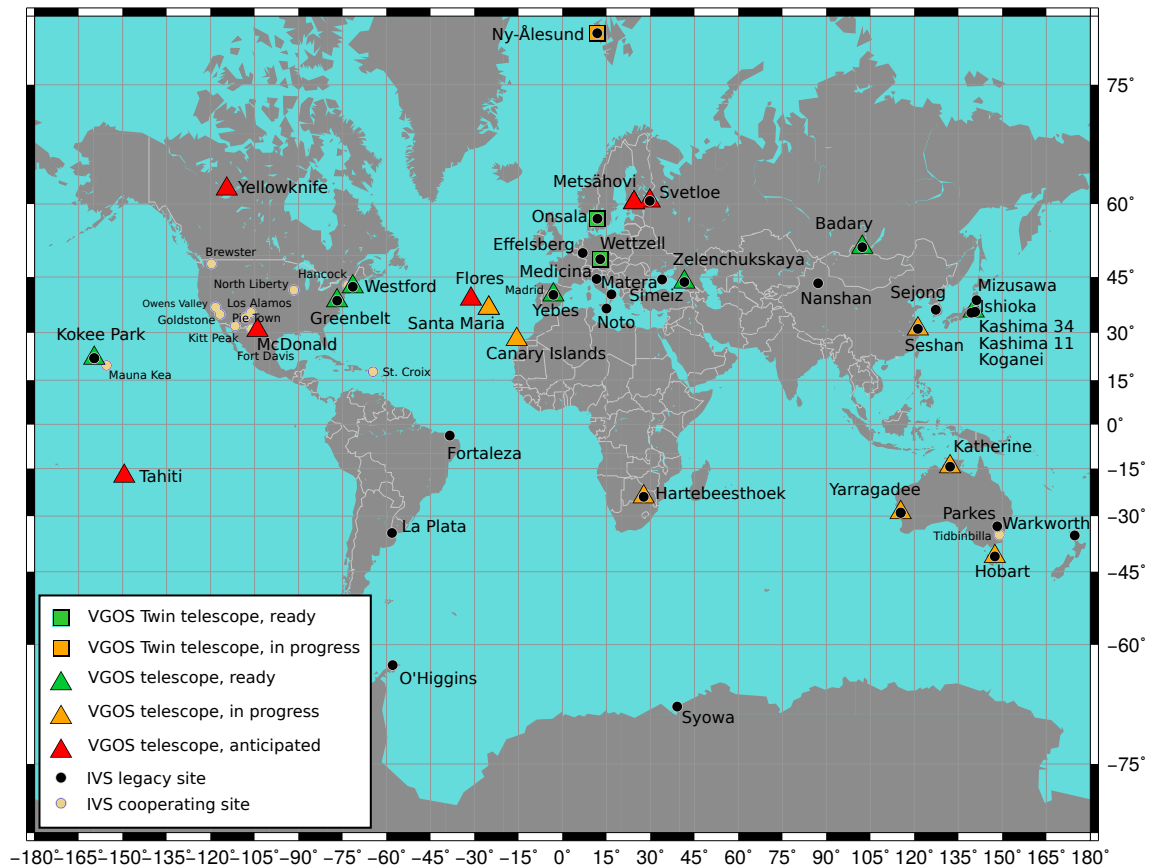
Figure 4.1: IVS observing network. The stations include VGOS sites (single telescope: triangles, twin telescope: squares; green: ready, orange: construction/hardware installation in progress, red: anticipated), legacy IVS sites (black circles), and IVS cooperating stations (beige circles).

have shown that with modern hardware and sufficient storage FlexBuff can reach a recording rate of 32 Gbps (Simon Casey, personal communication, February 9th, 2018).

Table 4.1: Introduction year and recording rates of Mark 5/6 VLBI recording systems.

Model	Introduced	Recording rate (Gbps)
Mark 5A	2002	1
Mark 5A+	2006	1
Mark 5B	2005	1
Mark 5B+	2006	2
Mark 5C	2011/2012	4
Mark 6	2012	16

Many stations have been shifting from analogue back-ends to the digital alternatives discussed in Section 3.2.2. Not only do the earlier generations of DBBC fulfil requirements of current observations, but the early adoption of these systems has

prepared many stations for digitizing their signal-chain in preparation for future systems. However, with mass-adoption of new systems it is recommended that checks are made that these systems perform on a similar level and do not introduce unknown instrumental biases to the results. For example, in 2011 the Onsala Space Observatory acquired a DBBC2, which subsequently was installed and operated in parallel with the MarkIV (Whitney, 1993) analogue back-end for testing purposes (Paper I).

The main parts of the signal chains at the stations include the antenna feeds, frequency converters, and samplers. For the legacy stations these meet the criteria for S/X observations at the required data rates. The feed has to be designed specifically for the intended frequency range. Hence, the capabilities of the instrumentation are largely tied to the requirements of current operations. The specifications are also intrinsically linked to the antenna size. The telescopes in the legacy network are generally large, which limits their slewing speeds. However, reducing the antenna size would mean the need to increase the recorded data rate and spanned bandwidth to compensate for loss of sensitivity.

4.1.2   Current IVS sessions

At the moment the IVS observing program includes several different session types. The most frequent ones are Rapid turnaround sessions (IVS-R1 and IVS-R4; in total two sessions per week) and Intensive sessions (IVS-INT1, IVS-INT2, IVS-INT3; in total eight sessions per week). The typical session length is 24 h with the exception of the 1-hour Intensives. Approximately every three years a 15-day CONT campaign of consecutive 24-hour sessions is observed. Its purpose is to produce a state-of-the-art data set, which can be used to gauge the performance limits of the network and to provide scientist in the field with an extremely high quality continuous set of observations.

In addition to these, the observing plan includes sessions for TRF and CRF determination, regional sessions to study or strengthen observations in particular area, astrometric/geodetic sessions in connection with the Very Long Baseline Array (VLBA), and Research and Development (R&D) sessions aimed at a particular interest. In the following two subsections the Rapid turnaround and Intensive sessions are discussed in more detail.

4.1.2.1   Rapid turnaround sessions

The IVS-R1 and IVS-R4 are weekly 24-hour sessions beginning on Monday and Thursday, respectively. In total 104 rapid turnaround sessions are observed in a year. Their main purpose is EOP determination. They also strengthen the TRF by adding to the history and number of station position measurements. The turnaround target for a session is 15 days. For example, during 2016 the turnaround target for IVS-R1 was met (median turnaround 15 days), but exceeded for IVS-R4 (median turnaround 39 days). For 2017 the median turnaround times were 15 days for IVS-R1 and 17 days for IVS-R4. This reflects the variability in a product chain, which works on best-effort basis and many tasks need to be performed manually. The network

consists of some core stations with additions based on availability and the need to replace core stations that needed to drop out. Usually the observing network consists of around 8–10 stations.

4.1.2.2 Intensive sessions

The aim of the Intensive sessions is to provide a time-series of daily UT1-UTC estimates. These estimates are needed to provide GNSS with timely updates of UT1. Satellite techniques cannot directly access UT1-UTC, but are only capable of observing LOD. This causes any UT1-UTC estimates from GNSS to drift from the true value. For GPS this is approximately 170 µs over a period of four days (Thaller et al., 2005). As VLBI is the only technique capable of directly observing UT1, the GNSS rely on the timely UT1 updates it provides. The Intensives are 1-hour sessions observed daily in three different session types through the week: IVS-INT1, IVS-INT2, and IVS-INT3, and together they cover the whole week. The standard observing plan is: IVS-INT1 from Monday to Friday at 18:30 UTC (18:45 on Friday) using Kokee (Hawaii, USA) and Wettzell (Germany). IVS-INT2 on Saturday and Sunday at 7:00 UTC using Wettzell and Tsukuba (Japan), and IVS-INT3 on Monday morning 7:00 UTC using Kokee, Wettzell, and Ny-Ålesund (Spitsbergen, Norway).

The short session duration and number of participating stations is the result of a combination of factors. The Intensives are observed on extended East-West baselines since this geometry is particularly sensitive to UT1-UTC. This limits the choice of stations that can fulfil the geometry requirements. Furthermore, the number of observations obtained from these sessions must be sufficient for accurate UT1-UTC determination for the purposes of providing GNSS with the updated estimates. Generally the INT1 sessions have 15–20 observations and INT2 around 20–30. This difference is due to geometry and the Tsukuba 32 m antenna (until December 2016) being large and fast for its size on the INT2 baseline, which reduces the on-source time leading to more observations. The operation of Tsukuba 32 m station ended in December 2016, and the telescope was dismantled. It was succeeded by the new Ishioka 13 m telescope, which has been able to attain similar high number of observations. Additionally, because of the busy observing schedule, it can be difficult for stations to commit to daily sessions. Lastly, the short duration and small number of observations reduce the workload on the correlators, which contributes to the quick turnaround. In principle the turnaround time from observation to results is as quickly as possible. In practice this is between a few minutes and 12 hours. However, with automation the turnaround time has been in some instances reduced to just 4 minutes (Matsuzaka et al., 2008).

Automation can significantly benefit this type of routine operations when the processing chain is not dependent on manual input. On the other hand it is important that the automated steps are reliable and robust. However, from their introduction the Intensives have not performed as well as the formal errors from the schedule analysis suggests. There has been a great deal of effort to try to improve the quality of the UT1-UTC estimates from the Intensives. Areas researched include scheduling and source selection (Gipson and Baver, 2016; Uunila et al., 2012),

geometry optimisation (Leek et al., 2015), increased session length (Artz et al., 2012), and adding an additional station in tag-along mode (Paper IV).
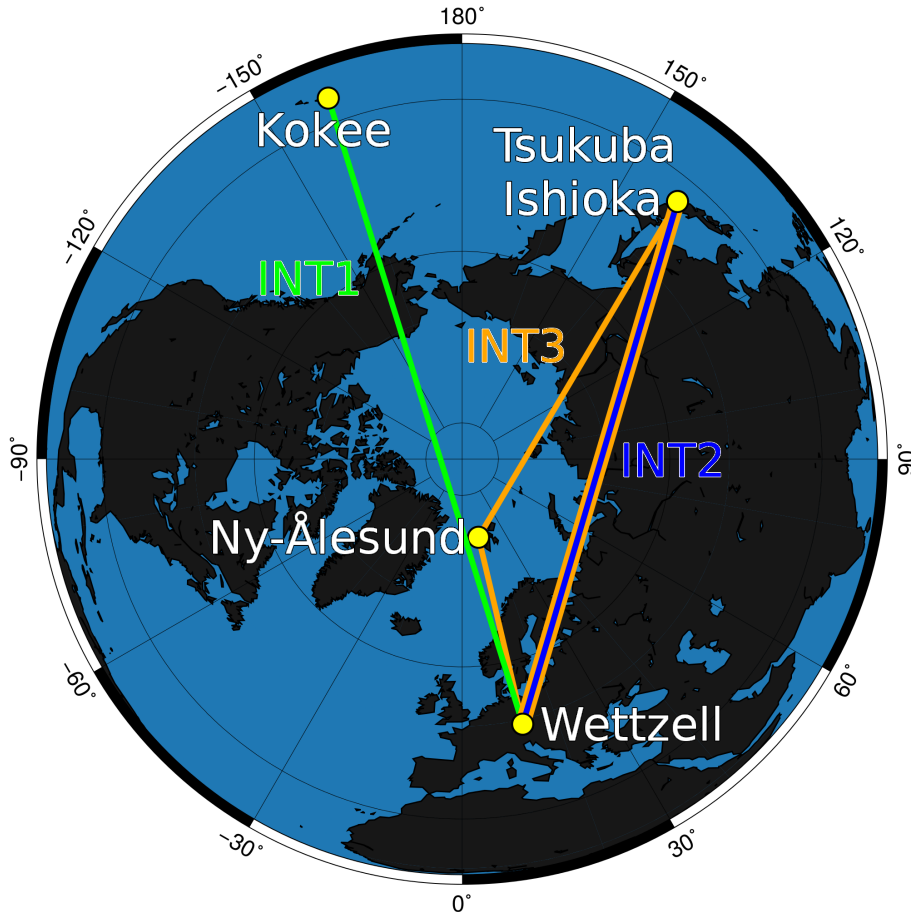
Figure 4.2: Observing geometries of the Intensives sessions. Three Intensive session types are observed: INT1 on Kokee–Wettzell baseline (green), INT2 on Tsukuba/Ishioka–Wettzell (blue), and INT3 on baselines among Wettzell, Tsukuba/Ishioka, and Ny-Ålesund (orange).

4.2   Towards the VGOS era

The VGOS design philosophy to achieve the required level of accuracy can be stated as follows: build new smaller fast-slewing antennas with broadband signal chains. This general idea is the result of a long investigation into the capabilities that effect the accuracy of the VLBI products. It is based on numerous assessments of the capabilities of the current legacy VLBI, feasibility simulations, advances in data storage and transfer, computing power, signal processing, receiver technology, and more. In this section an introduction is given to the current status of the VGOS project. In the following sections we discuss the goals and decisions that shaped how VGOS looks today: what problems have been solved and what still needs to be done.

The current and upcoming VGOS stations are depicted in the map of Figure 4.1. As can be seen many sites with the new VGOS telescopes will have a co-located

legacy antenna. An important step in phasing in the VGOS antennas and eventually phasing out the S/X antennas is to have a period of overlap in observations. This will ensure the continuity of the current geodetic time series as well as provide redundancy. Also, introducing new equipment often requires time to reach reliable full operations. Furthermore, it is likely that even when the number of VGOS antennas is enough to produce operational data, the legacy telescopes will be maintained at some sites to provide continuity or to serve another purpose, e.g. astronomy. A particularly interesting set of sites in the VGOS network will be Onsala, Wettzell, and Ny-Ålesund, as these sites will be operating two co-located VGOS antennas, commonly called *twin telescopes.* These sites are expected to be key locations in terms of reliability, as they can continue to operate even if there are technical problems with one of the antennas. Furthermore, twin telescopes provide a way to utilise scheduling strategies which take advantage of multi-directional observations for better resolving of the troposphere. Figure 4.3 shows the Twin Telescopes at Onsala Space Observatory (Elgered et al., 2017), which were inaugurated in May 2017 and are expected to be fully operational during 2018. The telescopes are identical in design with 13.2 m diameter reflectors.

Figure 4.3: The Onsala Twin Telescopes located at the OSO on the Western coast of Sweden (photo courtesy of Roger Hammargren, OSO).

4.3   VGOS goals

The goals for VGOS are both scientific and societal. Between 2003 and 2005 the IVS WG3 (Niell et al., 2006) determined the aims and requirements that would bring VLBI onto the required level of accuracy and timeliness. For this the IVS WG3 formed an action plan on how to fulfil the upcoming challenges to adopting a next-generation VLBI system. The report states the following goals as the guideline on which VGOS should be designed:

- Accuracy of 1 mm in station positions and 0.1 mm/year in station velocities

- Continuous monitoring of station positions and EOP

- Turnaround time of less than 24 hours for initial geodetic results

In general VGOS will not change the basic products that the IVS provides. The main products and tasks specific to VLBI will continue to be UT1, nutation and precession, the scale of the TRF, and CRF determination. The full set of goals specify accuracy, timeliness, frequency, and resolution targets for TRF, CRF, EOP and physical and geophysical parameters. An overview of these goals in terms of accuracy and timeliness are presented in Table 4.2, derived from the goal table in Niell et al. (2006).

Table 4.2: VGOS objectives for parameter accuracy and latency. The accuracy targets, frequency, temporal resolution, and turnaround time goals for the different parameters and VLBI products. These include TRF, CRF, EOP, and geophysical and physical parameters. The table is derived from Niell et al. (2006).

	Product	Accuracy	Timeliness
TRF	X,Y,Z time series (session)	2–5 mm	1 day
	Annual coordinates	1–2 mm	1 month
	Annual velocities	0.1–0.3 mm/y	1 month
CRF	Source coordinates	0.25 mas	1 month
	α & δ time series	0.5 mas	1 month
EOP	UT1-UTC	5 μs	Near real time
	Precession/nutation	20–50 μas	Near real time
	Polar motion	20–50 μas	Near real time
Geodynamics	Solid Earth tides	0.1 %	1 month
	Ocean loading	1 %	1 month
	Atmosphere loading	10 %	1 month
Atmosphere	Tropospheric parameters	1–2 mm	Near real time
	Zenith delay gradients	0.3–0.5 mm	Near real time
	Ionosphere mapping	0.5 TECU	Near real time

During years following the release of the IVS WG3 report, building on the work done by the VLBI community to realize operational VGOS, the planned types of products, their quality, and timeliness requirements for the core VLBI products (EOP, station positions, source positions) have become more detailed. The products are divided into four different categories: ultra-rapid, rapid, intermediate, and final. The goals for these products are specified in *Strategic Plan of the IVS for the Period 2016–2025* (Nothnagel et al., 2016). The ultra-rapid product is aimed for low-latency UT1-UTC estimation, given that scan-by-scan correlation is possible. The final product represents the weekly results for all of the core parameters: EOP, station coordinates, source positions. The details for these two products, representing the two extremities, are presented in Table 4.3 (adapted from Nothnagel et al. (2016)).

Table 4.3: Timeliness and accuracy goals for the ultra-rapid and final products of VGOS. The table is adapted from Nothnagel et al. (2016).

Product	Ultra-rapid	Final
Product epoch	Every 30 min	Every 3 h @ 3, 6,…24 h
Update epoch	Every 30 min	Every 7 d on day 3 at 12 h UT
Epochs to be updated	t–30…180 min	t–3 d…–10 h
Latency of last data point	30 min	7 days
Expected WRMS accuracy of target parameter		
UT1-UTC	7 µs	1 µs
PM	-	15 µas
Nutation offsets	-	15 µas
Station coordinates	-	3 mm
Source positions	-	15 µas

4.4 VGOS requirements – challenges and solutions

The goals of VGOS are ambitious and pose challenges for all aspects of future VLBI. In principle the accuracy goals can be achieved by careful system design. However, the effects from the timeliness requirements resonate on all levels of the VLBI product chain.

In order to be able to continuously provide data products in 24 h or less the stations and correlators must be able to manage their data storage and data transfer effectively. Compared to legacy VLBI the data volume is set to increase by up to two orders of magnitude. This will put the these capabilities to the test. Correlators will especially face a challenging situation: more data coming from a growing number of stations. To meet the goal of 24-hour turnaround the data will have to be transferred to the correlators using high-speed optical fibre connections. Most countries nowadays have comprehensive broadband coverage around heavily populated areas, but most telescopes are usually built in remote locations to avoid RFI. This last-mile connectivity problem needs to be considered when selecting sites for new VGOS telescopes. The prospect of including sites in completely new locations is an issue that needs to be addressed, because the current distribution of the existing telescopes is uneven between the Northern and Southern Hemispheres. Thus the observing network would greatly benefit from new sites for better EOP and CRF determination (Petrachenko et al., 2009).

In addition to improving the number and spatial distribution of the telescopes, also noted was the need to reduce the random errors of the delay observable. This includes contribution from the errors in individual observations, as well as stochastic effects of both the troposphere and instrumental errors, including frequency standards. The 1 mm accuracy requirement corresponds roughly to 4 ps of observation noise per scan (Niell et al., 2006). The improved observation accuracy will also increase the

impact of the radio source structure on the overall accuracy. In addition to error reduction, the need for improved observation and analysis strategies is also evident.

In the following subsections the approaches used to tackle the challenges with VGOS in the different stages of the VLBI product chain are discussed.

4.4.1   Observing plans and scheduling for VGOS

The observing plan and scheduling efforts for VGOS require many innovations in order to utilise the upcoming network of modern telescopes to its full potential. This also opens the way for many new possibilities. With fast telescopes capable of observing significantly more sources in rapid succession the pool of prospective sources is greatly increased. Furthermore, due to broadband receivers, radio sources that were previously too weak to observe are now added to the list of prospective sources. Additionally, with twin telescopes on sites such as Onsala, Ny-Ålesund, and Wettzell, the possible scheduling combinations grow significantly. However, it is quite clear that the observing plans and scheduling strategies that were developed during the legacy era may not be the optimal choice for VGOS observations. New approaches are needed.

A tentative operational VGOS observing plan has been presented by Petrachenko et al. (2014). It aims to improve on the current set of regular observation sessions based on the Rapid turnaround and Intensive sessions, which provide UT1 once daily and all EOP twice per week. The goal was set to incrementally increase the number of sessions until 24/7 observation capability is reached. The plan was drafted for a transition time period for 2015–2019 with full VGOS operations by 2020.

In the four year transition stage the VGOS network would observe one 24-hour session on Mondays and for the rest of the week four equally spaced 1-hour sessions. The plan is divided into three separate campaigns focusing on carrying out a 24-hour session, sustaining four 1-hour observing sessions daily, and and delivering initial geodetic products within 24 hours (being otherwise similar to the second campaign). In order to assess the expected performance of the network, simulations were carried with network configurations where the number of observing stations and the number of the daily 1-hour observing sessions increased gradually. These sessions were scheduled using VGOS sensitivities and slew rates for the antennas. The increments were eight stations observing in four sessions, 16 stations in eight, and lastly 30 stations for 24-hours. The simulations were compared against simulated R1, R4, and CONT11 networks.

The results showed that there is a major expected improvement in all target parameters with a fully operational 24-hour network. However, the number of observations for the VGOS sessions, while improved from R1, R4, and CONT11, did not meet the target of 120 observations per hour at the stations. The number of observations per time did not increase even with the inclusion of more stations or observing time. For the eight station configuration the low number is explained by inclusion of legacy antennas in the network. This was not the case however for the other two configurations. This indicates two things. Firstly, adding legacy telescopes to VGOS network need to be scheduled carefully in order not to degrade the overall

quality of the network. Secondly, to fully utilise the VGOS network the scheduling approaches used with the legacy networks need to be improved to accommodate the major changes in antenna specifications. Two prospective approaches for scheduling a session are source-centred and dynamic scheduling.

A prospective scheduling strategy for VGOS observations, which also addressed some of the shortcomings found in the 2014 Observing plan study (Petrachenko et al., 2014), was suggested in Searle and Petrachenko (2016). In order to utilise the network of new fast-slewing telescopes with wide-band receivers in a flexible manner it is necessary to consider the observing frequencies and geometry requirements to the source selection criteria. The attainable SEFDs depend on the used antennas, receiving equipment, and source strengths in the pool of used sources. In order to attain a good continuous observing geometry with maximum number of observations the observed sources must be selected so that as many as possible stations can observe with minimum idle time. For this purpose the study chose an opposite sky source-based scheduling strategy. Sources were selected every 30 seconds randomly in pairs from the opposite sides of the sky. The criteria for selecting the sources were that there should not be too recent observations made to either of them and that the selection would lead to equal amount of observations per source. By selecting the sources in this manner each station is likely to be able to observe at least one of the two sources. The target level for the delay precision improvement was chosen as 8 ps. This type of simple approach has the advantage that the scheduling itself is straightforward. Stations in the network can drop out and join in the observations based on their availability without the need to alter the scheduling approach or the schedule itself. It was found that, regarding the target geodetic parameters, the two most important factors were geometry and observation density. In order to reach the VGOS target of 1 mm positional uncertainty a station would need approximately 13000 observations. With a source pool of around 100 sources the EOP and stations positions solutions reached a satisfactory level. Regular observation intervals simplified the scheduling process, which also lead in total to a larger number of observations by having a high-level of station participation. This type of flexible scheduling is especially important in order to make the network robust against stations dropping out while maintaining continuous operation.

As an alternative, test of a dynamic scheduling concept have been carried out with the AuScope Array (Lovell et al., 2013), which includes three 12-meter telescopes located at Yarragadee in Western Australia, Katherine in the Northern Territories, and Hobart in Tasmania. A schedule was generated every 15 minutes for the three stations based on their availability. The observations were scheduled with VieVS for 1 Gbps observing mode on S- and X-bands. The scheduling software would then produce a daily VEX-file for the correlator. During the 8-hour test the stations were added and removed from the pool of available stations and it was ensured that the scheduler adapted dynamically to these changes. When the observations were correlated afterwards it was found that all baselines had detected good fringes. An important parameter for scheduling in flexible or dynamical manner is the time span for which the schedules are generated. For the test the 15-minute schedule generation interval was dictated by the limit that it takes to be able to resolve the troposphere

from the observations. However, it was noted that this will not lead to an optimal sky coverage during a standard 24-hour observing period. The legacy 24-hour sessions are scheduled for the whole network beforehand. In this way it is possible to optimize the geometry and sky-coverage for the duration of the observation period, which in turn will provide good quality geodetic products. However, this also assumes that the network geometry does not change during the observations. The issue on how to transition from the classic 24-hour scheduling paradigm to a continuous one that is able to quickly react to changes in the pool of available station, while still providing geodetic results with sufficient quality, is an important aspect in VGOS scheduling.

4.4.2   Flexible scheduling and improving the Intensives with a tag-along station

The Intensive sessions are to some degree fundamentally limited by the network geometry. Observing on a single baseline produces a relatively low number of observations. This restricts the parametrisation options significantly. As discussed in Section 3.2.4.5 the impact of choosing between different analysis strategies is relatively low, and the accuracy of *a priori* polar motion has more importance in terms of UT1-UTC accuracy. Thus, a logical next step is to change the initial conditions for the analysis. One way to achieve this is to extend the observing geometry with a third station. The most simple scenario where a station is added flexibly (in this case not regenerating the schedule after adding the station) to an observing network is to add the third station in a tag-along mode. This approach has been investigated in Paper IV. The aim of the study is to determine the optimal locations for an additional tag-along station in terms of UT1-UTC accuracy w.r.t. IERS EOP 08 C04 (referred to UT1-UTC in the following text). In this particular case a single-baseline Intensive network is appended with a tag-along station that has low enough SEFD to detected the scheduled sources and high enough slew rates to observe most of them when visible. The evaluation is done by extensive Monte Carlo simulations, in which the tag-along station is placed on a location selected from a grid of mutual radio-source visibility with the existing Intensive baselines.

The observing geometries for the study are contained in the VEX files of the 230 INT1 and 102 INT2 sessions observed during 2014. The VEX files contain the schedules for these sessions. These schedules were initially created for two stations and thus they are optimised for these particular stations. Starting with the intersection points on a global $2° \times 2°$ latitude–longitude grid the possible locations for the tag-along station were narrowed down to those where it could see all the sources observed in every schedule during the year 2014. This was done separately for the INT1 and INT2 sessions. The resulting grids for INT1 and INT2 were also combined to form an intersection grid INT1∩INT2. To quantify the level a that tag-along station can participate in the schedule we define a measure called Tag-Along Factor (TAF) which is the fraction of scans the tag-along station can participate in within a schedule. A 40 % participation corresponds to a TAF of 0.4. Each grid was narrowed down and divided into three regions of TAF exceeding 0.4, 0.6, and 0.8. These regions are illustrated in Figure 4.4. Picking the location for the tag-along station from these
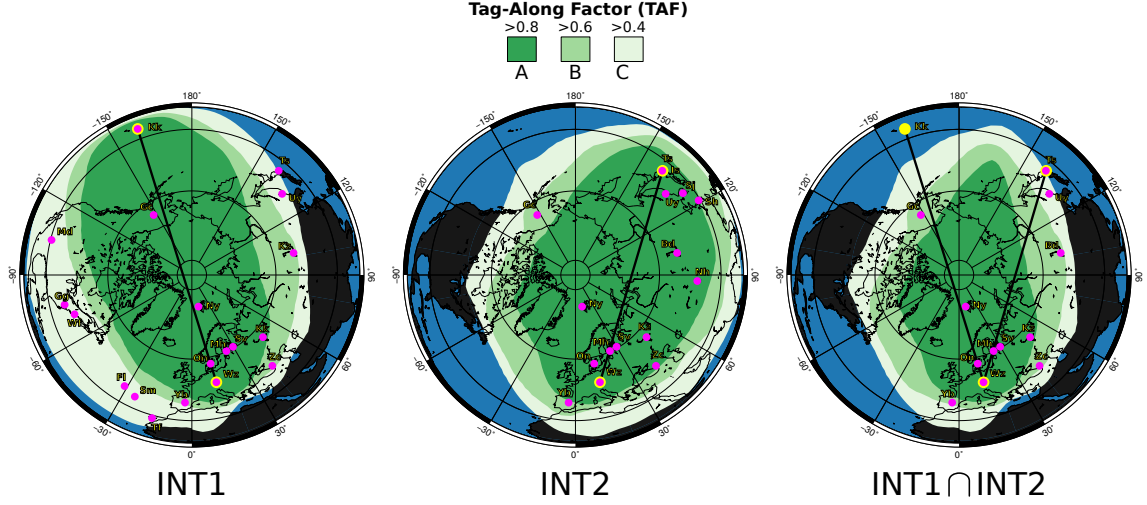
Figure 4.4: Maps of TAF values for the tag-along station in INT1 (left), INT2 (middle), and INT1∩INT2 (right) grids. The TAF levels are A (TAF>0.8), B (TAF>0.6), and C (TAF>0.4).

grids we simulated observed delays for the three stations and estimated UT1-UTC w.r.t. IERS EOP 08 C04. In 2016 the c5++ analysis software was extended with the capability to generate simulated delays (Klopotek et al., 2017). The simulated delay is given by Equation 4.1 and it includes geometric delay, troposphere delays, station clocks, and baseline-dependent Gaussian noise.

$$\tau_{sim} = \tau_{geom} + mf_w(e_2)\text{ZWD}_2 - mf_w(e_1)\text{ZWD}_1 + clk2 - clk1 + \tau_{wn}. \tag{4.1}$$

The troposphere model follows Nilsson and Haas (2010); clocks are simulated as a sum of random walk and integrated random walk. The clock stability used was 10^{-14} @ 50 min and the baseline dependent Gaussian noise was set to 1 cm for all baselines. In order to simulate the atmosphere delays the troposphere height, wind speed, and the structure constant C_n are required. The first two were set to constant 2 km and 5 m/s East and North wind speed components. Because C_n varies by location, an interpolated grid for its values was determined from C_n provided for different VLBI stations by Petrachenko et al. (2009). The sessions were analysed using the standard parametrisation of 6 unknowns for the Intensives (see Section 3.2.4.4). The UT1-UTC estimation was done as a Monte Carlo simulation with 20 iterations for each grid point, simulating a new observed delay for each iteration. A WRMS value for UT1-UTC w.r.t IERS EOP 08 C04 was computed from these 20 estimates and averaged over all the respective Intensive sessions from 2014. We simulated observations without the tag-along stations to estimate a reference UT1-UTC WRMS. The simulated reference values for INT1 and INT2 were 15.43 μs and 12.03 μs, respectively. Because the simulated values do not include errors due to instrumentation (e.g. cable delay), these values are lower than the actual UT1-UTC estimates from the Intensives, as expected. This is not an issue since we are interested in only the relative improvement achieved with the tag-along station. We define the improvement with a β-value as the ration of the mean WRMS obtained with the tag-along station to the two-station reference value, given by
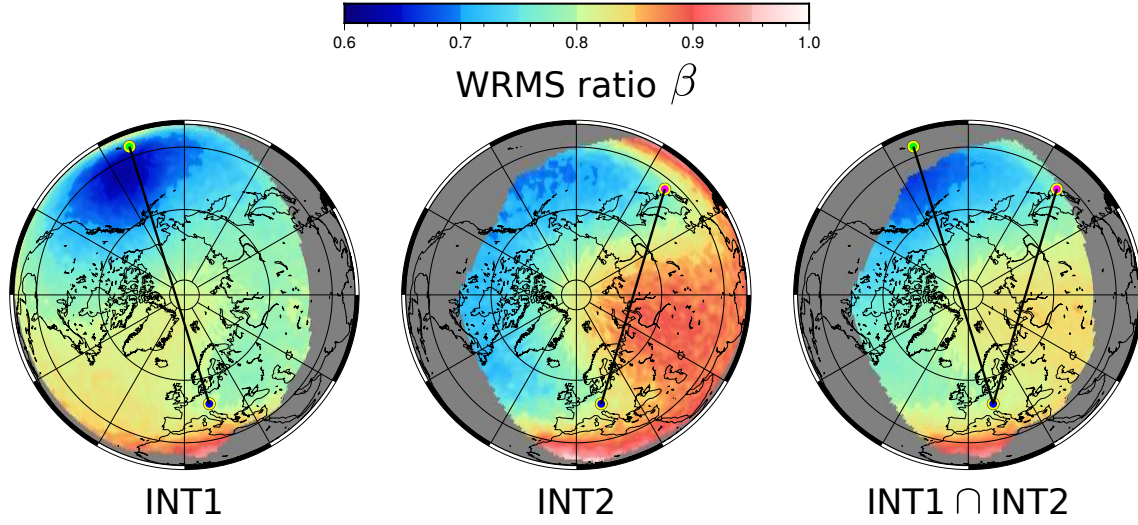
Figure 4.5: Maps of the β-values for the INT1 (left), INT2 (middle), and INT1∩INT2 (right) grids. The values represent the ratio of UT1-UTC WRMS obtained with the tag-along station and the reference solution. (Kokee: green dot, Wettzell: blue dot, Tsukuba: magenta dot)

$$\beta = \frac{WRMS_3}{WRMS_2}. \tag{4.2}$$

The β-values for the INT1∩INT2 grid were determined as the mean of the INT1 and INT2 β-values of the common grid point. The resulting UT1-UTC WRMS patterns are a convolution of geometry and the simulated troposphere as realised by the C_n value grid. The maps in Figure 4.5 show these patterns.

The β-values were in the range of 0.61–0.97. Based on these results the most suitable location for a tag-along station in INT1 sessions would be from around Kokee up to the Alaska region. For INT2 the Alaskan region is also favorable. A tag-along station located in North America could participate in both INT1 and INT2 while providing significant improvement w.r.t. these baselines. For a location that has had geodetic VLBI activity in the past Gilmore Creek could provide the largest improvement in terms of mean β-value for INT1 and INT2. To validate the performance of the simulations, we also computed a reference solution for the UT1-UTC WRMS using the INT3 network of Tsukuba, Wettzell, and Ny-Ålesund. This reference was compared to the one from the INT2 network where the tag-along station was placed at the location of Ny-Ålesund. The UT1-UTC estimates were nearly identical (within approximately 0.5 μs) even though the INT3 schedules were created specifically for that network as opposed to the INT2 schedule.

Even though the main purpose of the study is to detect optimal locations for the tag-along station, the addition of the third station is an example of flexible scheduling, where, by adding the third station in by tagging along to an existing schedule, we are able to demonstrate improvement in the UT1-UTC estimates. As the results of the simulation study show, several existing stations are already located in zones that are beneficial for adding a station in a tag-along mode to the Intensive network. In principle, individual stations could themselves create a tag-along schedule for

themselves. Naturally, this would increase the workload for the correlators in order to make available the additional baselines in the parameter estimation.

UT1-UTC is the geodetic VLBI product that has the highest need for low turnaround time. Because IVS aims with VGOS to provide an ultra-rapid UT1 product every 30 minutes with an accuracy, 7 μs, the observing network should constantly have long East-West baselines observing. As shown, improvement in Intensive performance is dependent on geometry and troposphere. There are areas in which a tag-along station can participate to a very high degree (TAF>0.8) but the improvement in UT1-UTC estimates is very modest. If the network needs to continuously provide highly accurate UT1-UTC estimate, it is possible that an Intensive-type baseline subnet could allocate some of their observing time for guaranteeing observations on long East-West baselines. These results also suggest that within a small network tagging-along versus optimising the schedule for all the stations might not necessarily degrade the solution significantly. If the VGOS network includes a set of reliable core stations, they could be joined by stations initially in a tag-along mode without the need for immediately creating a new observing schedule. On the other hand the sources could be selected based on maximal visibility to as many stations as possible. However, as seen from these simulations, not all locations are equal in terms of how much they can improve the results. One option would be to determine a strong core geometry, which would benefit the most from any additional stations. The type of analysis done here could be used for assessing the impact of tagging-along instead of schedule optimisation. It is possible that with further advances in automation and scheduling these types of tag-along scenarios could be included in the VLBI product line with relative ease.

4.4.2.1 Scheduling for twin telescopes

The upcoming VGOS network will also include twin telescopes at three sites: Onsala, Wettzell, and Ny-Ålesund. The co-located telescopes are capable of simultaneously observing in two different directions. With multidirectional observations the troposphere delays above the site can be better estimated, which will reduce the error caused by the turbulent troposphere. This will further increase the complexity of the scheduling tasks. There are several possibilities for scheduling the twin telescopes. We can, for example, consider a situation where a twin telescope is observing within a full VGOS network of single-dish sites. The twin telescopes can be scheduled to observe the same source. If the rest of the network is observing the same source, this draws the benefit of always having both telescopes forming baselines in the scan, and assuming common clocks and troposphere, reducing the delay uncertainty by $\sim \frac{1}{\sqrt{2}}$.

However, observing this way loses the benefit of multidirectional observations. Scheduling-wise this is the simplest approach as the twin telescopes can be regarded as two separate but co-located telescopes, making the network geometry optimization straightforward and achievable with existing algorithms. Another option is to schedule the twin telescopes to observe in sequence, where one telescope is always observing while the other is slewing to a new source. Considering that the slew-rates for the new VGOS antennas are considerably fast, the scan lengths need to be short enough

to avoid one telescope waiting for the rest of the network idling on-source. In order to realise the potential for troposphere error mitigation, the observations should be made to two directions simultaneously. For scheduling this complicates the task significantly. In order to form at least one baseline both telescopes from the twins need to pair with at least one other telescope from the full network. This means that the observation geometry has to be divided into at least two subnets. The number of baselines formed by N telescopes is $N(N-1)/2$. If two telescopes (including one half of a twin telescope) are separated from the main network, the total number of baselines is reduced. Finding the balance in terms of number and size of subnets w.r.t. overall observing geometry is vital for scheduling the twin telescopes efficiently. The number of possible subnets grows even larger when considering a full VGOS network of approximately 30 sites including three with a twin telescope. In addition to optimizing for overall network geometry, the scheduling algorithm also needs to consider the relative orientation of the co-located antennas.

The scheduling of twin telescopes can be conceptually divided into two parts. The first is to optimise the relative observing geometry between the two telescopes that form the twin telescope, and the second is to optimise incorporating the twin telescope within a larger global observing network. Naturally, the ultimate goal is to combine the optimisation for both local and global geometry. We have started work to determine how the local geometry should be constructed and if it is possible to represent this as a set of rules that involve both telescopes. To investigate this we use the c5++ VLBI software to generate simulated observations for a twin telescope and subsequently analyse them to estimate station positions, clocks, and atmosphere delays, including gradients, in Precise-Point-Positioning (PPP) mode (i.e. we do not simulate a baseline geometry, but delays for each telescope). The gradients are intrinsically included in the simulated troposphere due to the frozen flow model. The simulated delay (for each telescope) consists of station clock, turbulent atmosphere (ZWD) with $mf = 1/\sin(el)$ mapping function, and Gaussian noise and it is given by

$$\tau = mf(el)ZWD + CLK + wn, \tag{4.3}$$

where the ZWD is simulated following Nilsson and Haas (2010) (see also Section 4.4.2), CLK as integrated random walk + random walk with a clock stability of 10^{-14} @ 50 min, and wn is $\sim$16 ps Gaussian noise. The value of the mapping function $mf(el) = 1/\sin(el)$ depends on the elevation el of the observation. To realize an observing geometry we generate a time-tagged set of azimuth (az) and elevation (e) pairs for both telescopes (from now on referred to as OTT1 and OTT2 with corresponding subindices 1 and 2). An observation is simulated every 2.5 min for 24 h (576 observations per telescope). These 576 sets of t, az_1, el_1, az_2, el_2 are used as an input to c5++, which simulates the corresponding CLK_1, CLK_2, ZWD_1, and ZWD_2 values. Using Equation 4.3 we can thus compute an observed delay for each epoch and telescope.

The way the (az_1, el_1) and (az_2, el_2) pairs are generated form the different observing geometries we investigate. In general the approach is to point OTT1 to a random direction and then point OTT2 based on a geometric rule that depends on
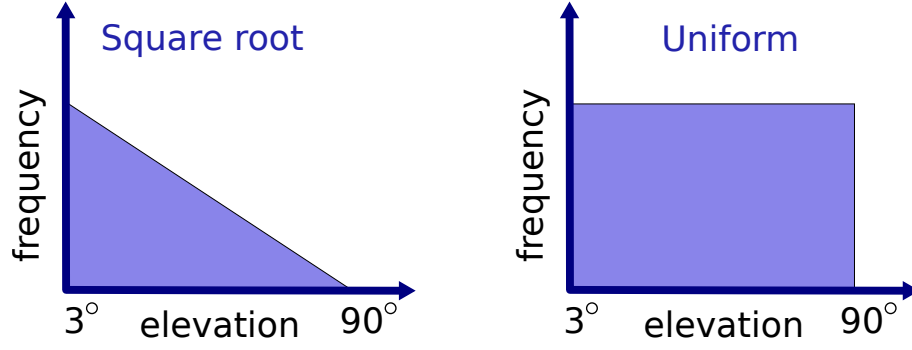
Figure 4.6: The two sampling distributions from which the pointing for OTT1 was drawn. The figures depict the frequency of occurrences w.r.t the elevation. Left image: the square root sampling distribution. Right: the uniform sampling distribution. For both cases an elevation cut-off of 3 ° was used.

OTT1 pointing. For OTT1 the (az_1, el_1) are drawn using two sampling approaches: uniform and square-root. For both approaches $az_1 \sim U(0,1)$, while the elevation el_1 follows $el_1 \sim U(0,1)$ for uniform and $el_1 \sim \sqrt{U(0,1)}$ for square-root. Finally, the az_1 are mapped to 0°–360° and el_1 to 3°–90°. In azimuth both approaches work similarly. For elevation the uniform distribution leads to equal number of high and low elevations, while the square-root approach will give more low elevations, but more equal sky-coverage, as changes in angles in high-elevations represents smaller distance on the sky. These differences are illustrated in Figure 4.6.

For pointing OTT2 we focus on four geometric cases: same source, orthogonal, opposite, and random. In the orthogonal case the telescopes are pointed so that the difference between their elevation is 90°, where the plane spanned by the source vectors is also orthogonal to the local horizon (i.e. the difference in the telescopes' azimuth angles is 180°). The case of opposite geometry is similar to this, but the elevations for the two telescopes are identical (i.e. they are pointed to the same elevation but at exactly opposite azimuth angles). The combinations of geometric cases and sampling approaches are listed in Table 4.4. Each geometry is represented by a set of (OTT1, OTT2) pairs which determine the pointing directions for the telescopes. Since the OTT1 directions are generated with the uniform and square-root approaches and there are four geometries to determine OTT2 direction for each sampling approach, we get in total eight $(sampling(2) \times geometries(4) = 8)$ distinct observing geometries. As mentioned before, the simulated delays were generated in sets of 576 observations per 24 hours, for which one set corresponds to one realization of a geometry. The simulated observations were generated in Monte Carlo fashion with 5000 iterations, thus generating this amount of realizations of each geometric case.

Using Equation 4.3 we can use the simulated values to compute two observed delays (τ_1 and τ_2) for each epoch. The observations are analysed in a least-squares adjustment to estimate station positions, clocks, and combined ZWD and gradients. The parametrisations for the two stations at an epoch are: two station offset per 24 h of observations w.r.t. *a priori* positions (E,N,U) = $(0, 0, 0)$, two station clocks as CPWL at 60 min intervals, combined ZWD as CPWL at 15 min intervals, respectively

Table 4.4: Geometric selection rules for OTT2 direction w.r.t. OTT1. For all four cases the OTT1 is randomized using uniform and square-root sampling. This results in eight distinct observing geometries.

Geometry	Pointing OTT1	Pointing OTT2
Same source	random uniform	same as OTT1
	random square-root	same as OTT1
Orthogonal	random uniform	orthogonal in *el*, opposite *az*
	random square-root	orthogonal in *el*, opposite *az*
Opposite	random uniform	same *el*, opposite *az*
	random square-root	same *el*, opposite *az*
Random	random uniform	random direction using same sampling
	random square-root	random direction using same sampling

combined East and North gradients as CPWL at 3 h intervals. Because we have access to the simulated values, and the station positions are known exactly to be $(E, N, U) = (0, 0, 0)$, it is possible to directly compare the estimated and 'true' values as RMS differences. This comparison is done for the station position and ZWD. The estimated gradients can not be compared directly, since they are not simulated but come implicitly from the turbulence model, and thus only estimated values are available. For each 24-hour period we get one E, N, and U estimate for both stations. This is in total 6 estimated coordinates for the 5000 geometry realizations, for which one *true − estimated* RMS value for each coordinate is computed. For ZWD there are 97 CPWL estimates in the 24 h. The ZWD CPWL are interpolated to the epochs of the simulated observations, and RMS is computed for each 24-hour period. The resulting 5000 RMS values are averaged to get a mean RMS for the *true − estimated* ZWD.

The results from these preliminary studies indicate that in terms of station positions w.r.t. 'true' RMS values the orthogonal strategy has the best performance for station positions. However, the margin compared to opposite azimuth strategy is very narrow. In comparison, opposite azimuth gives the best compromise in terms of station positions and ZWD estimates. The comparison of the results are depicted in Figure 4.7. The relatively good performance of random strategy w.r.t. the two geometric can be explained by the fact that the elevation distribution has an important role for the estimation. With randomizing one or both observing directions we effectively assume that a source is always found in that direction. This is especially evident in the RMS for the ZWD estimates from the square root sampling approach. In a real scheduling situation the source distribution is more sparse and it is not guaranteed that suitable sources will always be found at given elevations. Geometric rules, such as the orthogonal or opposite azimuth strategies, provide more strict and realizable conditions for the directions of potential sources. For station positions the orthogonal strategy outperforms random pointing for OTT1 and OTT2 for both sampling approaches.
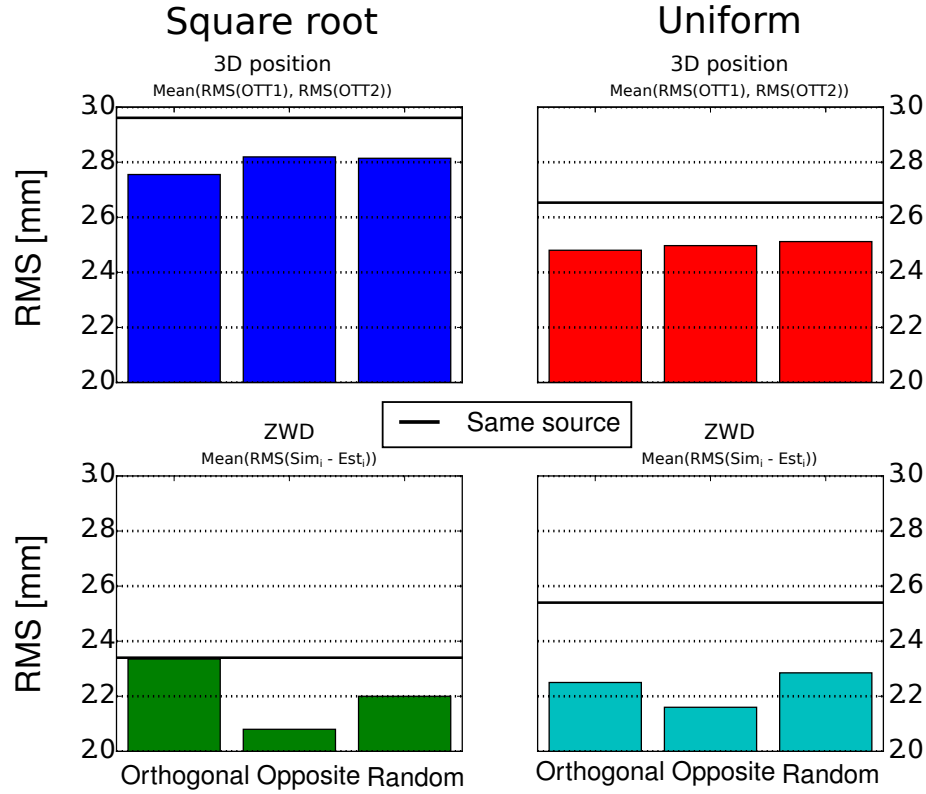
Figure 4.7: RMS of the residual values in millimetres for the station positions and ZWD estimated from simulated observations for OTT1 and OTT2. The values were calculated for each strategy-distribution pair. The RMS for the stations positions was calculated for each coordinate (E,N,U) from all 5000 iterations for both stations and then averaged to one 3D position RMS value. The RMS for the ZWD was computed as the difference of *simulated − estimated* ZWD values for each strategy realisation (i.e. iteration). The RMS values for each iteration were then averaged to give a single RMS. The black line denotes the RMS obtained by observing the same source with OTT1 and OTT2.

For ZWD determination low elevation observations seem to have more importance; the best results in terms of ZWD are achieved with opposite strategy and observing mainly on low elevations (i.e. elevations for OTT1 (and following opposite strategy also OTT2) are sampled with square-root approach). For orthogonal strategy low elevations at OTT1 implicitly mean high elevations at OTT2. This leads to somewhat weaker performance for ZWD estimation if one telescope mainly observes low elevations using orthogonal strategy. However, with better ZWD determination with low elevation observations, there is a trade-off in terms of station positions, and especially the U-coordinate. High elevation observations are necessary for the observing geometry to be sensitive to station height. The orthogonal strategy leads to the best station position estimates even in the cases where its ZWD performance is weaker. Observing the same source simultaneously performs worse for station positions and ZWD for all combinations of geometry and sampling approaches. This leads us to conclude that locally multidirectional observations produce the best results. However, the questions remain how the multidirectional strategies will perform within full VGOS netowrk, and what will be the effect of necessary

subnetting. Geographically the three twin telescope sites will be located at nearly the same longitude. They are situated in a way that could see them acting as important links between an eastern and western subnets. Combining optimization for local and global geometry, including finding the best subnet division, will be a difficult task. Furthermore, for VGOS any scheduling approach needs to be automated and dynamic. This is in favour of defining easy-to-implement geometric rules as a starting point for twin telescope scheduling.

4.4.3   Recording and correlation with VGOS data-rates

A crucial step outlined in the *Strategic Plan of the IVS for the Period 2016– 2025* (Nothnagel et al., 2016) for realizing continuous VGOS operations in the future is attaining the capability to handle the large amounts of observed data. The estimated amount of data recorded in a session for a VGOS antenna is on the order of 40 TB. This poses big challenges for recording, data transfer, and correlation. From the recording systems discussed in Section 3.2.2 the Mark6 system is designed to be able the handle the VGOS data rates. The more hardware-flexible FlexBuff system has also in tests reached VGOS level data rates (Simon Casey, personal communication, February 9th, 2018). However, the position of the IVS is to not limit stations to a single solution in order not to discourage technical advancements in the area. On the other hand, it is necessary to maintain a certain degree of standardization in order to reach consistent data quality. Currently, the VLBI stations transfer the data to the correlator either by shipping the disk modules physically or via e-transfer. Currently e-transfer is used by most of the stations as the means to deliver the data to the correlators. The advantage of shipping physical modules is that it reduces the need for data storage space at the correlator. Naturally, this approach will not reach the same latency as e-transfer. The success of e-transfer depends on the capability of the infrastructure to deliver the data from the individual stations to the correlators. This will be limited by both the network bandwidth at the stations and even more so at the correlators, which need to receive the data from all the stations. Furthermore, even in the case of high-speed transfer capabilities, this puts a strain on the storage requirements at the correlator. Two envisioned approaches to solve this are to a) make it possible for the correlators to retrieve the data in a pace that will balance the load of incoming data, or b) move from centralized correlators to distributed correlation. This could be achieved for instance by using commercial cloud architecture, since there have been significant advances in recent years in its availability, cost-effectiveness, and performance.

The correlation process is usually the first stage where the quality of the recorded data can be assessed. If at this stage the observed data have shortcomings with respect to the session setup, the data salvage process can turn out to be very labour intensive. Furthermore, the fringe-fitting process is regarded as requiring a high-level of expertise from the correlator staff. In order to guarantee a continuous product chain it is crucial that there are several correlators in operation with good resources in order to share the pressure that operational VGOS will put on them. It is foreseeable that among other segments of VGOS operations, correlation will also

benefit of automation of the operations in any stage where it is feasible. Naturally any automated process needs to be robust enough to guarantee a high-level of end results. Nonetheless, it has the potential to both reduce the turnaround time of the results and reduce the cost of the operations. These benefits are common to all stages of the VLBI product chain.

A promising demonstration of cloud correlation was achieved in New Zealand (Weston et al., 2017). The initial assessment of the feasibility of cloud correlation was done together by Auckland University of Technology (AUT) and Research and Education of Advanced Network New Zealand (REANNZ). Later, the project included the Commercial Cloud service provided by Catalyst IT Ltd. The key point in the study was to assess whether correlation can be performed successfully in a more cost effective manner by employing a commercial alternative to housing all the hardware and network infrastructure at the VLBI sites and dedicated correlators. The widely used software correlator DiFX (Deller et al., 2007) was implemented to operate within the cloud architecture. From the results of the study it was found that it is possible to achieve real-time correlation and manage resource scaling using DiFX and Ansible[1], respectively. This demonstration showed that cloud correlation has the potential to be a viable option to manage the issues posed by VGOS operations.

4.4.4   Data analysis for VGOS

The aim of VGOS to provide continuous monitoring of geodetic parameters will also pose challenges in the data analysis segment. The shift from strictly session-based VLBI experiments to the need to produce geodetic products at different intervals and latencies will require new approaches to how the sessions are analysed operationally. Whereas a typical legacy 24-hour session (e.g. IVS-R1), depending on the network size at the time, contains on the order of 1000–10000 observations, a similar time-span observed with VGOS will contain nearly two orders of magnitude more observations. For the legacy 24-hour sessions it is feasible for an analyst to manually process the data in order to produce a database which is corrected for clock breaks, ionosphere, outliers, and where the auxiliary data sets (cable, weather) have been screened for abnormalities. For VGOS, the near continuous stream of data and the need for timeliness prevent the use of this type of approach. This means the data analysis process needs to be automated to such a degree that geodetic parameters can be produced with sufficient quality without human interaction. This is especially true for the Ultra-rapid and Rapid products, which would require a 24/7 staff to process such observations. Such processing has two main requirements: that all the necessary auxiliary and *a priori* data are available, and that the analysis software packages used can perform basic analysis in automated mode. The need for sufficiently accurate *a priori* EOP data is especially important for providing good UT1-UTC estimates. An example case for the impact of *a priori* information to UT1-UTC for Intensive-type session is demonstrated in Paper II. This leads to a trade-off of waiting for good *a priori* data and the timeliness requirements of the geodetic products. Furthermore, moving from session-based analysis to a continuous mode

---

[1]`https://www.ansible.com`

will require updates to the existing VLBI analysis software, which have traditionally used least-squares adjustment based on the full information available from the session. An alternative analysis method is to use sequential-filter-based approaches. A widely used filter in many geodetic applications is the Kalman filter (Kalman, 1960). In recent years some VLBI software, e.g. VieVS, have been modified to include this as an analysis option. The use of Kalman filter for analysis of geodetic VLBI data has been demonstrated by, e.g., Nilsson et al. (2015), Soja et al. (2015), and Karbon et al. (2017). These results show that Kalman filtering is very suitable for analysing the observations in sequential mode even in the presence of clock breaks. On the other hand, in order to combine results from multiple analysis centres the access to normal equations is still necessary (Nothnagel et al., 2016). Furthermore, the robustness of any automated process needs the be thoroughly validated. Comparing the results from sequentially filtered analysis to ones from a standard least-squares adjustment provides a way to assess the performance of the (near) real-time analysis. Nonetheless, the capability for automated analysis in order to realise the timeliness goals of VGOS is of undeniable importance.

Chapter 5

Summary of appended papers

This thesis has focused on different aspects on both identifying ways to improve the results from the existing legacy VLBI and to prepare for the eventual VGOS era. The transition to VGOS observations involves all parts of the VLBI product chain from observations to final products. Paper I deals with in ensuring that the necessary equipment upgrades for the back-end of the signal chain in Onsala do not degrade the performance in terms of the final product, that is the estimated geodetic parameters. In most cases the equipment upgrades are done sequentially and used with the legacy system for operational VLBI. It is important to verify that the quality of the geodetic products do not degrade in this transitional period. There has been an ongoing effort to improve the quality of the operational IVS Intensive sessions. Historically, these sessions have not performed in line with the expected accuracy that is indicated by the formal errors from the scheduling process. Papers II, III, and IV deal with finding ways to improve the IVS Intensive sessions by using methods such as automated analysis and flexible scheduling, which are relevant in preparation for the upcoming VGOS operations. In Paper II IVS-INT1 sessions on the Kokee–Wettzell baseline from 2001 to 2015 for which the correlator output databases (i.e. includes ambiguities and ionosphere) were available are analysed consistently with c5++ VLBI analysis software in automated mode. Using different analysis options the aim was to identify which choices are most crucial for the UT1-UTC accuracy. In Paper III the c5++ VLBI analysis software was implemented with a robust estimation based on the L1-norm (as opposed the standard least-squares). Using the same set of IVS-INT1 sessions as in Paper II, the performance of the L1-estimation for ambiguity estimation was assessed. In Paper IV the question is whether, as an alternative to pure analysis methods, it is possible to improve the Intensives by adding a third station to the standard two station network and what would be the optimal location for such a station. This is done with extensive Monte Carlo simulations by simulating a third station in tag-along mode, taking into account not only geometry effects but also a turbulent troposphere. In the following, a brief introduction and summary are given for the four appended papers and their results.

5.1 Summary of Paper I

In 2011 the Onsala Space Observatory acquired and installed a Digital Base-Band Converter (DBBC) (Tuccari, 2004), model DBBC2 (Tuccari et al., 2010), with the purpose of replacing the old VLBI Mark4 analogue back-end. The Mark4 rack had been used operationally for over 15 years for both geodetic and astronomy purposes. Between 2011 and 2014 the back-end/recorder combination Mark4/Mark5A was phased out and replaced operationally by a DBBC2/Mark5B+. During this period both systems were run in parallel both to gain experience with operating the DBBC and to continually carry out the operational VLBI observations of the Onsala network station. We wanted to investigate whether there exist any systematic differences between the two systems. The sessions types observed in parallel include R1, R&D, EUR, T2, and the CONT14 campaign. Both parallelly observed sessions (On for analogue and Od for digital) were correlated at the Bonn correlator (Bernhart et al., 2015). During the observations log-files were also created for both On and Od, from which the weather and cable calibration data for both were extracted. The On and Od group delays and auxiliary data were then compared. Firstly, the group delays for On and Od were compared directly from the raw correlator output. This was done by computing the difference for the observed delays on On-Od zero-baseline and the triangle misclosure of On, Od, and a third station (Wettzell). The median baseline misclosure of the On-Od-Wz triangle for R1 sessions was found to be 6.5 ps and for CONT14 3.2 ps. The larger number of observations reduces the triangle misclosure for CONT14. The sessions were also analysed using calc/Solve (Ma et al., 1990) and νSolve (Bolotin et al., 2014) VLBI analysis software (see Section 3.2.4). This was done by including either On or Od in the analysis while turning the other station off during the analysis. From this we obtained sets of geodetic parameters, EOP, station coordinates, and ZWD, for On and Od, respectively. The differences were found to be within their formal errors, excluding the Up-coordinate for two R1 sessions. This is likely due to data gaps and the outlier detection algorithm of the analysis software handling these results differently. Lastly, the cable delay measurements from the On and Od log-files were compared. The cable delay differences were found to be smaller than the formal errors for the group delays from the correlator. A typical group delay formal error from the correlator for a standard geodetic VLBI sessions with a minimum signal-to-noise ratio (SNR) of 25 and an effective bandwidth of 360 MHz is approximately 15 ps (Takahashi et al., 2000). From the results we can conclude that there are no significant differences between the results obtained with the DBBC/Mark5B+ and Mark4/Mark5A. No systematic differences were found either in the observed group delays, estimated geodetic parameters, or the auxiliary data.

5.2 Summary of Paper II

The main purpose of the IVS Intensive sessions is to provide the users (e.g. GNSS) with daily UT1-UTC estimates with minimal latency. The UT1-UTC updates are essential for GNSS as these techniques cannot directly determine the phase of Earth's rotation from their observations. The degree to which the turnaround time for geodetic results can be minimised is dependent on the amount of time it takes to correlate and analyse a VLBI session. Starting from the correlator output (so called Version-1 databases) we investigate in terms of UT1-UTC WRMS w.r.t. IERS EOP 08 C04 (from here on UT1-UTC WRMS refers to the accuracy w.r.t IERS EOP 08 C04). We investigated the impact of different analysis strategies and application of available external information to the UT1-UTC w.r.t. IERS EOP 08 C04 from a fully automated analysis of IVS-INT1 sessions. The IVS Intensive 1 (IVS-INT1) sessions on the Kokee–Wettzell baseline are carried out on a daily basis from Monday to Friday at 18:30 UTC. For the analysis we used in total 1669 IVS-INT1 Version-1 databases between 2001.0–2015.0. The number of sessions were based on the necessary databases and auxiliary data, The Version-1 databases contain the group delays as they come from the correlator. This includes group delay ambiguities and the contribution of the ionosphere. Before UT1-UTC estimation these effects need to be removed from the data. The whole analysis was carried out using c5++ VLBI analysis software (see Section 3.2.4.2) in fully automated mode. The software is capable of ambiguity estimation and ionosphere calibration and thus we could perform the full analysis chain consistently within one software. In a typical parameter estimation setup for an Intensive session with two stations the estimated parameters are one station clock (the other is set as reference clock), ZWDs offsets for both stations, and UT1-UTC offset. Station positions, radio sources, polar motion, and nutation/precession are fixed to their *a priori* values. In this setup the total number of estimated parameters is six. This standard parametrisation was also used in our study with the exception of, in one case, estimating a constrained station position for the non-reference station. Using different analysis setups we investigated whether it is necessary to use the local meteorological and cable delay data from the station log-files, what is the impact of using VMF1 or GMF(GPT2) as the mapping function, how the UT1-UTC accuracy is affected by the *a priori* EOP, and can we draw benefit in terms of UT1-UTC accuracy from estimating one station position. These strategies were assessed based on the UT1-UTC WRMS from the 1669 analysed sessions. Crude outliers (e.g. as a result of failed ambiguity estimation) were removed by imposing relatively loose rejection conditions of 1000 μs and 50 μs for the absolute values of the UT1-UTC residuals and formal errors, respectively. The resulting difference due to the choice of mapping functions were approximately 10 ns. Including the information from the station log-files improved the WRMS by $\sim$0.4 μs. The UT1-UTC WRMS values with and without station log-files (as the impact of mapping function choice was minimal) were $\sim$17.6 μs and $\sim$18.0 μs. The use of station log-files is recommended, provided that the log data are reliable. Because the analysis is fully automated, any undetected deficiencies in the log files propagate to the estimated parameters. The impact of this was evident during a period between

late 2013 and early 2014 in which the Wettzell station log-files contained anomalous cable readings. This caused the UT1-UTC residuals to shift by approximately 5 μs compared to the solutions without the cable delay data. The key factor for accurate UT1-UTC estimates access to recent *a priori* polar motion information. Based on extensive Monte Carlo simulations the UT1-UTC accuracy degrades $\sim$4 μs within one day from the initial epoch of *a priori* polar motion values. If using one week old *a priori* values, the WRMS has degraded to $\sim$50 μs. In case of *a priori* UT1-UTC this does not pose a similar problem. Because UT1-UTC is estimated during the analysis, small changes in the *a priori* will still converge to the same (within error margins) estimate. This requires that the difference between the linearised functional model approximates the 'true' value well enough. Estimating one station position in addition to the six regular parameters did not lead to improvement in the UT1-UTC WRMS. If the station motion was constrained below 1 mm the UT1-UTC WRMS was unaffected. Based on these results drastic improvements in UT1-UTC are difficult to obtain. The best way to ensure the highest accuracy is to design the automated VLBI analysis process in such a way that access to the most recent *a priori* polar motion values are available at the time of processing.

5.3   Summary of Paper III

Automating the analysis chain is an essential step for providing timely near-real time geodetic parameters from VLBI observations. This is particularly important for VLBI products such as the daily UT1-UTC estimates from the IVS Intensive series. The data input for the analysis process is provided in databases (see Section 3.2.4.1) produced by the correlator. The data provided in the databases are group delays. In dual-frequency S/X VLBI observations each band is divided into several channels. The group delays can be determined with BWS from the best-fit slope of the phases for the channels (in each band) in frequency-phase domain (see Section 3.2.4.3). The BWS technique can determine the group delays up to an unknown number of fixed ambiguity spacings. For a typical IVS Intensive session the ambiguity spacing is 200 ns and 50 ns for S- and X-band, respectively. In addition to the ambiguities the group delays also contain the delay contributions from the ionosphere. Before geodetic parameters are estimated from the data both the delays due to ambiguities and to the ionosphere need to be estimated and removed. The c5++ VLBI analysis software (see Section 3.2.4.2) can do both of these tasks in a fully automated mode. In the standard c5++ version the ambiguity estimation is done using iterative least-squares (L2-norm) adjustment. After each iteration any observation for which the residual exceeds half of the ambiguity spacing for that given frequency band is shifted by the amount of the ambiguity spacing. This process is iterated until the ratio of the post-fit residual WRMS reaches a cut-off condition. L2-norm is a Maximum-Likelihood Estimator if the observation errors are assumed to be Gaussian. For observation noise this approximation is generally valid. The group delay ambiguities however are quantized shifts, which are from the analysis perspective distributed randomly among the observations in a session. Their magnitude is also considerably larger than the normal deviation of the observations. Because the ambiguities do not come from a Gaussian distribution the L2-norm adjustment underperforms in some situations. Since the L2-norm minimises the squared residuals the observations with ambiguities have a disproportionate influence on the fit. This leads to the ambiguities not being detected, deteriorating the model fit, and subsequently propagating to the target parameters. As opposed to L2-norm, the L1-norm minimises the absolute value of the residuals. This adjustment method is more robust against outliers, such as the group delay ambiguities. The benefit of L2-norm is that it is differentiable everywhere, which makes minimizing the objective function straightforward. The implementation of the L2-norm is easy because the parameters can be estimated by simply inverting the normal equations. In the case of L1-norm the residuals have to be expressed using slack variables. Essentially they separate the design matrix and the residuals into negative and positive parts. This way it is possible to deal with the non-differentiable point at zero due to taking the absolute value of the residuals. The resulting matrix equation reduces to a linear programming problem. To improve the automated ambiguity estimation and by that the UT1-UTC estimation we implemented the L1-norm based adjustment method in c5++. The implementation was done as an external Python application, which could be invoked directly from c5++. In order to test the robust ambiguity estimation we analysed 1835 IVS INT1 sessions

between 2001 and 2015, starting from the databases generated by the correlator. The analysis was done in two stages. In the first stage we estimated the ambiguities and ionosphere for all the sessions using both L1- and L2-norm adjustment with three different weighting strategies (unit weighting, correlator formal errors, correlator formal errors multiplied by mapping function). In the second stage the ambiguity and ionosphere free databases were analysed using L2-norm to produce the UT1-UTC estimates. The L2-norm was chosen for the parameter estimation because at this stage the errors are expected to be more nearly Gaussian. We used several metrics to determine whether the ambiguity estimation was successful in a given session. The most direct approach is to inspect the post-fit residuals after the first stage. The inspection showed that the L1-norm analysis resulted in smaller post-fit residuals while the L2-norm had an increased number of sessions with post-fit residuals close to 50 % of the ambiguity spacing at X-band. We also applied a rejection rule for the UT1-UTC estimates where the ambiguity estimation of the session was deemed a failure if the UT1-UTC residuals or formal errors exceeded 1000 μs or 50 μs in absolute value, respectively. The L1-norm increased the number of successful sessions for all weighting strategies. The best performance was achieved with unit weighting, where the L1-norm adjustment was able to successfully process 85 sessions that failed with L2-norm. In this case the L2-norm performed better for only one session. Relative to all successfully estimated sessions the L1-norm provided a 5 % increase in success rate (e.g. for unit weighting 1564 were successful for both adjustments methods, 85 for only L1-norm, one for only L2-norm). The computational cost of using a more complicated estimation method did not cause significant overhead. Most of the sessions converged in a similar number of iterations for both estimation strategies.

5.4 Summary of Paper IV

Since the start of the IVS Intensive series there have been many efforts to improve the accuracy of the UT1-UTC estimated from these sessions. These include scheduling-based approaches (Leek et al., 2015; Gipson and Baver, 2016; Uunila et al., 2012) and increasing the session length (Artz et al., 2012). Currently the IVS Intensive consist of three session types: IVS-INT1 (one baseline), IVS-INT2 (one baseline), and IVS-INT3 (three baselines) (see Section 4.1.2.2). Sometimes these sessions are joined by additional stations, but generally the network composition is fixed. Focusing on IVS-INT1 and IVS-INT2 sessions scheduled for the year 2014 we investigated the impact of expanding these single-baseline Intensive sessions by adding a third station in a tag-along mode. The accuracy criterion is the WRMS of the UT1-UTC estimates w.r.t. IERS EOP 08 C04. This included in total 230 IVS-INT1 and 102 IVS-INT2 sessions. The study was divided into two stages. The first stage consisted of pre-determining location grids for the third station that share mutual source visibility with the original network. In the second stage we simulated observed group delays for the two original stations in IVS-INT1 and IVS-INT2 sessions and the third station in the tagged-along scans at each of the pre-determined grid points. The simulated group delays were generated (see Section 4.4.2) and analysed using the c5++ VLBI analysis software (see Section 3.2.4.2). By adding the third station in a tag-along mode we effectively demonstrate a situation where an observing network is flexibly joined by an additional station. Because of this the observing schedule is not necessarily optimised for three stations. On the other hand the flexible schedules for VGOS network need to be designed in a robust manner to handle situations where the stations need to be able to join/leave the 24/7 observations without degrading the overall performance drastically. In this sense the situation where an additional stations participates on best-effort basis is relevant for flexible scheduling approaches. For this study it was assumed that the tag-along station will have sufficient slewing capabilities and SEFD to track the source on time and to reach high enough SNR. The tag-along station locations were determined in $2° \times 2°$ resolution on a rectangular grid, starting with points covering the whole globe. These grids were then subsequently narrowed down to only include points where the third station could observe the originally scheduled sources. This results in two grids, one for common visibility for INT1 and one for INT2 schedules. To quantify the level of participation for the third station the grids were divided into three categories based on a measure called Tag-Along Factor (TAF). The categories included all points where the third station could participate in at least 40 %, 60 %, and 80 % of the scheduled scans, corresponding to TAF of 0.4, 0.6, and 0.8, respectively. The final grids were used as the basis for the second stage. In order to simulate the ZWDs in an arbitrary location on the grid global refractive index structure constants C_n were interpolated from values determined for a set of existing VLBI stations. A set of observations were simulated for each schedule. Observations were generated for every point in both grids (INT1 and INT2) for the two original stations and the tag-along station located at that specific grid point. These observations were then analysed to estimate the UT1-UTC. The observations were simulated 20 times for each tag-along

station grid point. Finally, the WRMS results were averaged over the whole year. Given the yearly averaging the number of Monte Carlo iterations was determined to be sufficient to give a representative estimate of the UT1-UTC performance for each grid point. This also helped to keep the computational cost manageable, while still resulting in 27 and 11 million simulated observations for the IVS-INT1 and IVS-INT2 cases, respectively. Because the simulated observations do not include all the possible errors sources or correlations, the results were assessed w.r.t. reference solutions. The reference values were determined by analysing observations simulated using only the original two-station networks (again for each session and averaged over the year 2014). This provided the baseline performance of the network in the context of the simulations. The improvement was expressed as the ratio of the WRMS for three stations and the corresponding WRMS for two stations ($\beta = \text{WRMS}_3/\text{WRMS}_2$). The pattern of UT1-UTC WRMS values was found to be a convolution of network geometry and troposphere. The most advantageous area for the third station in terms of β was found to be in Northern America. The minimum β-values, corresponding to the largest improvement, for the IVS-INT1 and IVS-INT2 grids were 0.61 and 0.67, respectively. To validate the performance of the simulator and to assess the impact of non-optimised schedules we used the schedules for the IVS-INT3 sessions. These sessions extend the Tsukuba–Wettzell baseline IVS-INT2 with the Ny-Ålesund VLBI station. First, we computed a reference value for the IVS-INT3 schedules in similar manner as with the IVS-INT1 and IVS-INT2. This reference value was then compared to an IVS-INT2 schedule with the third station at Ny-Ålesund's location, interpolated from the grid points. These values were nearly identical, indicating that the simulator performs consistently and in this case the schedules optimised for three stations stations ended up with a geometry similar to those optimised for two stations and including a tag-along station. From the results we can conclude that including a third station always improves the UT1-UTC estimates. This is expected as the number of observations is increased from one to three for each scan where the third station is included. However, the increased number of observations alone is not enough to result in major improvements. The location of the third station and the combination of resulting geometry and average tropospheric turbulence determine how significant this improvement is. From the perspective of dynamic scheduling schedules could be constructed around a set of core stations, which could then be flexibly joined by an additional station, when available, without necessarily re-optimising the schedule immediately.

Bibliography

Altamimi, Z., Rebischung, P., Métivier, L., and Collilieux, X. (2016). "ITRF2014: A new release of the International Terrestrial Reference Frame modeling nonlinear station motions". *Journal of Geophysical Research: Solid Earth* 121(8), 6109–6131. DOI: `10.1002/2016JB013098`.

Artz, T., Leek, J., Nothnagel, A., and Schumacher, M. (2012). "VLBI Intensive Sessions Revisited". In: *IVS 2012 General Meeting Proceedings "Launching the Next-Generation IVS Network"*. Ed. by D. Behrend and K. D. Baver. NASA/CP-2012-217504, pp. 86–90.

Bach, U. and Kraus, A. (2015). "Effelsberg Radio Observatory 2014 Annual Report". In: *International VLBI Service for Geodesy and Astrometry 2014 Annual Report*. Ed. by K. D. Baver, D. Behrend, and K. L. Armstrong. NASA/TP-2015-217532, pp. 50–52.

Baver, K. D., Behrend, D., and Armstrong, K. L., eds. (2013). *International VLBI Service for Geodesy and Astrometry 2012 Annual Report*. NASA/TP-2013-217511.

Baver, K. D., Behrend, D., and Armstrong, K. L., eds. (2014). *International VLBI Service for Geodesy and Astrometry 2013 Annual Report*. NASA/TP-2014-217522.

Baver, K. D., Behrend, D., and Armstrong, K. L., eds. (2015). *International VLBI Service for Geodesy and Astrometry 2014 Annual Report*. NASA/TP-2015-217532.

Bernhart, S., Alef, W., Bertarini, A., Bruni, G., La Porta, L., Müskens, A., Rottmann, H., Roy, A., and Tuccari, G. (2015). "The Bonn Astro/Geo Correlator". In: *International VLBI Service for Geodesy and Astrometry 2014 Annual Report*. Ed. by K. D. Baver, D. Behrend, and K. L. Armstrong. NASA/TP-2015-217532, pp. 161–163.

Bindoff, N. L., Willebrand, J., Artale, V., Cazenave, A., Gregory, J., Gulev, S., Hawana, K., Le Quéré, C., Levitus, S., Nojiri, Y., Shum, C. K., Talley, L. D., and Unnikrishnan, A. (2007). "Observations: oceanic climate change and sea level". In: *Climate Change 2007: The Physical Science Basis. Contribution of Working Group I to the Fourth Assessment Report of the Intergovernmental Panel on Climate Change*. Ed. by S. Solomon, D. Qin, M. Manning, Z. Chen, M. Marquis, K. B. Averyt, M. Tignor, and H. L. Miller. Cambridge, United Kingdom and New York, NY, USA: Cambridge University Press, pp. 385–432.

Böhm, J., Böhm, S., Nilsson, T., Pany, A., Plank, L., Spicakova, H., Teke, K., and Schuh, H. (2012). "The New vienna VLBI Software VieVS". In: *Geodesy for Planet Earth*. Ed. by S. Kenyon, M. C. Pacino, and U. Marti. Berlin, Heidelberg: Springer Berlin Heidelberg, pp. 1007–1011. ISBN: 978-3-642-20338-1.

Böhm, J., Werl, B., and Schuh, H. (2006a). "Troposphere mapping functions for GPS and very long baseline interferometry from European Centre for Medium-Range Weather Forecasts operational analysis data". *Journal of Geophysical Research* 111, B02406. DOI: doi:10.1029/2005JB003629.

Böhm, J., Niell, A. E., Tregoning, P., and Schuh, H. (2006b). "Global Mapping Function (GMF): A new empirical mapping function based on numerical weather model data". *Geophysical Research Letters* 33(7), L07304. DOI: 10.1029/2005GL025546.

Böhm, J. and Schuh, H. (2004). "Vienna mapping functions in VLBI analyses". *Geophysical Research Letters* 31(1), L01603. DOI: 10.1029/2003GL018984.

Bolotin, S., Baver, K. D., Gipson, J., Gordon, D., and MacMillan, D. (2014). "The VLBI Data Analysis Software νSolve: Development Progress and Plans for the Future". In: *IVS 2014 General Meeting Proceedings "VGOS: The New VLBI Network"*. Ed. by K. D. Baver, D. Behrend, and K. L. Armstrong. Beijing: Science Press, pp. 253–257. ISBN: 978-7-03-042974-2.

Capitaine, N., Guinot, B., and McCarthy, D. D. (2000). "Definition of the celestial ephemeris origin and of UT1 in the international celestial reference frame". *Astronomy & Astrophysics* 355, 398–405.

Capitaine, N. and Soffel, M. (2015). "On the definition and use of the ecliptic in modern astronomy". In: *Journées 2014 "Systèmes de référence spatio-temporels"*. Ed. by Z. Malkin and N. Capitaine, pp. 61–64.

Capitaine, N. and Wallace, P. T. (2006). "High precision methods for locating the celestial intermediate pole and origin". *Astronomy & Astrophysics* 450(2), 855–872. DOI: 10.1051/0004-6361:20054550.

Chao, B. F., Dong, D. N., Liu, H. S., and Herring, T. A. (1991). "Libration in the Earth's rotation". *Geophysical research letters* 18(11), 2007–2010. DOI: 10.1029/91GL02491.

Cook, J., Nuccitelli, D., Green, S. A., Richardson, M., Winkler, B., Painting, R., Way, R., Jacobs, P., and Skuce, A. (2013). "Quantifying the consensus on anthropogenic global warming in the scientific literature". *Environmental Research Letters* 8(2), 024024. DOI: 10.1088/1748-9326/8/2/024024.

Davis, J. L., Herring, T. A., Shapiro, I. I., Rogers, A. E. E., and Elgered, G. (1985). "Geodesy by radio interferometry: Effects of atmospheric modeling errors on estimates of baseline length". *Radio Science* 20(6), 1593–1607. DOI: 10.1029/RS020i006p01593.

Deller, A., Tingay, S., Bailes, M., and West, C. (2007). "DiFX: A Software Correlator for Very Long Baseline Interferometry Using Multiprocessor Computing Environments". *Publications of the Astronomical Society of the Pacific* 119(853), 318–336.

Desai, S. D. (2002). "Observing the pole tide with satellite altimetry". *Journal of Geophysical Research: Oceans* 107(C11), 3186. DOI: 10.1029/2001JC001224.

Elgered, G., Haas, R., Conway, J., Helldner, L., Hobiger, T., Pantaleev, M., and Wennebäck, L. (2017). "The Onsala Twin Telescopes: the Status at the Time for the Inauguration". In: *Proceedings of the 23rd European VLBI Group for Geodesy and Astrometry Working Meeting*. Ed. by R. Haas and G. Elgered, pp. 136–139.

Fey, A. L. and Charlot, P. (2000). "VLBA Observations of Radio Reference Frame Sources. III. Astrometric Suitability of an Additional 225 Sources". *The Astrophysical Journal Supplement Series* 128(1), 17–83.

Fey, A. L., Gordon, D., and Jacobs, C. S., eds. (2009). *The Second Realization of the International Celestial Reference Frame by Very Long Baseline Interferometry, Presented on behalf of the IERS / IVS Working Group.* IERS Technical Note 35. Frankfurt am Main: Verlag des Bundesamts für Kartographie und Geodäsie.

Fricke, W., Schwan, H., Lederle, T., Bastian, U., Bien, R., Burkhardt, G., Du Mont, B., Hering, R., Jährling, R., Jahreiß, H., Röser, S., Schwerdtfeger, H.-M., and G. Walter, H. (1988). "Fifth fundamental catalogue (FK5). Part 1: The basic fundamental stars". *Veröeffentlichungen des Astronomischen Rechen-Instituts Heidelberg* 32, 1–106.

Gipson, J. (2010). "An introduction to Sked". In: *IVS 2010 General Meeting Proceedings "VLBI2010: From Vision to Reality".* Ed. by D. Behrend and K. D. Baver. NASA/CP-2010-215864, pp. 77–84.

Gipson, J. (2012a). "'IVS Working Group 4: VLBI Data Structures'". In: *IVS 2012 General Meeting Proceedings "Launching the Next-Generation IVS Network".* Ed. by D. Behrend and K. D. Baver. NASA/CP-2012-217504, pp. 212–221.

Gipson, J. (2012b). *SKED: VLBI Scheduling Software.* NASA/Goddard Space Flight Center Space Geodesy Program.

Gipson, J. (2014). "IVS Working Group IV and the New Open Format Database". In: *IVS 2014 General Meeting Proceedings "VGOS: The New VLBI Network".* Ed. by K. D. Baver, D. Behrend, and K. L. Armstrong. Beijing: Science Press, pp. 248–252. ISBN: 978-7-03-042974-2.

Gipson, J. and Baver, K. D. (2016). "Improvement of the IVS-INT01 sessions by source selection: development and evaluation of the maximal source strategy". *Journal of Geodesy* 90(3), 287–303.

Gross, R. S. (2000). "The excitation of the Chandler wobble". *Geophysical Research Letters* 27(15), 2329–2332. DOI: 10.1029/2000GL011450.

Haas, R., Elgered, G., Löfgren, J., Ning, T., Scherneck, H.-G., and Hobiger, T. (2015). "Onsala Space Observatory - IVS Network Station Activities during 2014". In: *International VLBI Service for Geodesy and Astrometry 2014 Annual Report.* Ed. by K. D. Baver, D. Behrend, and K. L. Armstrong. NASA/TP-2015-217532, pp. 98–101.

Hartmann, D. L., Klein Tank, A. M. G., Rusticucci, M., Alexander, L. V., Bönnimann, S., Charabi, Y., Dentener, F. J., Dlugokencky, E. J., Easterling, D. R., Kaplan, A., Soden, B. J., Thorne, P. W., Wild, M., and Zhai, P. (2013). "Observations: Atmosphere and Surface". In: *Climate Change 2013: The Physical Science Basis. Contribution of Working Group I to the Fifth Assessment Report of the Intergovernmental Panel on Climate Change.* Ed. by T. F. Stocker, D. Qin, G.-K. Plattner, M. Tignor, S. K. Allen, J. Boschung, A. Nauels, Y. Xia, V. Bex, and P. M. Midgley. Cambridge University Press, Cambridge, United Kingdom and New York, NY, USA, pp. 159–254.

Hase, H. and Pedreros, F. (2014). "The most remote point method for the site selection of the future GGOS network". *Journal of Geodesy* 88(10), 989–1006. DOI: `10.1007/s00190-014-0731-y`.

Herring, T. (1992). "Modeling atmospheric delays in the analysis of space geodetic data". In: *Proceedings of Refraction of Transatmospheric signals in Geodesy*. Ed. by J. C. De Munck and T. A. Spoelstra. Vol. 36. Netherlands Geodetic Commission Publications on Geodesy, pp. 157–164.

Himwich, E., Vandenberg, N., Gonzalez, R., and Holmström, C. (2003). "New developments in the NASA Field System". In: *New technologies in VLBI, Proceedings of a symposium of the International VLBI Service for Geodesy and Astrometry, ASP Conference Series*. Ed. by Y. C. Minh. Vol. 306. Astronomical Society of the Pacific, pp. 193–198.

Hobiger, T. and Jakowski, N. (2017). "Atmospheric Signal Propagation". In: *Springer Handbook of Global Navigation Satellite Systems*. Ed. by P. J. Teunissen and O. Montenbruck. Springer International Publishing, pp. 165–193. ISBN: 978-3-319-42928-1. DOI: `10.1007/978-3-319-42928-1_6`.

Hobiger, T., Otsubo, T., Sekido, M., Gotoh, T., Kubooka, T., and Takiguchi, H. (2010). "Fully automated VLBI analysis with c5++ for ultra-rapid determination of UT1". *Earth, Planets and Space* 62(12), 933–937. DOI: `10.5047/eps.2010.11.008`.

IGG Vienna (2018). *Institute of Geodesy and Geophysics at the Vienna University of Technology, Archive of troposphere delay parameters.*
available from: `http://ggosatm.hg.tuwien.ac.at/DELAY/SITE/VLBI/`. Accessed: 2018-04-23.

Jacobs, C. S., Arias, F., Boboltz, D., Böhm, J., Bolotin, S., Bourda, G., Charlot, P., De Witt, A., Fey, A., Gaume, R., Gordon, D., Heinkelmann, R., Lamber, S., Ma, C., Malkin, Z., Nothnagel, A., Seitz, M., Skurikhina, E., Souchay, J., and Titov, O. (2013). "ICRF-3: Roadmap to the Next Generation ICRF". In: *Journées 2013 "Systemes de Référence Spatio-temporels"*. Ed. by N. Capitaine, pp. 51–56.

Kalman, R. E. (1960). "A New Approach to Linear Filtering and Prediction Problems". *Journal of Basic Engineering* 82(1), 35–45. DOI: `10.1115/1.3662552`.

Karbon, M., Soja, B., Nilsson, T., Deng, Z., Heinkelmann, R., and Schuh, H. (2017). "Earth orientation parameters from VLBI determined with a Kalman filter". *Geodesy and Geodynamics* 8(6), 396–407. DOI: `10.1016/j.geog.2017.05.006`.

Karttunen, H. (2007). *Fundamental astronomy.* 5th ed. Springer Science & Business Media.

Klopotek, G., Artz, T., Bellanger, A., Bourda, G., Gerstl, M., Gordon, D., Haas, R., Halsig, S., Hjelle, G. A., Hobiger, T., Hugentobler, U., Iddink, A., Kirkvik, A. S., Lambert, S., Plank, L., Schmid, R., Shu, F., Titov, O., Tong, F., Wang, G., Xu, M., and Zheng, W. (2016). "Results from the VLBI Analysis Software Comparison Campaign 2015". In: *IVS 2016 General Meeting Proceedings" New Horizons with VGOS"*. Ed. by D. Behrend, K. D. Baver, and K. L. Armstrong. NASA/CP-2016-219016, pp. 203–207.

Klopotek, G., Hobiger, T., and Haas, R. (2017). "Geodetic VLBI with an artificial radio source on the Moon: a simulation study". *Journal of Geodesy.* DOI: 10.1007/s00190-017-1072-4.

Krásná, H., Böhm, J., and Schuh, H. (2013). "Free core nutation observed by VLBI". *Astronomy & Astrophysics* 555, A29. DOI: 10.1051/0004-6361/201321585.

Lagler, K., Schindelegger, M., Böhm, J., Krásná, H., and Nilsson, T. (2013). "GPT2: Empirical slant delay model for radio space geodetic techniques". *Geophysical Research Letters* 40(6), 1069–1073. DOI: 10.1002/grl.50288.

Lambeck, K. (1988). *Geophysical geodesy: the slow deformations of the earth.* Clarendon Press, Oxford, United Kingdom and Oxford University Press, New York, USA.

Leek, J., Artz, T., and Nothnagel, A. (2015). "Optimized scheduling of VLBI UT1 intensive sessions for twin telescopes employing impact factor analysis". *Journal of Geodesy* 89(9), 911–924. DOI: 10.1007/s00190-015-0823-3.

Lovell, J. E. J., McCallum, J. N., Reid, P. B., McCulloch, P. M., Baynes, B. E., Dickey, J. M., Shabala, S. S., Watson, C. S., Titov, O., Ruddick, R., Twilley, R., Reynolds, C., Tingay, S. J., Shield, P., Adada, R., Ellingsen, S. P., Morgan, J. S., and Bignall, H. E. (2013). "The AuScope geodetic VLBI array". *Journal of Geodesy* 87(6), 527–538. DOI: 10.1007/s00190-013-0626-3.

Ma, C., Arias, E. F., Eubanks, T. M., Fey, A. L., Gontier, A.-M., Jacobs, C. S., Sovers, O. J., Archinal, B. A., and Charlot, P. (1998). "The international celestial reference frame as realized by very long baseline interferometry". *The Astronomical Journal* 116(1), 516–546. DOI: 10.1086/300408.

Ma, C., Sauber, J. M., Bell, L. J., Clark, T. A., Gordon, D., Himwich, W. E., and Ryan, J. W. (1990). "Measurement of horizontal motions in Alaska using very long baseline interferometry". *Journal of Geophysical Research: Solid Earth* 95(B13), 21991–22011. DOI: 10.1029/JB095iB13p21991.

Malkin, Z., Jacobs, C. S., Arias, F., Boboltz, D., Böhm, J., Bolotin, S., Bourda, G., Charlot, P., De Witt, A., Fey, A., Gaume, R., Heinkelmann, R., Lambert, C., Chopo, M., Nothnagel, A., Seitz, M., Gordon, D., Skurikhina, E., Souchay, J., and Titov, O. (2015). "The ICRF-3: Status, plans, and progress on the next generation International Celestial Reference Frame". In: *Journées 2014 "Systèmes de référence spatio-temporels".* Ed. by Z. Malkin and N. Capitaine, pp. 3–8.

Malkin, Z. (2007). "Empiric models of the Earth's free core nutation". *Solar System Research* 41(6), 492–497. DOI: 10.1134/S0038094607060044.

Matsuzaka, S., Shigematsu, H., Kurihara, S., Machida, M., Kokado, K., and Tanimoto, D. (2008). "Ultra-rapid UT1 Measurements with e-VLBI". In: *International VLBI Service for Geodesy and Astrometry 2008 General Meeting Proceedings.* Ed. by A. Finkelstein and D. Behrend, pp. 68–71.

McCallum, L., Mayer, D., Le Bail, K., Schartner, M., McCallum, J., Lovell, J., Titov, O., Shu, F., and Gulyaev, S. (2017). "Star Scheduling Mode–A New Observing Strategy for Monitoring Weak Southern Radio Sources with the AuScope VLBI Array". *Publications of the Astronomical Society of Australia* 34, e063. DOI: 10.1017/pasa.2017.58.

McCarthy, D. D. and Petit, G., eds. (2004). *IERS Conventions (2003)*. IERS Technical Note 32. Frankfurt am Main: Verlag des Bundesamts für Kartographie und Geodäsie.

Mignard, F., Klioner, S., Lindegren, L., Bastian, U., Bombrun, A., Hernández, J., Hobbs, D., Lammers, U., Michalik, D., Ramos-Lerate, M., Biermann, M., Butkevich, A., Comoretto, G., Joliet, E., Holl, B., Hutton, A., Parsons, P., Steidelmüller, H., Andrei, A., Bourda, G., and Charlot, P. (2016). "Gaia Data Release 1 - Reference frame and optical properties of ICRF sources". *Astronomy & Astrophysics* 595, A5. DOI: `10.1051/0004-6361/201629534`.

Mujunen, A. and Salminen, T. (2013). *Final report on Networked Storage on Demand*. Tech. rep. The Joint Institute for VLBI in Europe.

Munk, W. H. and MacDonald, G. J. (1960). *The Rotation of the Earth: A Geophysical Discussion*. Cambridge monographs on mechanics and applied mathematics. Cambridge University Press, New York, USA.

Niell, A. E. (1996). "Global mapping functions for the atmosphere delay at radio wavelengths". *Journal of Geophysical Research: Solid Earth* 101(B2), 3227–3246. DOI: `10.1029/95JB03048`.

Niell, A. E. (2000). "Improved atmospheric mapping functions for VLBI and GPS". *Earth, Planets and Space* 52(10), 699–702. DOI: `10.1186/BF03352267`.

Niell, A. E., Whitney, A., Petrachenko, B., Schlüter, W., Vandenberg, N., Hase, H., Koyama, Y., Ma, C., Schuh, H., and Tuccari, G. (2006). "VLBI2010: Current and Future Requirements for Geodetic VLBI Systems". In: *International VLBI Service for Geodesy and Astrometry 2005 Annual Report*. Ed. by D. Behrend and K. Baver. NASA/TP-2006-214136, pp. 13–40.

Nilsson, T. and Haas, R. (2010). "Impact of atmospheric turbulence on geodetic very long baseline interferometry". *Journal of Geophysical Research: Solid Earth* 115(B3), B03407. DOI: `10.1029/2009JB006579`.

Nilsson, T., Soja, B., Karbon, M., Heinkelmann, R., and Schuh, H. (2015). "Application of Kalman filtering in VLBI data analysis". *Earth, Planets and Space* 67(1), 136. DOI: `10.1186/s40623-015-0307-y`.

Nothnagel, A., Artz, T., Behrend, D., and Malkin, Z. (2017). "International VLBI Service for Geodesy and Astrometry". *Journal of Geodesy* 91(7), 711–721. DOI: `10.1007/s00190-016-0950-5`.

Nothnagel, A. (2009). "Conventions on thermal expansion modelling of radio telescopes for geodetic and astrometric VLBI". *Journal of Geodesy* 83(8), 787–792. DOI: `10.1007/s00190-008-0284-z`.

Nothnagel, A., Behrend, D., Bertarini, A., Charlot, P., Combrinck, L., Gipson, J., Himwich, E., Haas, R., Ipatov, A., Kawabata, R., Lovell, J., Chopo, M., Niell, A. E., Petrachenko, B., Schüler, T., and Wang, G. (2016). "Strategic Plan of the IVS for the Period 2016–2025". In: *IVS 2016 General Meeting Proceedins*. Ed. by D. Behrend, K. D. Baver, and K. Armstong. NASA/CP-2016-219016, pp. 3–11.

Nothnagel, A. and Schnell, D. (2008). "The impact of errors in polar motion and nutation on UT1 determinations from VLBI Intensive observations". *Journal of Geodesy* 82(12), 863–869. DOI: `10.1007/s00190-008-0212-2`.

Petit, G. and Luzum, B., eds. (2010). *IERS Conventions (2010)*. IERS Technical Note 36. Frankfurt am Main: Verlag des Bundesamts für Kartographie und Geodäsie.

Petrachenko, B., Behrend, D., Gipson, J., Hase, H., Ma, C., MacMillan, D., Niell, A. E., Nothnagel, A., and Zhang, X. (2014). "'VGOS Observing Plan'". In: *IVS 2014 General Meeting Proceedings "VGOS: The New VLBI Network"*. Ed. by K. D. Baver, D. Behrend, and K. L. Armstrong. Beijing: Science Press, pp. 16–19. ISBN: 978-7-03-042974-2.

Petrachenko, B., Niell, A. E., Behrend, D., Corey, B., Böhm, J., Charlot, P., Collioud, A., Gipson, J., Haas, R., Hobiger, T., Koyama, Y., MacMillan, D., Malkin, Z., Nilsson, T., Pany, A., Tuccari, G., Whitney, A., and Wresnik, J. (2009). *Design aspects of the VLBI2010 system - Progress report of the IVS VLBI2010 committee*. NASA/TM-2009-214180.

Petrov, L. and Boy, J.-P. (2004). "Study of the atmospheric pressure loading signal in very long baseline interferometry observations". *Journal of Geophysical Research: Solid Earth* 109, B03405. DOI: 10.1029/2003JB002500.

Plag, H.-P. and Pearlman, M., eds. (2009). *Global geodetic observing system: meeting the requirements of a global society on a changing planet in 2020*. Springer-Verlag Berlin Heidelberg. DOI: 10.1007/978-3-642-02687-4.

Rogers, A. E. E. (1970). "Very Long Baseline Interferometry with Large Effective Bandwidth for Phase-Delay Measurements". *Radio Science* 5(10), 1239–1247. DOI: 10.1029/RS005i010p01239.

Saastamoinen, J. (1972). "Atmospheric correction for the troposphere and stratosphere in radio ranging of satellites". In: *The use of artificial Satellites for geodesy, Geophysical Monograph Series*. Ed. by S. W. Hendrickson, A. Mancini, and B. H. Chovitz. Vol. 15. AGU, Washington, D.C., pp. 247–251.

Scherneck, H.-G. (1999). In: *Explanatory supplement to the section "Local site displacement due to ocean loading" of the IERS Conventions (1996) Chapters 6 and 7*. Ed. by H. Schuh. DGFI Report 71, pp. 19–23.

Schubert, S. D., Rood, R. B., and Pfaendtner, J. (1993). "An Assimilated Dataset for Earth Science Applications". *Bulletin of the American Meteorological Society* 74(12), 2331–2342. DOI: 10.1175/1520-0477(1993)074<2331:AADFES>2.0.CO;2.

Schuh, H. and Behrend, D. (2012). "VLBI: a fascinating technique for geodesy and astrometry". *Journal of Geodynamics* 61, 68–80. DOI: https://doi.org/10.1016/j.jog.2012.07.007.

Searle, A. and Petrachenko, B. (2016). "Operational VGOS scheduling". In: *IVS 2016 General Meeting Proceedins*. Ed. by D. Behrend, K. D. Baver, and K. L. Armstong. NASA/CP-2016-219016, pp. 78–81.

Shaffer, D. B. (2000). "RFI: Effects on Bandwidth Synthesis". In: *IVS 2000 General Meeting Proceedings*. Ed. by N. R. Vanderberg and K. D. Baver. NASA/CP-2000-209893, pp. 402–406.

Soja, B., Nilsson, T., Karbon, M., Zus, F., Dick, G., Deng, Z., Wickert, J., Heinkelmann, R., and Schuh, H. (2015). "Tropospheric delay determination by Kalman filtering VLBI data". *Earth, Planets and Space* 67(1), 144. DOI: 10.1186/s40623-015-0293-0.

Souchay, J. and Feissel-Vernier, M., eds. (2006). *The International Celestial Reference System and Frame - ICRS Center Report for 2001-2004*. IERS Technical Note 34. Frankfurt am Main: Verlag des Bundesamts für Kartographie und Geodäsie.

Sovers, O. J., Fanselow, J. L., and Jacobs, C. S. (1998). "Astrometry and geodesy with radio interferometry: experiments, models, results". *Reviews of Modern Physics* 70(4), 1393–1454. DOI: 10.1103/RevModPhys.70.1393.

Steffen, H. and Wu, P. (2011). "Glacial isostatic adjustment in Fennoscandia—A review of data and modeling". *Journal of Geodynamics* 52(3), 169–204. DOI: 10.1016/j.jog.2011.03.002.

Sun, J., Pany, A., Nilsson, T., Böhm, J., and Schuh, H. (2011). "Status and future plans for the VieVS scheduling package". In: *Proceedings of 20th European VLBI for Geodesy and Astrometry (EVGA) Working Meeting, Bonn, Germany*, pp. 44–48.

Takahashi, F., Kondo, T., Takahashi, Y., and Koyama, Y. (2000). *Wave Summit Course: Very Long Baseline Interferometer*. Ohmsha, Ltd., Tokyo, Japan. ISBN: 4-274-90378-8.

Thaller, D., Krüger, M., Angermann, D., Rothacher, M., Schmid, R., and Tesmer, V. (2005). "Combination Studies Using the CONT02". In: *International VLBI Service for Geodesy and Astrometry 2004 Annual Report*. Ed. by D. Behrend and K. D. Baver. NASA/TP-2005-212772, pp. 13–24.

Thompson, A. R., Moran, J. M., and Swenson Jr, G. W. (2017). *Interferometry and synthesis in radio astronomy*. 3rd ed. Springer International Publishing. ISBN: 978-3-319-44431-4. DOI: 10.1007/978-3-319-44431-4.

Titov, O., Lambert, S. B., and Gontier, A.-M. (2011). "VLBI measurement of the secular aberration drift". *Astronomy & Astrophysics* 529, A91. DOI: 10.1051/0004-6361/201015718.

Titov, O., Tesmer, V., and Böhm, J. (2004). "'OCCAM v. 6.0 software for VLBI data analysis'". In: *IVS 2004 General Meeting Proceedings*. Ed. by N. R. Vanderberg and K. D. Baver. NASA/CP-2004-212255, pp. 267–271.

Tuccari, G., Alef, W., Bertarini, A., Buttaccio, S., Comoretto, G., Graham, D., Neidhardt, A., Platania P.R., Russo, A., Roy, A., Wunderlich, M., Zeitlhöfler, R., and Xiang, Y. (2010). "DBBC2 backend: Status and development plan". In: *IVS 2010 General Meeting Proceedings "VLBI2010: From Vision to Reality"*. Ed. by D. Behrend and K. D. Baver. NASA/CP-2010-215864, pp. 392–395.

Tuccari, G. (2004). "DBBC - a Wide Band Digital Base Band Converter". In: *IVS 2004 General Meeting Proceedings*. Ed. by N. R. Vanderberg and K. D. Baver. NASA/CP-2004-212255, pp. 234–237.

Tuccari, G., Alef, W., Buttaccio, S., Casey, S., Felke, A., Lindqvist, M., and Wunderlich, M. (2014). "DBBC3: An EVN and VGOS All-inclusive VLBI System". In: *IVS 2014 General Meeting Proceedings "VGOS: The New VLBI Network"*. Ed. by K. D. Baver, D. Behrend, and K. L. Armstrong. Beijing: Science Press, pp. 86–90. ISBN: 978-7-03-042974-2.

Tuccari, G., Buttaccio, S., Nicotra, G., Xiang, Y., and Wunderlich, M. (2006). "DBBC - A Flexible Platform for VLBI Data Processing". In: *IVS 2006 General*

Meeting Proceedings. Ed. by D. Behrend and K. D. Baver. NASA/CP-2006-214140, pp. 185–189.

Uunila, M., Nothnagel, A., and Leek, J. (2012). "Influence of source constellations on UT1 derived from IVS INT1 sessions". In: *IVS 2012 General Meeting Proceedings "Launching the Next-Generation IVS Network".* Ed. by D. Behrend and K. D. Baver. NASA/CP-2012-217504, pp. 395–399.

Weston, S., Gulyaev, S., Kim, B., Litchfield, A., Hall, D., Curtis, J., Yun, T., Ruthven, A., Davies, G., Lagos, B., and Christie, D. (2017). "Towards Cloud Correlation of VLBI Data". In: *Proceedings of the 23rd European VLBI Group for Geodesy and Astrometry Working Meeting.* Ed. by R. Haas and G. Elgered, pp. 51–55.

Whitney, A. (1993). "The Mark IV VLBI Data-Acquisition and Correlation System". In: *Developments in Astrometry and their Impact on Astrophysics and Geodynamics.* Dordrecht: Springer Netherlands, pp. 151–157. ISBN: 978-94-011-1711-1.

Whitney, A. (2002). "Mark 5 Disc-Based Gbps VLBI Data System". In: *IVS 2002 General Meeting Proceedings.* Ed. by N. R. Vanderberg and K. D. Baver. NASA/CP-2002-210002, pp. 132–136.

Whitney, A. (2004). "The Mark 5B VLBI Data System". In: *IVS 2004 General Meeting Proceedings.* Ed. by N. R. Vanderberg and K. D. Baver. NASA/CP-2004-212255, pp. 177–181.

Whitney, A. and Lapsley, D. (2012). "Mark 6 Next-Generation VLBI Data System". In: *IVS 2012 General Meeting Proceedings "Launching the Next-Generation IVS Network".* Ed. by D. Behrend and K. D. Baver. NASA/CP-2012-217504, pp. 86–90.

Whitney, A., Ruszczyk, C., Romney, J., and Owens, K. (2010). "The Mark 5C VLBI Data System". In: *IVS 2010 General Meeting Proceedings "VLBI2010: From Vision to Reality".* Ed. by D. Behrend and K. D. Baver. NASA/CP-2010-215864, pp. 373–377.

Zhou, H., Li, H., and Dong, G. (2015). "Relative position determination between Chang'E-3 lander and rover using in-beam phase referencing". *Science China Information Sciences* 58(9), 1–10. DOI: 10.1007/s11432-015-5363-1.